Physics of very small bandgap carbon nanotube quantum dots

Master Thesis
Michiel Jol

July 2010

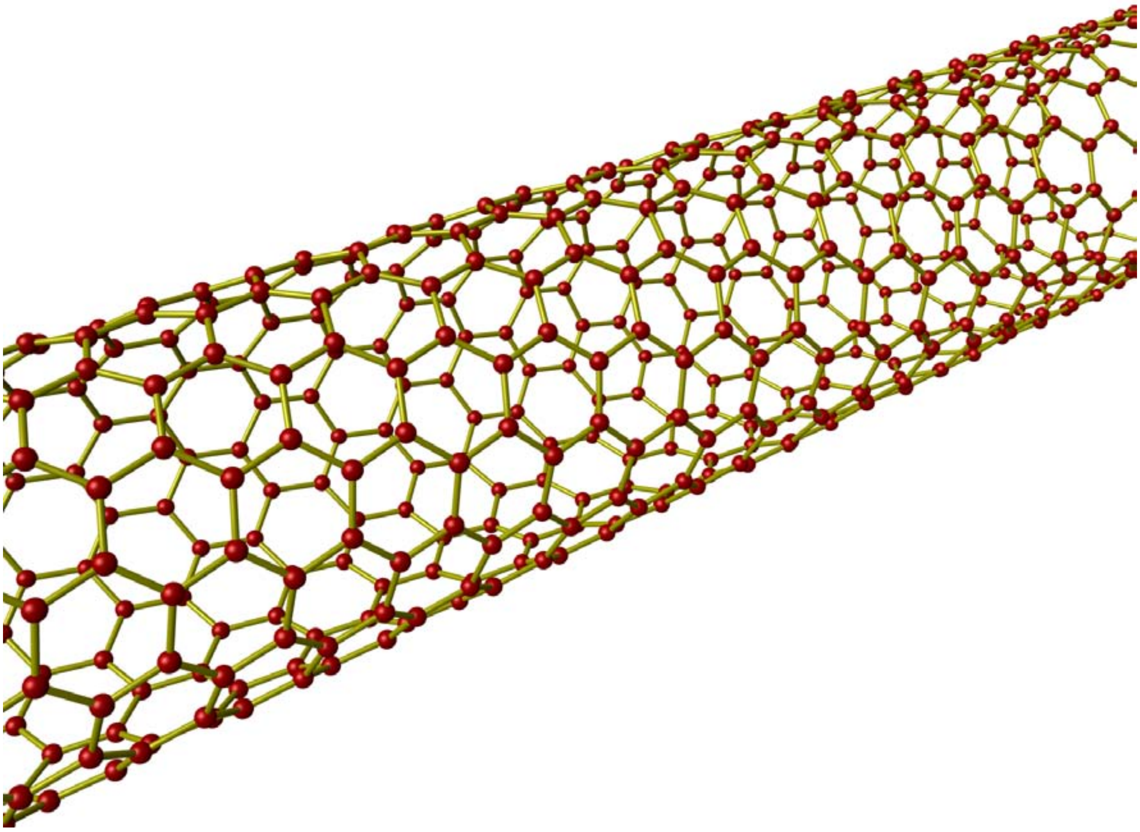

Delft University of Technology Faculty of Applied Sciences
Kavli Institute of NanoScience
Quantum Transport Group
Dr. Gary Steele
Prof.dr.ir. Leo Kouwenhoven

Abstract

In this thesis, measurements on small bandgap carbon nanotube quantum dots (CNT-QDs) are presented and discussed. Recent ‘ultra’ clean fabrication methods have enabled observations of a strong coupling between the spin and the orbital degree of freedom, arising from the curvature of the nanotube surface (Kuemmeth *et al.* (2008)).

In the work presented here a spin-orbit coupling is observed in several devices. In one such device, we find a spin-orbit coupling energy of 3.4 meV, which is an order of magnitude higher than observed before. We find that the sign of the spin-orbit coupling differs from device to device and suggest that it may be correlated with the nanotube chirality.

Devices are presented which have an ‘ultra’ small ‘intrinsic’ bandgap of a few milli electronvolts, which results in a Dirac crossing at observable fields of 2 T and less. Furthermore, we find a large suppression of the orbital magnetic moment from $\mu_{orb} = 0.8\ meV/T$ for the first electron in the dot, to $\mu_{orb} = 0.09\ meV/T$ for many electrons in the dot.

A model is introduced which includes spin-orbit interaction, very small values of $k_{\perp}$, and increasing $k_{\|}$ to calculate the electronic spectrum of a CNT-QD. This model qualitatively explains the suppression of the orbital magnetic moment and the shape of the Dirac crossing at measurable magnetic fields.

Measurements on one device in the many electron and hole regime show unexpectedly large magnetic field dependence and have a crossing of the second and third electron energies at high magnetic field that cannot be accounted for in the model presented here. As we believe our model includes all of the relevant single particle physics, we suggest that electron-electron interactions may be required to explain the many electron and many hole regime.

For the few electron regime the model provides a basis for understanding the spin physics of carbon nanotube devices experimentally, and can be applied to future work developing spin-qubits in CNT-QDs.

Acknowledgements

About a year ago I was searching for a master project and ended up in the group of Quantum Transport (QT). Almost all projects done in QT are very interesting, but only one is supervised by Gary. From the first moment I highly appreciated his very clear and enthusiastic explanations. Furthermore, he gave me the freedom to choose to do the parts of the project I liked and showed me what it means to be a good experimental physicist. Gary, I wish you the best in your new position as a staff member and as a father. Sorry that I only used ‘ultra’ in the abstract, but maybe you could use it in the title for the paper?

Besides Gary, I’d like to thank the rest of the nanotube team: Georg, Edward, Tang, Gilles, Vincent, Han and of course Leo. Furthermore, I appreciated the nice atmosphere in QT and the QT-activities. I’d like to thank all the master students in QT which I have had the privilege to share a room with. I especially enjoyed the discussions at the end of the day on very broad subjects to get my mind off the physics.

Many people have unwittingly contributed to my well-being during the long sessions of experiments. Without my friends I would have forgotten the world outside the lab, thanks for pulling me out once in a while.

Last but not least I would like to thank my parents and my girlfriend for their support in all things.

Michiel Jol - July 2010

Contents

Chapter 1

Introduction

1.1 (Non)sense fundamentals

In the last year I have been doing research in order to become a Master of Science, or 'Natuurkundig ingenieur'. I've been working on experimentally observing the fundamentals of quantum mechanics in a material and a logical question is: *why?* During this year, I've had several discussions with primarily non-physicists on the (non)sense of fundamental research without any foreseeable application in the near future, and want to briefly repeat my own personal arguments for this type of research. After this I will give a more scientific motivation for this research.

Why are we doing fundamental research, especially when no application is apparently involved? All people that I consider good physicists, will answer: *'because it is fun!'* (If you find them in an honest mood.) Being fun, unfortunately, does not justify large amounts of community and private money to be spend on research, so what is the use? The real (and honest) answer would be *'no idea'*, because that is the whole point of fundamental research: We *don't know* what will be discovered, since we have not discovered it *yet*. We do know that eventually *something very useful will be discovered that will have a very dramatic impact on global society.*

That fundamental research has impact on society is illustrated by the invention of the *LASER*. Albert Einstein himself did theoretically work in 1916 about a 'quantum theory for radiation' (Einstein (1916)), because he was interested in the *'elementary processes of emission and absorption'*. This paper was followed by theoretical and experimental work, that eventually led to the discovery of the laser. Applications of the laser can be found in construction, health, communication, and many other areas of society. Most of today's applications of the laser were not, and could not have been, imagined by Einstein.

A less direct way in which fundamental research can have impact is illustrated by the arrival of *the internet*. In the late 1980's, researchers at the European Organization for Nuclear Research, CERN, were investigating the fundamentals of particles, just like they are doing right now. Since the 1950's, a network of computers was linked together to communicate information over a distance between various facilities. To be able to improve their research infrastructure, they decided to design and implement a network-protocol that would be very userfriendly and bring various concepts of the existing network together.

In retrospect, this was the start of what we commonly describe as the internet, which impact on society is larger and more profound than anyone could have imagined. (What would be a more suitable reference for this story than Wikipedia (July 3rd)?)

These two examples illustrate how fundamental research has its impact on society and why it is very unlikely to know in advance what this impact exactly is. Unfortunately, there is a limit to the amount of money available for fundamental research, and this money usually goes to research that looks the most promising. This is why a scientist will argue about future use and potential when you ask for a scientific motivation. I do not want to argue that a scientist should not have such a motivation, but in the last year I have seen a gap between what scientist say about their motivation and their actual motivation. The ultimate goal of the research in this thesis can be argued (and will be argued) to be a quantum computer, but whether this will ever be achieved is generally not a concern of the people working on it, *as long as it is fun*.

1.2 Solid State Quantum Information Processing

in the remaining sections, the scientific motivation of this project will be given. The research in this master thesis was done in the Research Department Quantum Transport of the Kavli Institute of Nanoscience at Delft University of Technology. This group is part of an initiative called Solid State Quantum Information Processing (SSQIP), which describes the eventual goal of all the research done in this group: to *use solid state systems to process information using quantum mechanics*. The solid state system used in this research is a quantum dot (QD) in a carbon nanotube (CNT), and the research aims at understanding the behavior of a few electrons in such a carbon nanotube quantum dot (CNT-QD). Now, three questions will be answered in the next sections. First, why do we need quantum mechanics to process information? Second, why do we use carbon nanotubes? And third, why do we want to know about single electrons in these systems?

1.3 Breaking the computational barrier

"*Nature isn't classical, dammit, and if you want to make a simulation of Nature, you'd better make it quantum mechanical, and by golly it's a wonderful problem, because it doesn't look so easy.*" – Feynman (1982).

To simulate a physical system, very large amounts of data have to be processed. Examples of physical systems that physicists want to simulate are the folding of a protein or how the weather and climate will evolve. In order to do a simulation of these systems, a conventional computer uses bits which can be either a $|0\rangle$ or a $|1\rangle$ to store information. Very small and simple systems can be simulated with such a conventional computer. When bigger systems need to be simulated, the amounts of data that the computer needs to store increases exponentially. Furthermore, operations done on this data have to be done on each individual bit sequentially, making computing time also increase exponentially. Therefore, conventional computers are limited in the amounts of data they can store and the time they need to process these data.

The idea behind quantum information processing is to make use of the quantum-mechanical principles of superposition and entanglement to break this computational barrier. The basic tool of this so called quantum computing are quantum-bits (or qubits). A qubit is a quantum mechanical system with different states that can be labeled as $|0\rangle$ or $|1\rangle$, like a conventional bit. But now, because it is a quantum mechanical system, a superposition is possible where the qubit is in a state that is both an amount a_0 of $|0\rangle$ and an amount a_1 of $|1\rangle$ *at the same time*. Mathematically this means that a 2 dimensional vector can be represented by only one qubit. Calculations can be done on this qubit-state as a whole, automatically doing calculations on both the $|0\rangle$ and the $|1\rangle$ parts simultaneously. The real advantage of a qubit becomes apparent when multiple qubits are connected quantum-mechanically, by *entanglement*. Entangling multiple qubits makes them essentially act as one single system. This one system again can have superpositions, and can be represented by a 2^n-dimensional vector for only n-qubits. This enables extremely large amounts of data to be stored in only a few qubits. Still only one operation is needed to process the 2^n-dimensional vector, which enables very fast computation.

When a multiple-qubit system is realized and operations can be done on it, a quantum computer has been created which is fundamentally different from conventional computers, because it can contain enormous amounts of data and do calculations on this data all at once. Initially, Feynman thought of this computer to simulate physics, but once the potential of the quantum computer was realized, many more applications have been devised. Another possible application would be in breaking every possible conventional cryptography, but also making data encryption schemes which are physically not possible to hack. It is important to realize that "*a quantum computer will not be a faster, bigger or smaller version of an ordinary computer. Rather, it will be a different kind of computer, engineered to control coherent quantum mechanical waves for different applications.*" (from Ladd *et al.* (2010)). Unfortunately, no quantum computer has been build yet. Physics has succeeded in creating qubits in a variety of systems, for instance the polarization of a photon or the spin of an electron (Ladd *et al.* (2010)). But scaling up this process to include more than a few qubits, is proving very difficult. The search for the quantum computer continues, and is currently the holy grail of condensed matter physics.

In this thesis, the fundamentals of quantum dots in carbon nanotubes are investigated, which can eventually lead to realizing qubits in this system. I don't want to argue that this system is *the* system to realize a quantum computer. It is, however, a very good system to investigate fundamental quantum mechanics needed for qubits, and these fundamentals are very valuable on their own.

1.4 An ultimate nanomaterial

This section will discuss why we use Carbon nanotubes (CNT) to make a QD. Carbon nanotubes are hollow cylinders completely made of carbon with diameter in the nanometer range and lengths in the order of micrometers, which is thousands times larger than this diameter. Since their discovery in 1991 (multi wall Iijima (1991) and single wall Iijima & Ichihashi (1993)), there has been a boom in publication about their remarkable elasticity, strength and conductivity (Charlier *et al.* (2007)), as well as a broad range of applications. These applications range from tools in nano fabrication to macroscopic applications in tennis rackets. Because CNTs can be 'grown' in a near-perfect cylinder, the disorder in a CNT is very low and electrons can move ballistically through a nanotube. This makes the nanotubes a material with one of the highest electron mobilities known. Furthermore, the electronic structure of a nanotube is such that it is practically a 1-D material, making CNTs of fundamental importance for solid state physics.

In this research, QDs are created in CNTs with the goal of developing a spin-qubit (Hanson *et al.* (2007)). A quantum dot can be seen as a (very) little box that can trap one or more electrons. If this box is small enough (a few micrometers), quantum mechanics will play a significant role. If a repulsive electric field is applied to parts of a CNT, electrons are confined, making a quantum dot in a very simple and robust way. Another advantage of a CNT-QD is that the carbon atoms do not have a net nuclear spin. This means that no nuclear-spin can influence the electron in a QD in an uncontrolled way, as is the case for the conventional GaAs-QDs.

The wide range of applications of CNTs in both macro and nano scales and the ideal properties the tubes have to make a QD, make nanotubes an ultimate nanomaterial.

1.5 Unexpected behavior of trapped electrons

Doing quantum computations in CNT-qubits might be possible, but first the behavior of electrons in CNT-QDs must be investigated in order to be able to eventually controlling this behavior. This is the general goal of the work presented in this thesis. Meanwhile, this research has direct fundamental relevance, because the behavior of the electrons gives us insights in the principles of quantum mechanics. Furthermore, even if CNTs will never be used as qubits, its wide range of application already justifies investigating its electronic properties. In this thesis, CNT-QDs in the presence of magnetic field are investigated. Recently, a strong spin-orbit effect was discovered in cabon nanotubes and this is again observed in this experimental work. Furthermore, it is discovered that this spin-orbit effect is dependent on the specific type of nanotube. Also, nanotubes with a very small (intrinsic) bandgap are discovered to have fundamentally different properties in magnetic fields than assumed until now.

In short, we investigate a nice quantum-mechanical system and have some unexpected results. But, most importantly, it is *fun* because it is truly a *pleasure of finding things out* (Feynman (2008)).

Chapter 2

Theory

The aim of this thesis is to add to the understanding of electronic transport through carbon nanotube quantum dots (CNT-QDs) by explaining data from experiments. In order to understand the data, the basic theoretical concepts have to be introduced. This theory chapter will introduce the bandstructure of CNTs with help of the bandstructure of graphene. After that, the general concepts of physics of QDs will be explained. Then, the last section will elaborate on the specific mechanisms in a CNT-QD.

2.1 Bandstructure of carbon nanotubes

When doing any experiments involving electrons, the physical behavior of the electrons in the material at hand will determine the outcome. The field of solid state physics gives a set of tools to model this behavior (see, for instance, Ashcroft & Mermin (1976)). One of these tools is the construction of a bandstructure. This model combines the details of the chemical bonds that valence electrons form between individual atoms, with the overall structure (or lattice) in which the atoms are arranged. As a result, the electrons can have only limited ranges of possible energies, called bands. The structure of these bands determine the electronic properties of the material. The first part will explain the bandstructure of graphene, and this bandstructure will be used to show the bandstructure of CNTs in the second part.

2.1.1 Electronic structure of graphene

Graphene is a sheet of carbon-atoms in a honey-comb structure, as shown in figure 2.1(a). Multiple sheets of graphene are the basis of the well know graphite, found in pencils. As early as 1947 the first theoretical studies about graphene were published by Wallace (1947), followed by many more, because the calculations to obtain the bandstructure of graphene are relatively straightforward. On top of this, the bandstructure turns out to be of a special kind, as will be shown later. Graphene was believed to be too unstable to exist in real-life, until its discovery in 2004 by Novoselov *et al.* (2004). This resulted in a explosion of publications about the material. A good review about its electronic

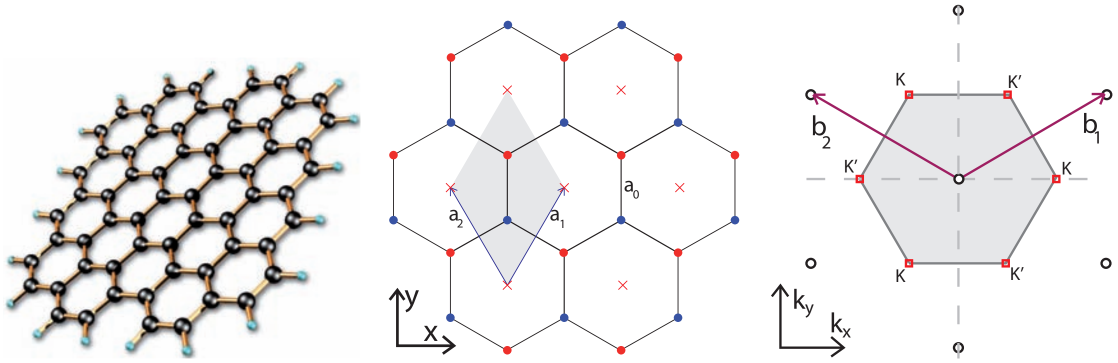

(a) (b) (c)

Figure 2.1: The structure of graphene and its reciprocal lattice. *(a) An artists impression of a graphene sheet taken from http://www.lbl.gov/Science-Articles/Archive/sabl/2007/Nov/gap.html on 28 May 2010. (b) The graphene lattice with it's primitive unit-cell indicated in gray. The nearest neighbor distance between atoms is shown as* a_0*. The lattice vectors are indicated by* a_1 *and* a_2*. (c) Brillouin zone of graphene with the reciprocal lattice vectors. The two inequivalent corners* K *and* K' *are indicated.*

properties can be found in Castro Neto *et al.* (2009). For this thesis only the bandstructure is important.

From figure 2.1(a) it is obvious that graphene has a very regular structure. The primitive unit-cell has two atoms, as shown in figure 2.1(b). The carbon-carbon distance is given as a_0 and has a documented value of 0.142 nm (Castro Neto *et al.* (2009)). The lattice-vectors for graphene are derived in appendix A as

$$\vec{a_1} = a \begin{bmatrix} 1/2 \\ \sqrt{3}/2 \end{bmatrix}, \quad \vec{a_2} = a \begin{bmatrix} -1/2 \\ \sqrt{3}/2 \end{bmatrix}, \tag{2.1}$$

with $a = \sqrt{3}a_0$. The reciprocal lattice vectors are

$$\vec{b_1} = \frac{2\pi}{a} \begin{bmatrix} 1 \\ \frac{1}{3}\sqrt{3} \end{bmatrix}, \quad \vec{b_2} = \frac{2\pi}{a} \begin{bmatrix} -1 \\ \frac{1}{3}\sqrt{3} \end{bmatrix}. \tag{2.2}$$

In figure 2.1(c) the Brillouin zone (BZ) is shown. The corners of the BZ are shared by three other zones, so a total of two inequivalent corners exist, called K and K'.

To be able to find the eigenstates of the Hamiltonian, the tight binding approximation is used. It is assumed that the electron-wavefunctions of the valence electron for each atom do not overlap much. The total wavefunction of the system is the summation over the wavefunctions for each individual atom with a small perturbation. Using only next neighbor interactions, an equation for the energy is found (see appendix A):

$$E(\vec{k}) = \pm\gamma_1 \left[3 + 2\cos(\vec{k}\cdot\vec{a_1}) + 2\cos(\vec{k}\cdot\vec{a_2})\right]^{\frac{1}{2}} \tag{2.3}$$

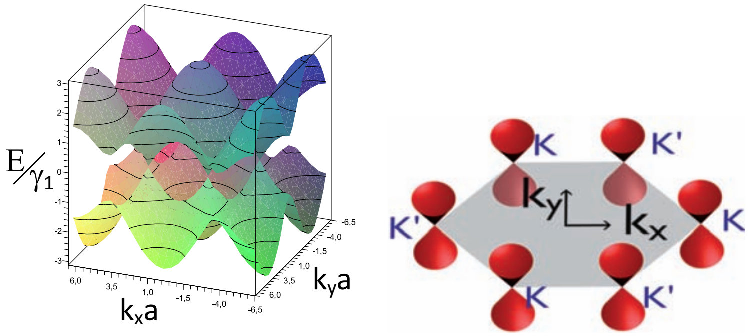

(a) (b)

Figure 2.2: The bandstructure of graphene and its Dirac points. *(a) Energy as a function of momentum (equation 2.3). The bottom band is called valence band or π-band and the top band is called the conduction-band or π^*-band. (b) Brillouin zone with Dirac cones at its K-points.*

In this equation, γ_1 is a measure for the overlap between atom wavefunctions and $\vec{k}$ is the wavevector, see figure 2.2(a). The above equation has a few points where it has zero energy and the bands touch each other, called Dirac points. These points turn out to be exactly the corners of the Brillouin zone, K and K'. The Fermi-level will be zero for undoped graphene. Therefore, the bandstructure around these K-points determines the behavior of electrons and the bandstructure can be expanded around these points. If κ is the distance in reciprocal space from a K-point, equation A.35 from appendix A gives

$$\begin{aligned} \epsilon(\vec{\kappa}) &= \pm\hbar v_f|\vec{\kappa}| = \pm\hbar v_f\sqrt{\kappa_x^2+\kappa_y^2}, \\ v_f &= \frac{\sqrt{3}\gamma_1 a}{2\hbar}, \end{aligned} \tag{2.4}$$

with a Fermi-velocity of $v_f \sim 10^6\ m/s$ and a nearest neighbor overlap energy γ_1 of $\sim 2.9eV$ (Castro Neto *et al.* (2009)). This is an equation of a cone with a slope of $\hbar v_f$, also called a Dirac cone. There is such a cone at each corner of the BZ, making a total of two inequivalent cones at K and K'. This is visualized in figure 2.2(b) and these cones will be used to derive the bandstructure of CNTs in the next section. As a final remark, the linear dispersion relation means that the velocity of an electron in graphene does not depend on the wave-vector, and the electrons behave as relativistic particles described by the Dirac equation. This feature is one of the main reasons for the interest in graphene.

2.1.2 Electronic Structure of Carbon Nanotubes

The previous section described the electronic structure of graphene. CNTs can be seen as tubes of rolled up graphene, having certain properties depending on how they are rolled up. Since the graphene lattice is rotational symmetric over 60° and posses inversion

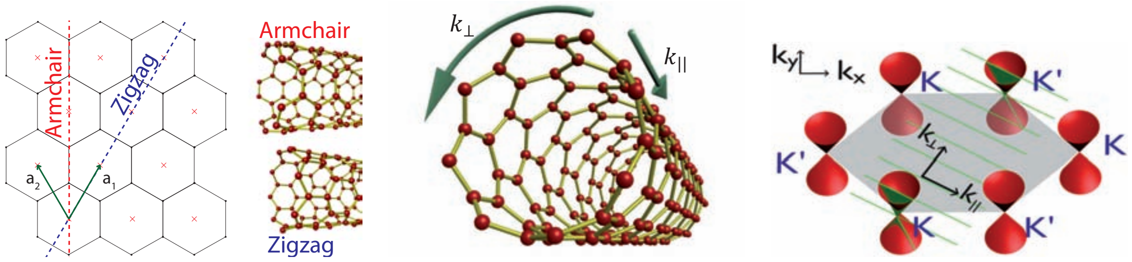

(a) (b) (c)

Figure 2.3: Carbon nanotube lattice and resulting quantization.*(a) The wrapping vectors to get the two extremes of nanotube chirality. To the right a (5,5) armchair and a (8,0) zigzag tube are shown. (b) The wavevector defined in the coordinates of the CNT.* $k_\perp$ *points around the circumference of the CNT and* $k_{||}$ *points along the axis of the tube. (c) The Brillouin zone of graphene with in green the possible values for* $k_\perp$ *of the CNT.*

symmetry, the CNT can effectively be rolled up over a wrapping vector $\vec{w}$ with an angle between 0° and 30°. This can be classified as in figure 2.3(a):

$$\text{Armchair} \quad : \quad \vec{w_a} = N(\vec{a_1} + \vec{a_2}), \tag{2.5}$$

$$\text{Zigzag} \quad : \quad \vec{w_z} = N\vec{a_1} \text{ (or } M\vec{a_2}), \tag{2.6}$$

where the names are derived from the shape of the end of the nanotube, as seen in figure 2.3(a). In between these two extremes the nanotubes are in general defined as chiral

$$\text{Chiral} \quad : \quad \vec{w_c} = N\vec{a_1} + M\vec{a_2}. \tag{2.7}$$

Usually, the chirality is indicated by a two integer vector (N,M).

The wavevector along the axis of the nanotube is defined as $k_{||}$ and the wavevector along the circumference of the tube as $k_\perp$, see figure 2.3(b). Now $k_\perp$ has periodic boundary conditions imposed on it, resulting in a quantization of

$$\vec{k_\perp} \cdot \vec{w} = \pi d k_\perp = 2\pi m \tag{2.8}$$

where d is the diameter of the tube and m is an integer. (See appendix B for a derivation of this for both armchair and zigzag tubes and Javey & Kong (2009) for above equation.) Figure 2.3(c) sketches what happens when these quantization lines are drawn in the graphene bandstructure. There are two lines close to a Dirac point, one for K and one for K' and these take a cut out of the cone. This cut is a distance $k_\perp^0$ from the Dirac Point (figure 2.4(a)), determined by the chirality of the tube through the quantization of equation 2.8. This approach is called zone-folding.

For all realistic single wall CNTs, the next quantization line already has an energy in the order of $\gamma_1 \sim 2.9\ eV \sim 10^4\ K$ and can be neglected (Appendix B and Charlier *et al.* (2007)). This means that only two values of $k_\perp$ are possible: one positive and one negative, and, as a result, the electrons travel the CNT counter-clockwise or clockwise, as

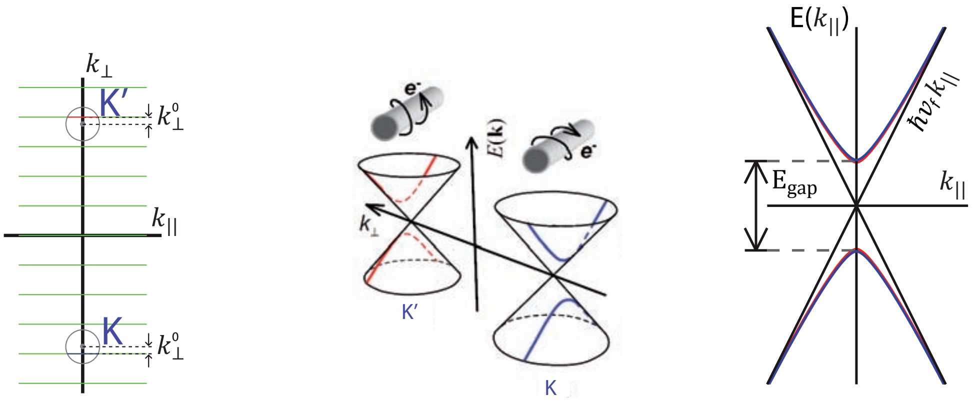

(a) (b) (c)

Figure 2.4: CNT quantization lines cut the two Dirac cones. *(a) A few of the quantization lines in the CNT coordinate system (see 2.3(c)). The lines cut the cones at a distance* $k_\perp^0$ *from the center. (b) The quantization line traces out a curve through the K and K′ Dirac cone. For one cone, the electrons travel clock-wise, for the other cone, they travel anti clock-wise. Figure adapted from Minot (2004). (c) The resulting CNT bandstructure given as a function of* $k_{||}$*. Both K and K′ contribute in same way to this bandstructure meaning a double degeneracy. The slope of the black graphene cone is* $\hbar v_f$*, making the bandgap* $E_{gap} = 2\hbar v_f k_\perp^0$*.*

shown in figure 2.4(b). For all practical purposes a CNT is a 1-D material device with two channels.

The final picture 2.4(c) of this section gives the bandstructure of a CNT for low energies (i.e. not reaching out of the cone). A more general bandstructure is given in appendix B, but this approximation will suffice for the purpose of this thesis. Note that both valleys K and K' have the same energy, meaning a double degenerate system. On top of this degeneracy, each valley can be occupied by an electron with spin up and one with spin down at the same time, making a total four-fold degeneracy. Nevertheless, it will be shown later that these valleys lift the degeneracy in the presence of a magnetic field. The bandgap is defined for a semiconductor as the distance between the valence and conduction band, and it follows that the bandgap is $E_{gap} = 2\hbar v_f k_\perp^0$. Tubes with a very small or zero $k_\perp^0$ have a very small or zero bandgap and are called *metallic* CNTs. On the other hand, CNTs with significant $k_\perp^0$ do have a bandgap and are therefore called *semi-conducting* CNTs. Note that the bandgap is linked to the diameter of the CNT by equation 2.8, and, on average (Javey & Kong (2009)),

$$E_{gap} \sim 0.7eV \text{ per nm diameter} \tag{2.9}$$

Several types of perturbations to this approach are possible. Axial strain, curvature and twists are a few examples of perturbations that shift the dispersion cones in a NT. As a result, the bandgap has a perturbative contribution that can dominate the total bandgap for otherwise metallic nanotubes. For more on bandgap perturbations, see Kane & Mele (1997) and Minot (2004).

2.2 Physics of quantum dots

This section will discuss the physics of a quantum dot (QD). In the first part the QD and its important features will be introduced. In the next part the constant interaction model will be presented together with a few basic concepts necessary for understanding experimental data from (transistor-type) QDs. After this, the final part will discuss the presence of features in QD transport that deviate from the constant interaction model.

2.2.1 Quantum dots

A QD is an artificial structure that is able to trap electrons in such a small area that the energies of the electrons become quantized. The trapping of electrons and the very small confinement area are the two main ingredients to make a QD.

The first ingredient of trapping electrons is a classical effect. If a piece of material is isolated from its surroundings, adding an extra electron to this material will cost electrostatic energy. The electrons on this ‘island’ create an electric field towards the surroundings of this island. The electric field results in a capacitance to the surroundings of the island and every time an electron is added, it will cost some energy to get to a new equilibrium. This energy is called charging energy and can be derived from elementary electrostatics as

$$E_C = \frac{e^2}{2C}, \tag{2.10}$$

where C is the capacitance of the island to its surroundings and e the electron charge. The capacitance scales with the size of the structure, and for a sphere of radius R this dependence is $C_{sphere} = 4\pi\epsilon_0 R$, with the electric constant ϵ_0. Note that only for very small structures this energy becomes significant. For a device of $\sim 10\ \mu m$ the charging energy $\sim 0.1\ eV$ is only bigger than the thermal energy for temperatures below $\sim 1\ K$. It is now possible, however, to fabricate very small structures of a few nanometers, resulting in very significant charging energies ($E_C \sim 100\ meV$ or $\sim 1000\ K$), see for instance Reimann & Manninen (2002). When this energy is not provided, no new electrons can tunnel on to the structure and this phenomena is called *Coulomb blockade*.

The second ingredient for the QD, the confinement, is strictly a quantum effect, resulting from the quantum mechanical wave nature of all particles. The wave function of the confined electrons will have to constructively interfere with itself, making only a few discrete wave vectors and corresponding energies possible. The energy difference between the discrete electron energies, called level spacing, depends strongly on the shape of the confinement. For a particle in a box the level spacing due to confinement of length L in one direction is (Thijssen & Van der Zant (2008))

$$\Delta E = \frac{h v_f}{2L}. \tag{2.11}$$

Using the Fermi velocity found for CNTs in the previous section, a confinement of a few hundreds of nanometer would yield $\Delta E \sim 10\ meV$. For a more introductory text on confinement see Griffiths (2005), and a more detailed discussion about quantum dots can be found in Kouwenhoven *et al.* (2001) and Hanson *et al.* (2007).

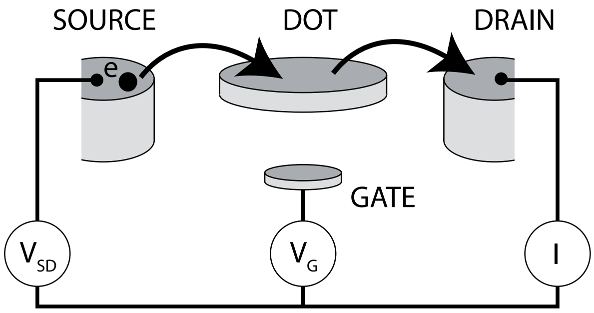

Figure 2.5: General structure of a transistor-type QD. *Electrons tunnel from source to the dot and from the dot to the drain. The gate is capacitively coupled to the dot. Figure adapted from* Hanson et al. (*2007*).

Quantum dots can be realized in a very large variety of materials and structures (see Gammon (2000) and Reimann & Manninen (2002)). This thesis will only discuss quantum dots of a transistor-type structure as shown in figure 2.5. In this configuration a large source of electrons is connected to the dot through a tunnel junction. Electrons cannot easily pass through a tunnel junction, since there is no classical connection between the two sides. They can, however, quantum mechanically tunnel through the junction with a probability that depends on the size of the barrier that creates the junction. On the other side of the dot another tunnel junction between the dot and a large drain is present. Electrons can hop on the dot and will remain there for a relatively long period of time if the tunnel probability is small enough (or the barrier big enough). The source and drain are also called the leads and have a capacitance C_S and C_D to the dot, respectively. To influence the energy states on the dot, a gate is placed in such a way that no tunneling is possible, but the dot is still capacitively coupled to the gate with a capacitance C_G. The measured current between source and drain, gives information about the processes on the dot and is a function of the difference between the source voltage V_S and drain voltage V_D, called the bias voltage V_{SD}, and gate voltage V_G.

2.2.2 Electronic transport in quantum dots

To describe the behavior of electrons passing through a QD as discussed above, the constant interaction model will be introduced. This model assumes that the charging energy E_C is always the same, irrespective of the number of electrons N on the dot. In other words: the capacitance of the dot does not change with electron number. Another assumption is that the level spacing is not influenced by the Coulomb interaction and can be viewed separately. This gives the following energy spectrum as a function of N (see Thijssen & Van der Zant (2008)):

$$\boxed{U(N) = \frac{(Ne)^2}{2C} - NeV_{ext} + \sum_{n=1}^{N} E_n}, \tag{2.12}$$

where C is the total capacitance of the system given by $C = C_S + C_D + C_G$, and E_n is the energy of quantum level n. The level spacing ΔE mentioned in the previous section determines the energy differences between the different n quantum levels E_n. V_{ext} is a net voltage due to the environment given by

$$V_{ext} = \frac{C_S V_S + C_D V_D + C_G V_G}{C}. \tag{2.13}$$

Usually, only the *difference* in energy is important and this can be visualized in a convenient way when the chemical potential $\mu(N)$ is used. The chemical potential $\mu(N)$ is the energy needed to add the Nth electron so

$$\mu(N) = U(N) - U(N-1) = \left(N - \frac{1}{2}\right)\frac{e^2}{C} - eV_{ext} + E_N. \tag{2.14}$$

Using this description the quantum dot is modeled as in figure 2.6. In general current flows in a system if there is a mismatch between chemical potentials in different areas: the source has particles with higher energy than the drain and current should flow. The difference between the chemical potentials of the leads, called bias window, is important and is caused by the voltage difference on the leads. Current cannot flow freely, however, because the dot must be able to carry electrons from source to drain. This means that states must be available in the bias window. Whether a state is available, depends on the chemical potential and that can be changed by the gate voltage V_G. If the bias window is small, the majority of gate voltages has no state available in the window and no current flows (Coulomb blockade). There are a few gate voltages that have a state available in the window and current flows for these gate voltages. Note that for a change in the gate voltage V_G, the chemical potential of the dot is changed by an effective voltage of αV_G where $\alpha = C_G/C$ and is called the α-factor.

An other important feature of the quantum dot is the energy difference between two consecutive states of the dot, called the addition energy E_{add}. The last section explained that both level spacing and charging energy contribute, resulting in

$$E_{add} = \mu(N+1) - \mu(N) = E_C + \Delta E(N), \tag{2.15}$$

where the level spacing ΔE depends on the specifics of the quantum mechanics involved, and could change for different electron numbers. Figure 2.6(c) gives the so called Coulomb peaks if the gate is swept at low bias. The distance between the peaks is the addition energy (which is α times the distance in voltage).

To get a better picture of transport through QDs, the strength of the barriers need to be taken into account as well. The rate of electrons passing through the barriers are Γ_S and Γ_D for the source and drain respectively (figure 2.6(b)). From the energy uncertainty principle it follows that $1/\Gamma \cdot \delta E \geq \hbar$, where δE is the the difference in energy between the level of the dot and the energy of the electron in the lead. This means that for a certain Γ, states that are a small energy δE (or less) outside the bias window, can already be used to carry current, effectively broadening the state. This broadening of the level and the corresponding Coulomb peak is called life-time broadening (or Γ-broadening) and has a Lorentzian shape (Datta (1997)). The temperature can also play a role through the leads.

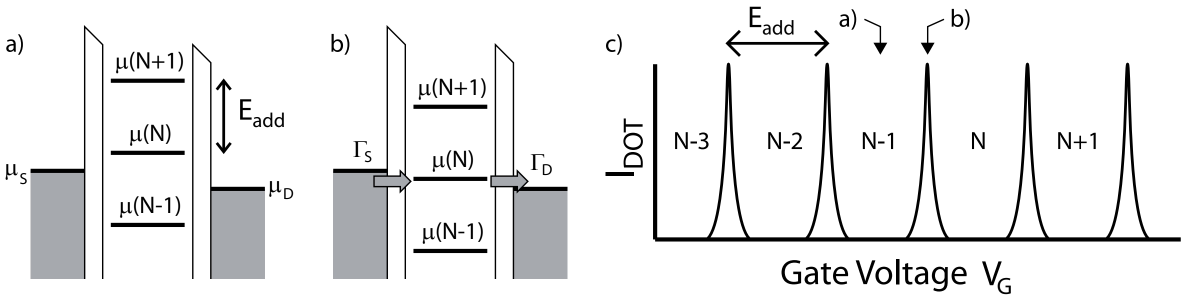

Figure 2.6: Schematic of transport through a quantum dot. *(a,b) Chemical potentials of a QD with fixed low bias* V_{SD} *and different* V_G*. The levels of the dot are quantized and the difference between them is the addition energy* E_{add}*. (a) The levels of the dot are outside the bias window and no current flows (Coulomb blockade). (b) The gate voltage has shifted the levels down, making a state is available in the bias window and current flows. The amount of current is determined by the barrier strengths* Γ_S *and* Γ_D*.(c) If the gate voltage is swept, peaks in the current are measured, called Coulomb peaks. The distance between the Coulomb peaks is the addition energy. Adapted from* Hanson et al. (*2007*).

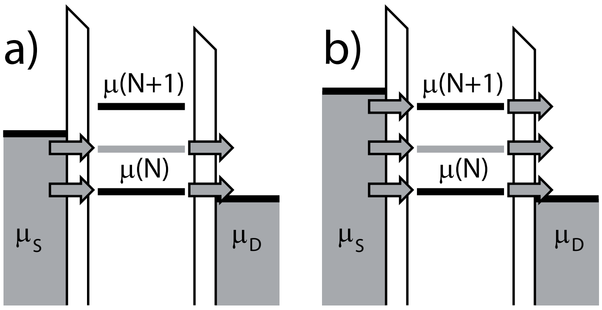

Figure 2.7: High bias measurements in QDs. *(a) The excited state of the* N^{th} *electron is shown in grey and gives a higher tunnel probability: only one electron at the same time can tunnel. (b) The bias is large enough to provide the charging energy and the ground state of N+1 becomes available:two electrons can tunnel at the same time. Adapted from* Hanson et al. (*2007*).

The continuous density of states of the leads are subject to the Fermi-Dirac distribution, meaning the Fermi-level of the leads is spread out over about $k_b T$. If $\hbar\Gamma > k_b T$, then the peaks are lifetime broadened, but if $\hbar\Gamma < k_b T$, then the peaks are temperature broadened and have a shape that is a derivative of the Fermi function which closely resembles a Gaussian. In experiments it is desirable to have as less broadening of the peaks as possible to be able to separately states with small energy differences. The minimum broadening in the type of devices used here is usually determined by lifetime, since it is experimentally difficult to reduce the barrier Γ towards the temperature limit of a dilution fridge.

Finally, not only the gate voltage is varied, but also the bias voltage. Until now, the bias was so small that only one state at the same time could fit in the window. By opening

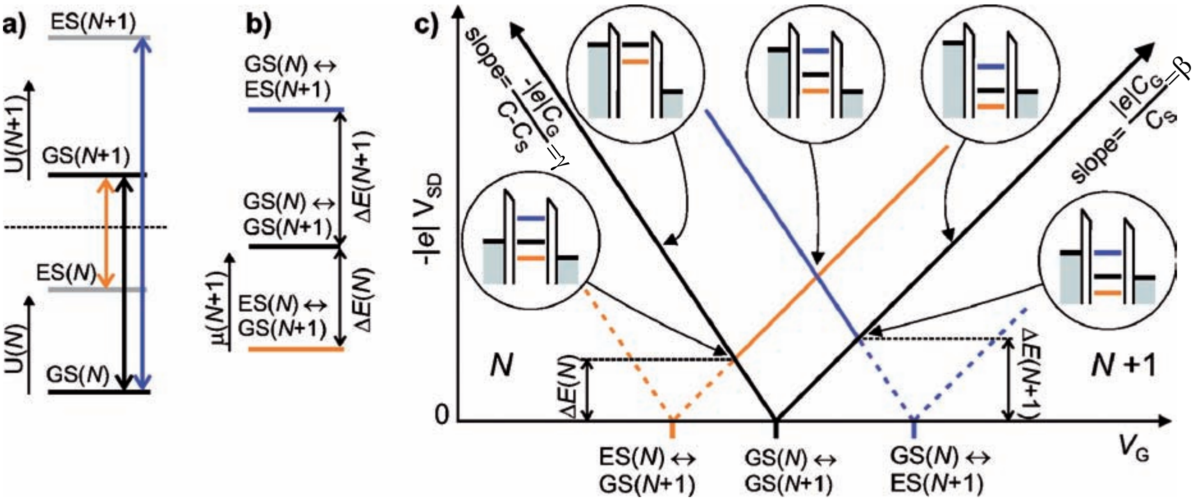

Figure 2.8: Schematic of high bias measurements. *(a) The energies of the different quantum states for the N^{th} electron and $(N+1)^{th}$ electron. The different transitions are indicated with arrows. Note that $ES(N) \longleftrightarrow ES(N+1)$ is omitted. (b) The chemical potential picture for the situation from (a). Plot of the differential conductance dI/dV_{SD} as a function of $-|e|V_{SD}$ and V_G. Several chemical potential diagrams are shown to illustrate the processes in the corresponding points. Adapted from Hanson et al. (2007).*

up the window, extra states become available at $\Delta E(N)$, which is the excited state (ES) of the initial ground state (GS) of this electron. Because the charging energy is not provided, only one electron at a given moment can tunnel, but the tunnel probability will increase since more states are available for tunneling, and the total current will increase (figure 2.7(a)). The next quantum level of the electron forms an excited state of the dot, but other effects like mechanical vibration can also form excited states and will be discussed in the last part of this section. If the bias is increased even more, the charging energy is also provided, creating the possibility of two electrons tunneling at the same time and increasing the current further (figure 2.7(b)).

Figure 2.8(a) gives the total energies of the different states and shows several possible transitions. Important, however, is the energy needed for these transitions, and a chemical potential scheme is shown in figure 2.8(b). The bias in combination with the gate voltage determines if a state is available and is visualized in 2.8(c). The black lines in this plot correspond to the transition GS(N)⟷GS(N+1). The slopes indicate the coupling factors between source and the dot (left line), and drain and the dot (right line), also called γ and β respectively. In this picture, the drain is taken to be grounded ($\mu_D = 0$), as is conventional in experiments. The coupling factor between the gate and the dot (α-factor) can now be calculated as $\frac{1}{\alpha} = \frac{1}{\beta} + \frac{1}{\gamma}$. The left line is drawn for the case where the transition is aligned with the source, and the right line is drawn for the case where this transition is aligned with the drain. Along these lines, the bias is increased and for the left line, the transition ES(N)⟷GS(N+1) becomes available (orange). Note that this line stops at the groundstate transition, since there can be no excited state if no ground state is available. To the right, the same happens for the transition GS(N)⟷ES(N+1) (blue). The energy

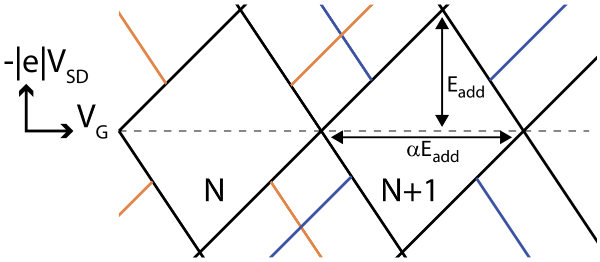

Figure 2.9: Schematic Coulomb diamonds. *The Coulomb diamonds are shown in the same configuration as 2.8. The addition energy can be determined by the height alone or by the α-factor and the width.*

difference belonging to a certain excited state transition is directly visible as $\Delta E(N)$ and $\Delta E(N+1)$, respectively. The use of the differential conductance against the two voltages is a very powerful and common tool and usually taken for both signs of V_{SD} and larger V_G, resulting in *Coulomb diamonds* (figure 2.9).

Sometimes, quantum levels are degenerate, and multiple electrons have the same (quantum-mechanical) energy. For many systems, electron spin causes such a degeneracy. For degenerate states, the gray excited lines in figure 2.7 coincide with the black ground state line and the current will be higher than for a single state. Looking at the Coulomb diamonds, this means that the addition energy E_{add} equals only the charging energy, since no energy is needed to get to a higher level. If only spin degeneracy is present, every odd N has an addition energy containing only the charging energy and the Coulomb diamond is smaller than those of even N (see, for instance, figure 2.11(b)).

2.2.3 Other features in quantum dot transport

In the previous part, the basic mechanisms for transport in QDs were explained. In the last part of this section, mechanical vibration, cotunneling, and the Kondo effect will be introduced briefly.

Vibrations

Quantum dots made in a structure that can vibrate can couple their electronic transport properties to vibrational modes. A relatively simple addition to the story so far occurs if an electron tunnels on the dot and the dot has certain vibrational modes. These modes can be viewed as extra exited states and will be visible as excitation lines in the Coulomb diamonds. This assumes both a very strong electron-phonon coupling and an energy of these phonon that is larger than that of the temperature ($\hbar\omega >> k_b T$). See Sapmaz *et al.* (2003), Sapmaz *et al.* (2006) and Leturcq *et al.* (2009).

In addition to these quantum effects, a classical effect occurs if the distance between the dot and its gates is changed due to the vibration of the structure. This change in distance results in a change in capacitance, which can modulate the current. In turn, the change in current can also change the mechanical motions. If this feedback is pos-

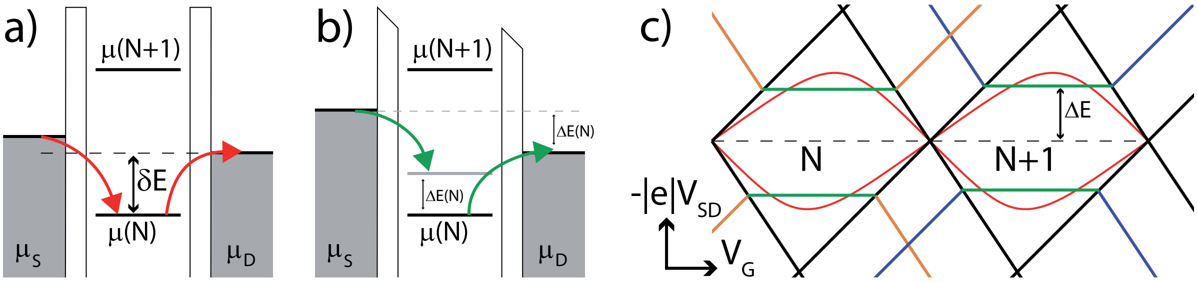

Figure 2.10: Cotunneling in a QD. *(a) Elastic Cotunneling: With no bias, one electron tunnels in at the same time as another tunnels out of the same level. This is called elastic cotunneling. (b) Inelastic Cotunneling: If the bias equals (or is larger than) the excitation energy, an electron tunnels to the excited state the same time as an electron tunnels out from the ground state. (c) Cotunneling in the Coulomb diamond of figure 2.9. Elastic cotunneling increases when approaching the Coulomb diamond edges and is shown in red. If the bias is equal to the excited state energy, inelastic cotunneling will increase the current, shown here as a green differential conductance line.*

itive, it will again lead to more current. The non-stable feedback will break down the regular Coulomb diamond structure, obscuring much of the underlying electrical properties. Whether this non-stable feedback occurs is dependent on the bias, the barrier transparency, and the Q-factor (a measure for the damping for mechanical motion), see Steele *et al.* (2009b). In the high Q-factor devices used in the experimental work for this thesis, we have tried to avoid mechanical feedback by sticking to mostly low bias experiments. Unfortunately, avoiding mechanical feedback was not always possible, resulting in measurements with limited visibility of the electronic states involved.

Cotunneling

In the last section, it was explained that no current will flow when there are no states available inside the bias window (Coulomb blockade). This is not strictly true, because current can flow in Coulomb blockade by means of so-called high order processes, like lifetime broadening already discussed above. These processes in general are called cotunneling events, because it involves the simultaneous tunneling of two or more electrons (De Franceschi *et al.* (2001)). In Coulomb blockade, if a state is an energy δE outside the bias window, the energy uncertainty principle states that during a time of about $\Delta t = \hbar/\delta E$, the addition energy does not have to be paid (see figure 2.10(a)). The tunnel barrier Γ determines this time, as explained above, so $\Delta t = 1/\Gamma$. Put differently, whenever $\delta E \leq \hbar\Gamma$ no addition energy is needed for an electron to tunnel in if within a corresponding time Δt an electron tunnels out, see figure 2.10. Elastic cotunneling occurs when the electrons tunnel in and out of the same (ground) state (figure 2.10(a)), and this causes current to flow close to the edges of the Coulomb diamond. This can also be explained as a life-time broadening of the edges of the Coulomb diamonds. When a bias is present that is at least equal to the excited state energy, an electron can also tunnel

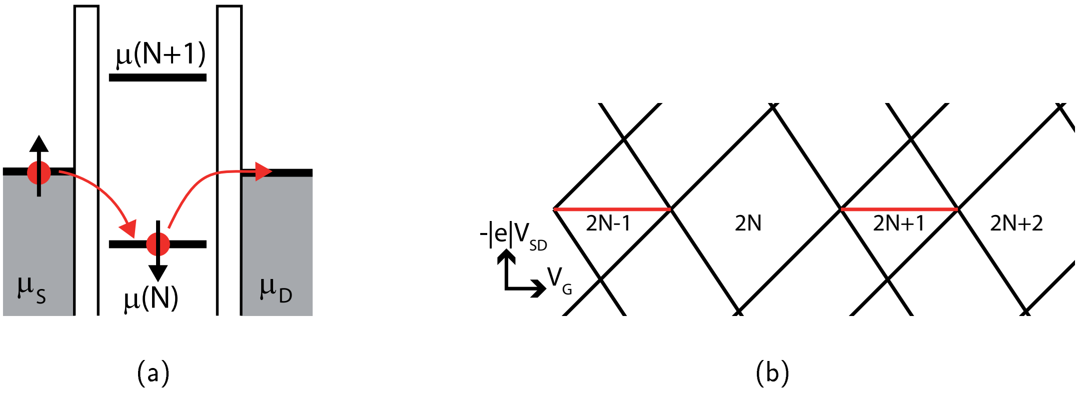

Figure 2.11: The Kondo effect in QDs. *(a) Interaction between spins causes one spin to tunnel out and a electron with opposite spin to tunnel in. (b) Kondo effect in a Coulomb diamond. Every odd diamond is smaller than the even diamonds because of the spin degeneracy. The odd diamonds have a differential conductance line at zero bias from the Kondo effect.*

in to the excited state at the same time as an other electron tunnels out of the ground state. This last process is called inelastic cotunneling although the total energy in this process is conserved. The result is shown in the Coulomb diamond of figure 2.10(c). More transparent barriers (higher Γ) will result in more cotunneling events and therefore more current. Inelastic cotunneling can sometimes be used as a tool to measure the excited state energies, since these lines have a better resolution in some situations than the first order excited state lines (De Franceschi *et al.* (2001)).

The Kondo effect

A special kind of elastic co-tunneling exists when a state is degenerate, called the Kondo effect. The Kondo effect is most commonly observed in spin-degenerate systems, but can also occur for other types of degeneracies (Jarillo-Herrero *et al.* (2005b)).

The Kondo effect is encountered only for a degenerate state, like odd spin, when the temperature is below the Kondo temperature T_K, and when the energy of the bias is below $k_b T_K$, see 2.11(b). Its origin lies in the fact that for an unpaired spin in the dot, a type of magnetic exchange interactions occurs with the electrons in the leads (Cronenwett *et al.* (1998)). As a result of this interaction, the electron in the dot is strongly coupled to the leads, allowing current to flow, even if the level is not aligned with the Fermi energy. In the experiments, this was encountered as current at zero bias in Coulomb blockade, see figure 2.11(a). The precise many body mechanisms behind the Kondo effect are beyond the scope of this thesis. For recent reviews on the Kondo effect in QDs, see Chang & Chen (2009) and Pustilnik & Glazman (2004).

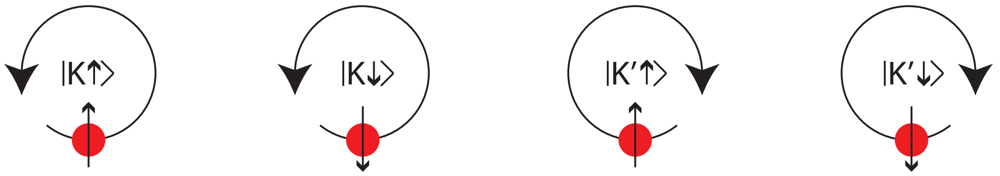

Figure 2.12: The states of one shell in a CNT-QD. *Both for spin (up or down) and valley (counterclockwise or clockwise) two different states with the same energy exist, creating a total of four states with the same energy.*

2.3 Electronic transport through CNT-QDs

This last section will discuss Quantum Dots in CNTs (CNT-QDs), combining the knowledge about the electronic structure of CNTs of the first section with the knowledge about QDs of the second section. Finite size will be introduced in the first part, followed by a part about the influence of magnetic field and orbital magnetic moment. The next part will introduce spin-orbit coupling, and the finishing part will deal with the disorder effects in CNTs.

2.3.1 Finite length CNTs

In the section about the bandstructure of CNTs it was assumed that the nanotube had an infinite length and was floating in free space. In real life, the CNT has a finite length L and has to make contact to its surroundings. The result of a finite length is a quantization of $k_{||}$. Remember that $k_{\perp}$ was already deduced to be in the K-valley or the K'-valley. The quantization is given by π/L and using equation 2.11, this is translated to energy:

$$\Delta E_{||} = \frac{h v_f}{2L}. \tag{2.16}$$

In the experiments in this thesis, a quantum dot is desired for which it is possible to distinguish between the different quantum states, so devices are actually designed to have a small L. Each value for $k_{||}$ has different possible values for the valley (K or K') and the spin (up or down), making a total of four states per $k_{||}$ value called a *shell*: $|K\uparrow\rangle$, $|K\downarrow\rangle$, $|K'\uparrow\rangle$, and $|K'\downarrow\rangle$, see figure 2.12. The initial assumption is that these states are degenerate, but a few mechanisms will be explained below that lift this degeneracy.

2.3.2 Contact effects in CNT-QDs

In electronic experiments, electric contact has to be made to the CNT. Usually the contact material is a metal, and if the CNT is metallic the contact is ohmic. If the CNT is semiconducting, a metal-semiconducting contact is formed. Each material has a workfunction $e\phi$, defined as the energy needed to take an electron from the Fermi energy to vacuum. The contact metals usually have a bigger workfunction than the nanotube, as will be explained in the next chapter when the device is introduced, see figure 2.13(a). In other words, the metal and semiconductor have a different Fermi energy and have to

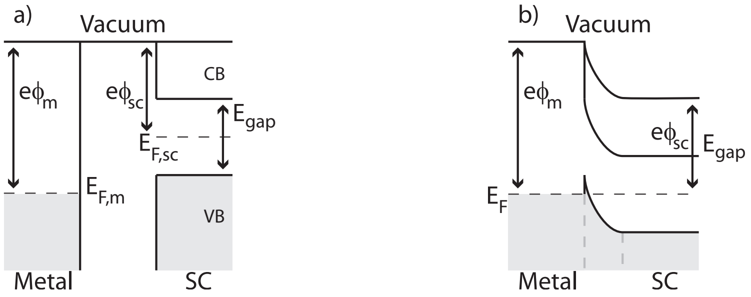

Figure 2.13: Metal-semiconductor contact. *(a) The metal and semiconductor (SC) are separated. in the metal, the states are filled up till the Fermi level $E_{F,m}$ and the semiconductor with a gap E_{gap} has a filled valence band (VB) and an empty conductance band (CB). The Fermi level of the (undoped) SC $E_{F,sc}$ lies in the middle of the gap. The workfunctions $e\phi_m$ and $e\phi_{sc}$ are indicated. (b) The metal and SC are in contact, a Schottky barrier is formed to align the Fermi levels to E_F.*

rectify this difference when brought in contact. If an undoped semiconductor is brought in contact with a metal with a bigger workfunction, the Fermi levels will align for the bulk of the materials. To accomplish this, the free charges in the metal and semiconductor will redistribute to shift the bandstructure. In the metal this will not have a significant effect because of the high charge carrier density, but in the (low charge density) semiconductor a significant region will be needed to shift the bands, thereby forming a barrier. This barrier is called the Schottky barrier and in the case of a bigger metal workfunction this barrier will be present for electrons. For holes, however, no contact barrier is present, see figure 2.13(b). Put differently: *the semiconductor becomes p-doped at the contact area*. For a more elaborate and general discussion about Schottky barriers see Sze (1981).

2.3.3 Magnetic field dependence

A magnetic field $B_{\|}$ can be applied to the CNT in the direction of the CNT-axis, see figure 2.14(c). The charges moves around the nanotube and the magnetic field couples to the phase via an Aharonov-Bohm term. Above, it was explained that the phase has to obey periodic boundary conditions and now equation 2.8 becomes dependent on $B_{\|}$. This means the quantization lines in the graphene bandstructure (figure 2.14(a)) get shifted in the $k_{\perp}$ direction with a change in field. For one valley, this results in a cut of the Dirac cone closer to the Dirac point and the other valley will be further away from its Dirac point, lifting the degeneracy of the two valleys (figure 2.14(c)).

The rate at which the energy changes with magnetic field can be calculated from the CNT bandstructure

$$E = \hbar v_f \sqrt{k_{\perp}^2 + k_{\|}^2}. \tag{2.17}$$

The bandgap gives a value for $k_{\perp}$ at zero field through $\hbar v_f k_{\perp}^0 = E_{gap}/2$, which is typically in the order of 100 meV. The energy-scale belonging to $k_{\|}$ is the level spacing $\hbar v_f \Delta E_{\|}$, which is typically in the order of a few meVs. It can therefore be assumed that $k_{\perp} >> k_{\|}$

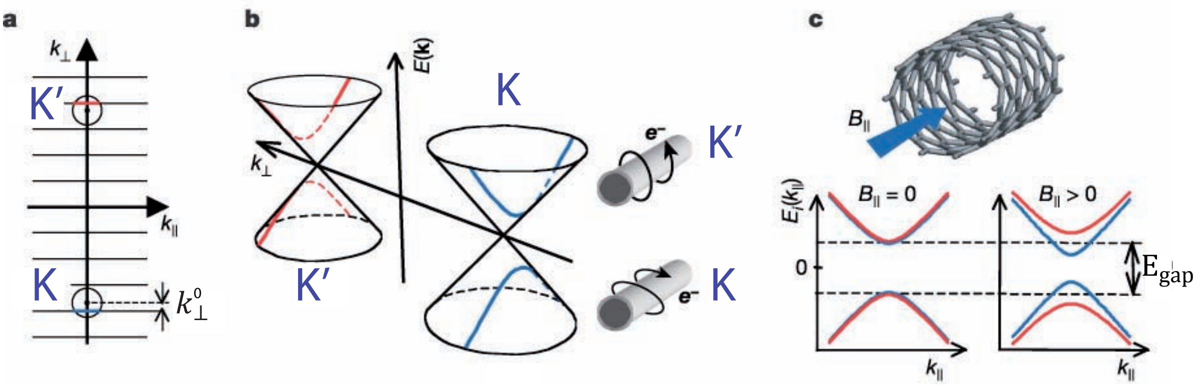

Figure 2.14: Magnetic field dependence of the bandstructure of CNTs. *Adapted from* Minot et al. *(2004). (a) The quantization lines in the graphene bandgap result in cross sections in the two cones in (b). (c) A parallel field will shift the quantization lines in (a) and move the cross section towards the Dirac point for K and away from the dirac point for K′, resulting in a splitting of the valleys.*

resulting in

$$\frac{\delta E}{\delta B} \approx \hbar v_f \frac{\delta k_\perp}{\delta B} = \mu_{orb}. \tag{2.18}$$

In this equation, the orbital magnetic moment μ_{orb} is defined as the rate of the change in energy with field and has a sign depending on the valley. This magnetic moment is called ‘orbital’ because the magnetic field couples to the valleys through their orbit around the CNT.

The orbital magnetic moment can also be derived in a more classical way when looking at the direction of the velocity around the tube obtained from the slope of the Dirac cone: $v_\perp = \hbar^{-1}\delta E/\delta k_\perp$. The valleys have the same speed but with opposite sign, resulting in a clockwise or anticlockwise motion (figure 2.14(b)). For a charge (like an electron) moving in a circle there is a magnetic moment, given by

$$\mu_{orb} = IA = \frac{ev}{2\pi R}\pi R^2 = \frac{Dev}{4}, \tag{2.19}$$

with current I and area A, speed v, radius R, and diameter D. Making the Hamiltonian

$$\boxed{H_{orb} = \pm\vec{\mu}_{orb}\cdot\vec{B} = \pm\frac{D\ e\ v_f}{4}B_\parallel}, \tag{2.20}$$

with a orbital magnetic moment μ_{orb} in the direction of the axis, and the sign depending on the valley (Minot *et al.* (2004)).

The electron spins are also influenced by the magnetic field by the usual Zeeman coupling term.

$$H_{spin} = \pm\frac{g\ \mu_B}{2}B \tag{2.21}$$

the sign depends on the direction of the spin. The g-factor in CNTs is found to be 2 (Charlier *et al.* (2007)) so the splitting of the levels becomes $g\mu_B = 0.116 meV/T$ and

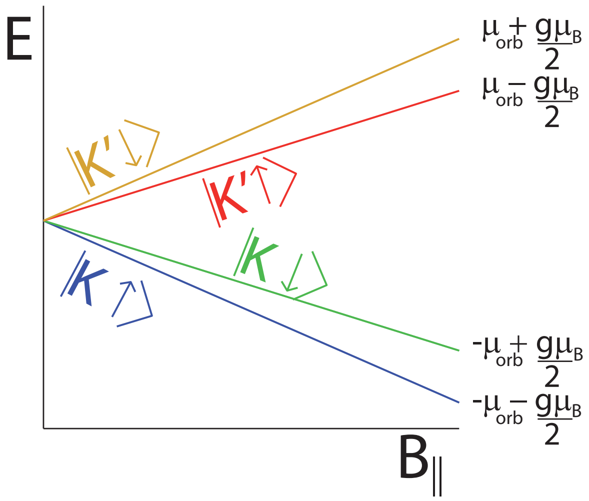

Figure 2.15: Simple picture of the magnetic field dependence of a shell. *Each state has a different slope, indicated to the right, which is a combination of the orbital and Zeeman slope.*

splitting due to the orbital magnetic moment has been measured in a range of $2\mu_{orb} \sim 0.7 - 3.0 meV/T$ (Jarillo-Herrero *et al.* (2005b), Minot *et al.* (2004), and Kuemmeth *et al.* (2008)). If both the spin and the valley contributions are taken into account, the four initially degenerate states for a given $k_{\|}$ have a different dependence on magnetic field as shown in figure 2.15. This assumes, however, that there is no coupling between spin and valley, an effect that will be discussed in the next section.

2.3.4 Spin-Orbit Coupling

Until recently, it was assumed that spin and orbit (valley) could be seen as independent in CNTs, but Kuemmeth *et al.* (2008) found that a strong spin-orbit coupling exists in nanotubes. This coupling is an effect that emerges because of the curvature of the CNT and was already theoretically predicted by Ando (2000) and further described by Huertas-Hernando *et al.* (2006) and Izumida *et al.* (2009). The derivation of the bandstructure assumes that the electrons use the free p_z-orbitals to move through the nanotube, exactly like they do for graphene (see first section of this chapter). In order to obtain a spin-valley coupling, the fact that these p_z orbitals are always perpendicular to the tube must be taken into account (figure 2.16(a)). In the previous section, it was discussed that the valleys K and K' move in opposite direction around the tube. In a reference frame that rotates around the tube with the electron, this motion is translated to a rotation of the lobes of the p_z orbital around the positive charge of the nucleus of the carbon atoms (figure 2.16(b)). These rotating lobes, combined with the radial electric field from the atomic core, lead to an effective local magnetic field along the axis of the tube:

$$\vec{B}_{SO} = \frac{\vec{v}}{c} \times \vec{E}. \tag{2.22}$$

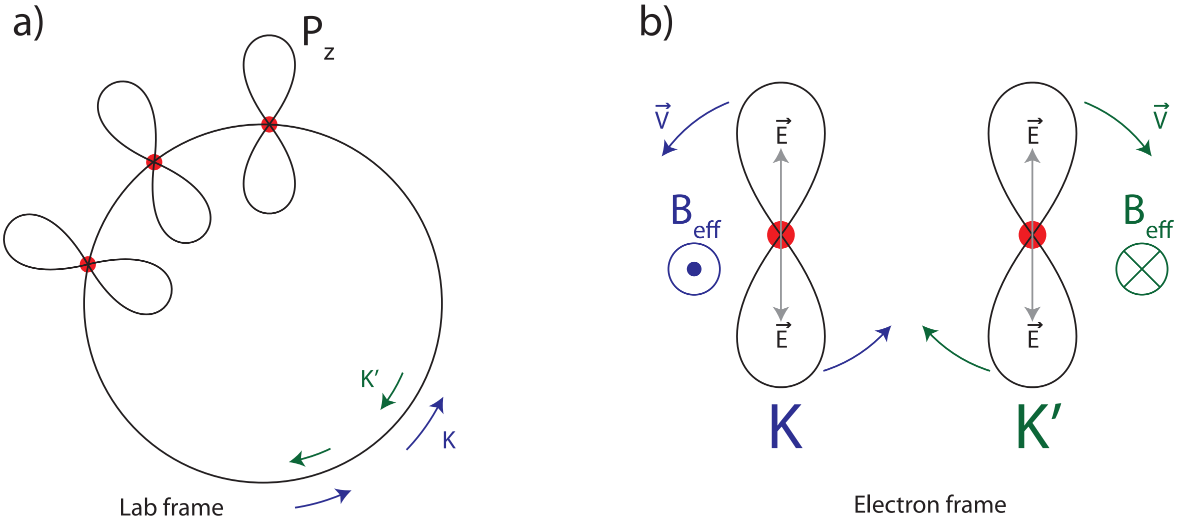

Figure 2.16: The curvature in CNTs causes an effective local magnetic field that has opposite direction for the two valleys. *(a) The p_z orbitals of the carbon atoms are always perpendicular to the plane of the nanotube and the electrons move around the nanotube with a direction depending on the valley. (b) In the rest frame of an electron the p_z orbital rotates around the electron. This causes an effective electric field which is opposite for both valleys.*

The speed v in this formula is determined by the distance l the orbital traces in one round and the time t it takes to do this. Now $l = 2\pi d_0$, where d_0 is the characteristic length scale for a lobe, and $t = \pi D/v_f$, where D is the diameter of the tube and v_f the fermi velocity as before. Making the speed $v = (d_0/D)v_f$ gives

$$B_{SO} = v_f \frac{d_0}{D} \frac{|\vec{E}|}{c}. \tag{2.23}$$

Both $|\vec{E}|$ and d_0 are properties intrinsic to the p_z orbital of carbon.

Because the effective local magnetic field is proportional to the local curvature, the electron will always acquire the same amount of phase for each rotation, even in the presence of local deformations of the nanotube. Such a phase that is independent of the trajectory was first discussed by Berry (1984) and is often referred to as a "topological" or "geometric" phase. Furthermore, since this spin-dependent phase is proportional to the angle the electron has traveled around the nanotube circumference, it will also shift the quantization lines an amount of k_{SO} in the graphene bandstructure (see figure 2.17(a) compared to figure 2.15). This is similar to the effect of an external magnetic field as explained in previous section, but now the magnetic field points in a direction that depends on the relative orientations of the valley and spin. The movement of an electron around the tube depends on the valley and the resulting change in phase due to the rotating p_z orbital couples to the spin, making a spin-valley (or spin-orbit) coupling. The effective magnetic field will split the spin-states within one valley, making the spin-state that is aligned with the effective magnetic field of the valley have a lower energy, and making the unaligned spin-state have a higher energy, see figure 2.17(a).

Experimentally, the spin-orbit effect manifest in a very clear way. If one electron is in a

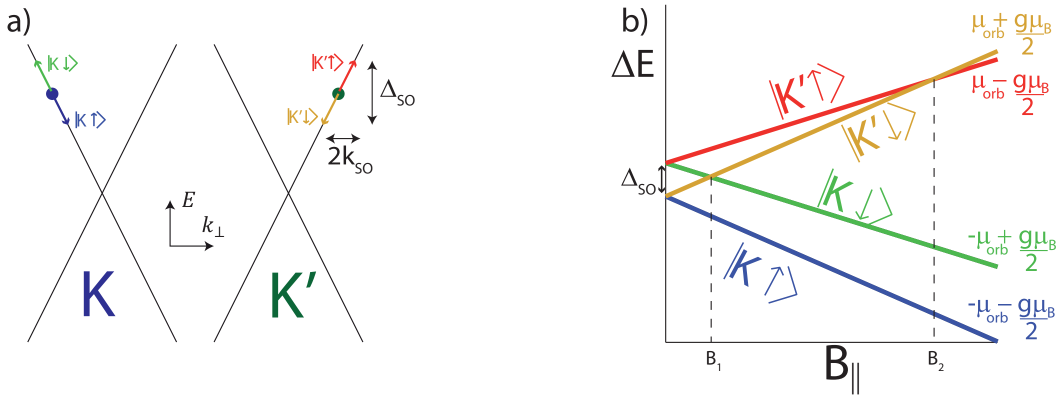

Figure 2.17: The effective magnetic field splits the valleys. *(a) The initial two-fold degenerate valley is split because the spin aligns or anti aligns with the effective magnetic field, moving the spin state a distance k_{SO} in the Dirac cone. (b) Magnetic field dependence of the four states of one shell. The spin-orbit coupling lifts the degeneracy at zero, but the two states of the K valley will move down and the two states K' will move up.*

shell, it occupies the K-valley and will move down in energy if an magnetic field is applied. The spin-orbit effect will make the other valley K' more energetically favourable for the second electron at low field, whereas it would also occupy the K valley without spin-orbit (figure 2.17(b)). At a certain field B_1 the second electron occupying the K'-valley (going up in energy with field) crosses with the K valley (going down with field). This crossing is determined by the orbital magnetic moment and the amplitude of the spin-orbit effect, and can be seen as the field where the orbital splitting overcomes the spin-orbit energy Δ_{SO}.

Other experimental evidence for spin-orbit is more subtle and happens when the Zeeman splitting overcomes the spin-orbit splitting. At a field B_2 one state crosses with a same valley state with opposite spin, and this is determined by the spin-orbit energy and the spin g-factor.

2.3.5 Disorder Effects

Several types of disorder in CNTs exist. Here, the two general types of longe range and short range disorder will be discussed, see figure 2.18.

First, long range disorder are defects that have a disorder potential that is slowly varying compared to the inter-atomic distance a_0. In the Fourier domain, this translates to wavevectors much smaller than the Brillouin zone. To scatter from one valley to the other (so scatter from clockwise motion to counterclockwise motion), a scattering vector of the order of the Brillouin zone is needed. This means that longe range disorder does not allow mixing between the two valleys. It can, however, divide the tube in two or more regions and create multiple quantum dots within the tube. This formation of dots in series can not be controlled and is unwanted in most cases. Localized charges in the vicinity of the tube (in the substrate), could cause long range disorder for example.

Second, short range disorder has a potential that varies on the scale of a_0 and this

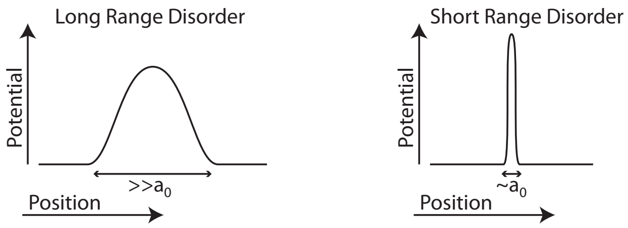

Figure 2.18: The type of disorder is determined by the characteristic length scale of the disorder potential. *Long range disorder (left) has a potential varying over a large range (compared to the interatomic distance a_0. Short range disorder (right) has a potential variying within the range of a_0.*

can mix the valleys, because the electrons can scatter from a clockwise to a counterclockwise motion and vise versa. This type disorder is also called KK'-mixing and causes the different valleys to lose their intrinsic properties, such as their orbital magnetic moments at low fields. KK'-mixing can be caused by deformations of the structure of the CNT, for example by putting the CNT on a rough substrate. It can also be caused by a vacancy in the CNT structure (missing carbon atom), substitution or addition of hydrogen atoms, or deformation of the lattice (local changes in inter atomic distance). The mixing states can be calculated by introducing mixing elements in the Hamiltonian for a given $k_{\|}$:

$$\mathbf{H}_{\mathbf{mixing}} = \begin{array}{c} \\ \langle K\uparrow| \\ \langle K\downarrow| \\ \langle K'\uparrow| \\ \langle K'\downarrow| \end{array} \begin{array}{cccc} |K\uparrow\rangle & |K\downarrow\rangle & |K'\uparrow\rangle & |K'\downarrow\rangle \end{array} \hspace{-17em} \begin{array}{c} \\ \left[\begin{array}{cccc} E_{|K\uparrow\rangle} & 0 & \frac{1}{2}\Delta_{KK'} & 0 \\ 0 & E_{|K\downarrow\rangle} & 0 & \frac{1}{2}\Delta_{KK'} \\ \frac{1}{2}\Delta_{KK'} & 0 & E_{|K'\uparrow\rangle} & 0 \\ 0 & \frac{1}{2}\Delta_{KK'} & 0 & E_{|K'\downarrow\rangle} \end{array}\right] \end{array}$$

The eigenvalues of this Hamiltonian are

$$\begin{aligned} \text{Mixed state 1} &= \frac{1}{2}\left[E_{|K\uparrow\rangle} + E_{|K'\uparrow\rangle} + \sqrt{(E_{|K\uparrow\rangle} - E_{|K'\uparrow\rangle})^2 - \Delta_{KK'}}\right] \\ \text{Mixed state 2} &= \frac{1}{2}\left[E_{|K\uparrow\rangle} + E_{|K'\uparrow\rangle} - \sqrt{(E_{|K\uparrow\rangle} - E_{|K'\uparrow\rangle})^2 - \Delta_{KK'}}\right] \\ \text{Mixed state 3} &= \frac{1}{2}\left[E_{|K\downarrow\rangle} + E_{|K'\downarrow\rangle} + \sqrt{(E_{|K\downarrow\rangle} - E_{|K'\downarrow\rangle})^2 - \Delta_{KK'}}\right] \\ \text{Mixed state 4} &= \frac{1}{2}\left[E_{|K\downarrow\rangle} + E_{|K'\downarrow\rangle} - \sqrt{(E_{|K\downarrow\rangle} - E_{|K'\downarrow\rangle})^2 - \Delta_{KK'}}\right] \end{aligned}$$

This means the states can be seen as decoupled when the energy difference between them is more than $\Delta_{KK'}$. For energy differences smaller than $\Delta_{KK'}$, mixing will occur and an avoided crossing will be the result. From this it can be seen that for a field smaller than $B_{KK'} = \Delta_{KK'}/\mu_{orb}$ the valleys are mixed and for fields bigger than $B_{KK'}$ the valleys are unmixed, as is shown in figure 2.19. Recently, innovations in fabrication have reduced disorder very significantly (Steele *et al.* (2009a)), and a very low $\Delta_{KK'}$ has been reported

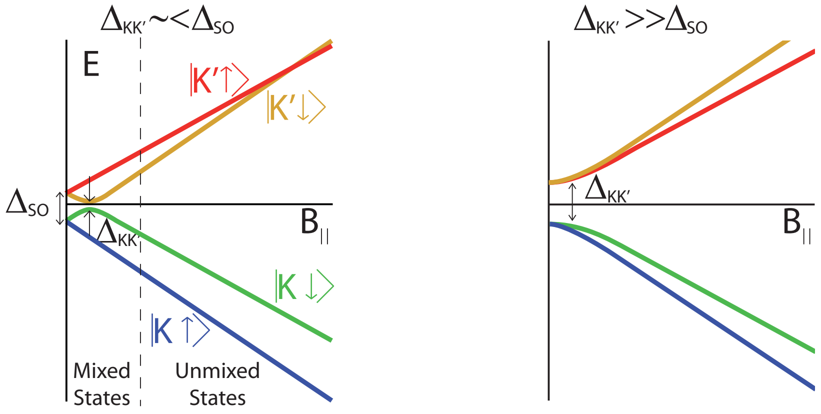

Figure 2.19: KK'-mixing causes the valleys to mix when close in energy. *The four states of a shell are shown, with the spin-orbit effect. When states in opposite valleys cross, an avoided crossing is observed with a characteristic scale of $\Delta_{KK'}$ for a small $\Delta_{KK'}$ (left), but for a big $\Delta_{KK'}$ (right) spin-orbit effects will no longer be visible. Furthermore, the orbital magnetic moment of the nanotube is suppressed for magnetic fields smaller than $B_{KK'} = \Delta_{KK'}/2\mu_{orb}$.*

(Kuemmeth *et al.* (2008)). This disorder reduction revealed low magnetic field and low energy features in electronic transport, such as the spin-orbit effect mentioned above.

Chapter 3

Experimental setup

This chapter will present the devices used in the experimental work. The measurement setup will be explained and the electronics involved will be discussed.

3.1 Device layout

During the experimental work, multiple devices were measured, made in one fabrication batch. All devices have the same design and differ only in some specific dimensions. Since the devices were made before the start of this project by G.A. Steele, the fabrication procedure will be discussed very briefly. A wafer with a silicon layer and a silicon oxide layer serves as an overall backgate and insulator. A silicon gate layer is deposited, followed by another silicon oxide layer, and electron-beam lithography and dry etching is used to create a trench as shown in figure 3.1. A 5/25 nm W/PT layer is deposited to serve as the

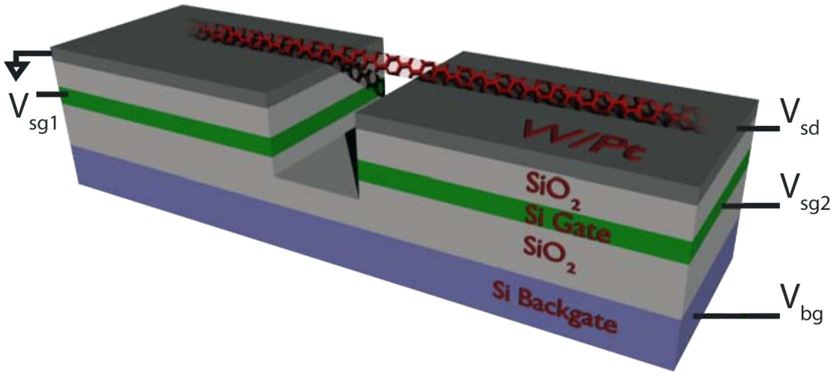

Figure 3.1: Schematic representation of the design of the used devices. *A Tungsten/Platinum (W/PT) metal contact is grounded on one side and biased on the other with* V_{SD}. *Beneath this metal a silicon oxide* (SiO_2) *insulator is placed, covering two silicon* (Si) *splitgates with a voltage offset* V_{SG1} *and* V_{SG2}. *Below the splitgate another oxide layer covers the* Si *backgate with voltage potential* V_{BG}.

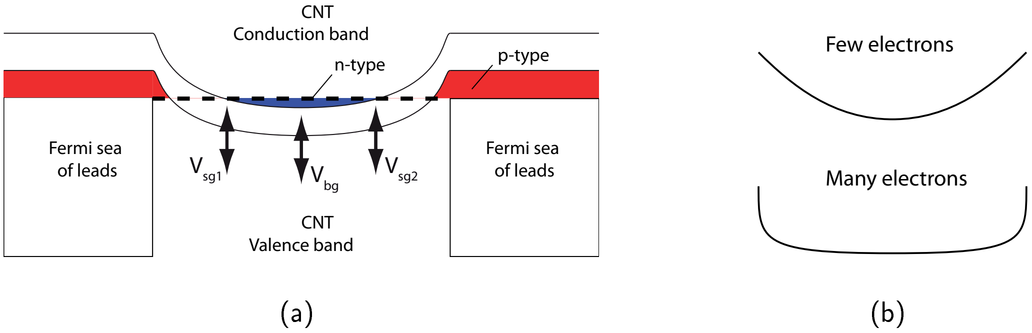

Figure 3.2: Electronic potential in the experimental device *(a) Scetch of the potential of the CNT for a specific configuration of gates. (b) Shape of the potential for a few and for many electrons.*

contacts. As a last step, a catalyst is used to grow the nanotubes, which fall over the trench in some devices. Because the nanotubes fall randomly, the exact position and orientation of the tubes is not known. The design is very similar to that used for Steele *et al.* (2009a), where the fabrication procedure is outlined in more detail. (Note that the only difference between the devices used in Steele *et al.* (2009a) and these devices, is that here the contact metal covers the whole silicon oxide layer.) Due to the workfunction difference between the contact metal $\phi_{Pt} = 5.6\ V$ (Lide (2008)) and the CNT $\phi_{CNT} \sim 4.7 - 4.9\ V$ (Liu *et al.* (2008)), the tube is doped with holes close to the contact by formation of a Schottky barrier, as explained in the theory chapter (section 2.3.2).

The key feature of the fabrication procedure is that the carbon nanotubes are ‘ultra clean’. In many fabrication procedures until recently, the nanotubes where grown first and the gates and contacts were deposited afterwards. As a result of these processes, significant short range and long range disorder was introduced (see section 2.3.5). With the fabrication method used here, the CNTs are measured *as-grown*, and disorder is significantly reduced (Cao *et al.* (2005)).

The splitgates are designed to change the potential of the CNT only locally, and in this way influence mainly the barriers. The backgate is an overall offset of the potential, and together these gates can be used to tune the nanotube to an ‘pnp’-doped device, and even switch between single dot and double quantum dot, as is done by Steele *et al.* (2009a). For a single dot, the splitgates determine where in the tube the dot is located. In the work presented here, the size of the trenches are of the same order as the distance from the tube to the splitgates, making the coupling of the splitgates to the CNT potential no longer ‘local’. This means that in this case, sweeping the splitgates together is enough to change the potential of the whole tube.

Figure 3.2(a) gives a scetch of the potential for a specific configuration of gates, and for this configuration, the tube is in ‘pnp’ mode. Note that this potential looks like a harmonic potential, and this could have consequences for the lateral quantization discussed in the theory, since there a hard-wall potential was assumed. The level spacing, for instance, is constant for a harmonic potential but depends on electron number for a hard-wall potential. If only a few electrons are in the dot, the size of the potential will not change much. The more electrons are added, however, the more the electrons will screen the gates, making the potential wider, and more towards a hard wall potential (figure 3.2(b)). As a consequence, the size of the dot changes with electron number, and this means that the coupling to the gates (α-factor) is also changed when an electron is added.

3.2 The dilution fridge

To be able to measure low energy features around 0.1 meV like spin-orbit coupling, the temperature has to be lower than 1 K. In the experimental work done here, a dilution fridge is used to reach a temperature of about 20 mK. First, helium can be liquefied, cooling it down to a temperatures of 4.2 K. About 60 liters of this liquid is transferred to a big vessel which is thermally isolated from room temperature by vacuum shields (cryostat), and an insert is submerged in the fluid, as is shown in figure 3.3(a). The insert consist of a sample holder, a 1K pot and a dilution unit, as shown in figure 3.3(b). Small amounts of 4.2 K helium are transferred to the 1K pot, and the gas is pumped out. Pumping all of the gas out of the 1K pot continuously means removing the high energy particles from the liquid, cooling it to 1.5 K. The 1K pot is thermally connected with a closed circuit containing a very special mixture of the very rare ^{3}He and conventional ^{4}He. If this mixture is cooled down below 1K by pumping on it, it will form two layers in the mixing chamber. On the bottom of the mixing chamber a dilute phase is presented, consisting of mostly ^{4}He. The concentrated phase, consisting mostly of ^{3}He, will normally not mix with the dilute phase because this is energetically unfavorable, but in this case it is forced through by pumping on the dilute phase in order to extract the ^{3}He from it, cooling the mixing chamber down to 20 mK, in our case. The extracted ^{3}He gas is recondensed, using the 1K pot, to complete the cycle. The sample is thermally anchored to the mixing chamber.

In the 4.2 K Helium, a super-conducting magnet (NbTi) is put to generate fields up to 9 T. The field is generated along the length of the insert.

3.3 Electronic Setup

The devices are fabricated on a chip, and can be connected by bonding wires to designed bond pads. These wires are also connected to a sample holder, which is placed inside the fridge, and go through some filters at cold temperatures and leave the fridge via the insert to the room temperature setup. Here, the different gates can be connected to an electronic setup as shown in figure 3.4.

To create computer-controlled, noise free voltage sources, a custom-made so-called IVVI rack is used. This rack has isolated voltage and current sources and measures current or voltage, and has its own battery power supply. The only incoming connection is an optical signal, so no interference can be picked up from the rest of the setup. Inside the rack, this optical signal is translated to voltages to send to the device. The resulting measured current is translated in a voltage, low-pass filtered and measured by a Keithley

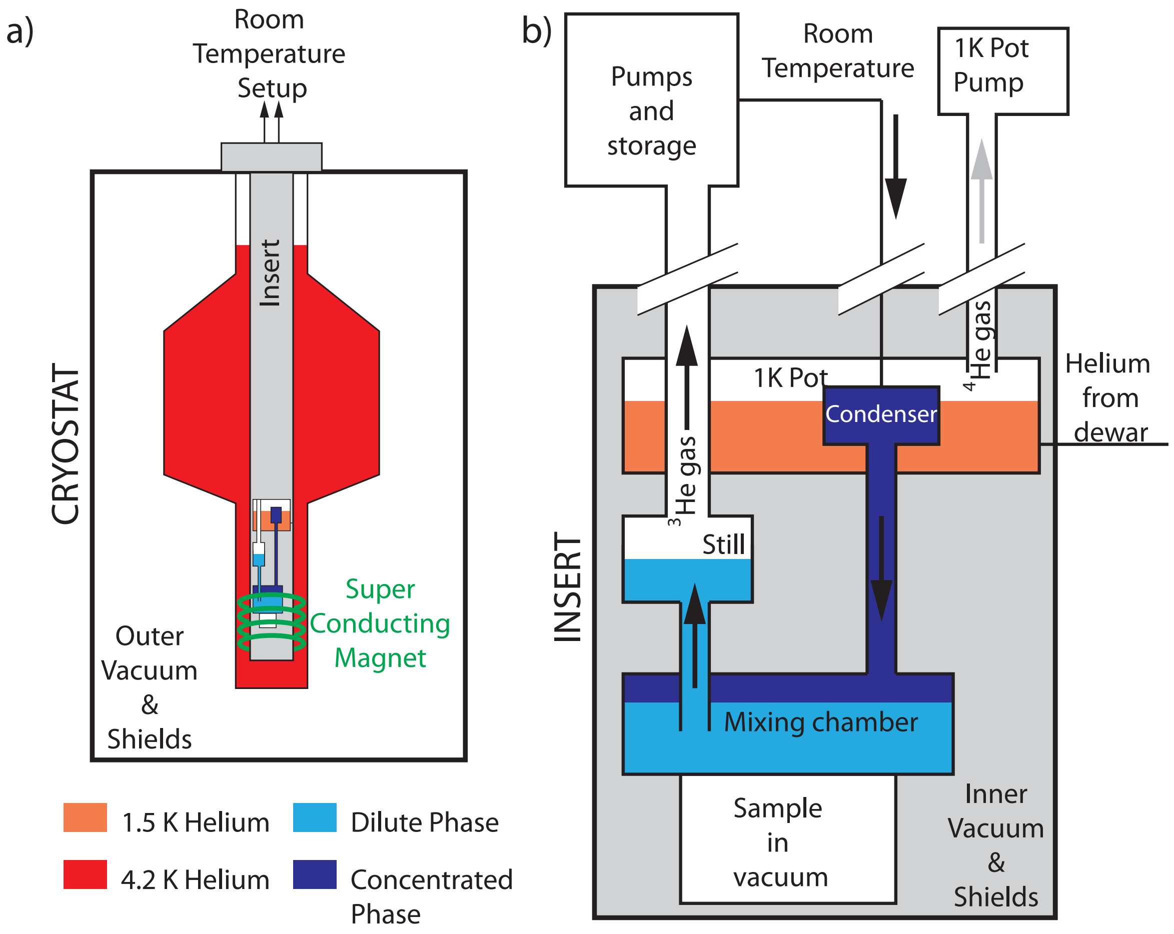

Figure 3.3: *Schematic of the dilution fridge.*

2700 voltage meter. Everything is controlled by a pc, which also sends signals to the magnet controller.

The device is vulnerable for fast changes in gate voltages. Charged defects in the oxide can be moved by a fast changes in the gates, resulting in switches in the measurement from the suddenly changed electrostatic environment. Furthermore, from previous experience with this type of devices, it was found that sweeping the gates too fast can result in breaking down the oxide, making the device useless for further measurements. Therefore, the software is programmed to sweep slowly and a resistance is put in series with the gate. The measured capacitance of the wires going to the sample is around a nano Farad, so putting a resistance of 1 $M\Omega$ in series will create a low-pass filter which makes the signal to the gate smooth on millisecond timescales.

Although only DC measurements are done, the timing is still critical due to capacitative coupling, and the time between each step has to be very constant to avoid significant noise. Thus, the software has to be optimized to make the timing as uniform as possible, as discussed in detail in appendix C.

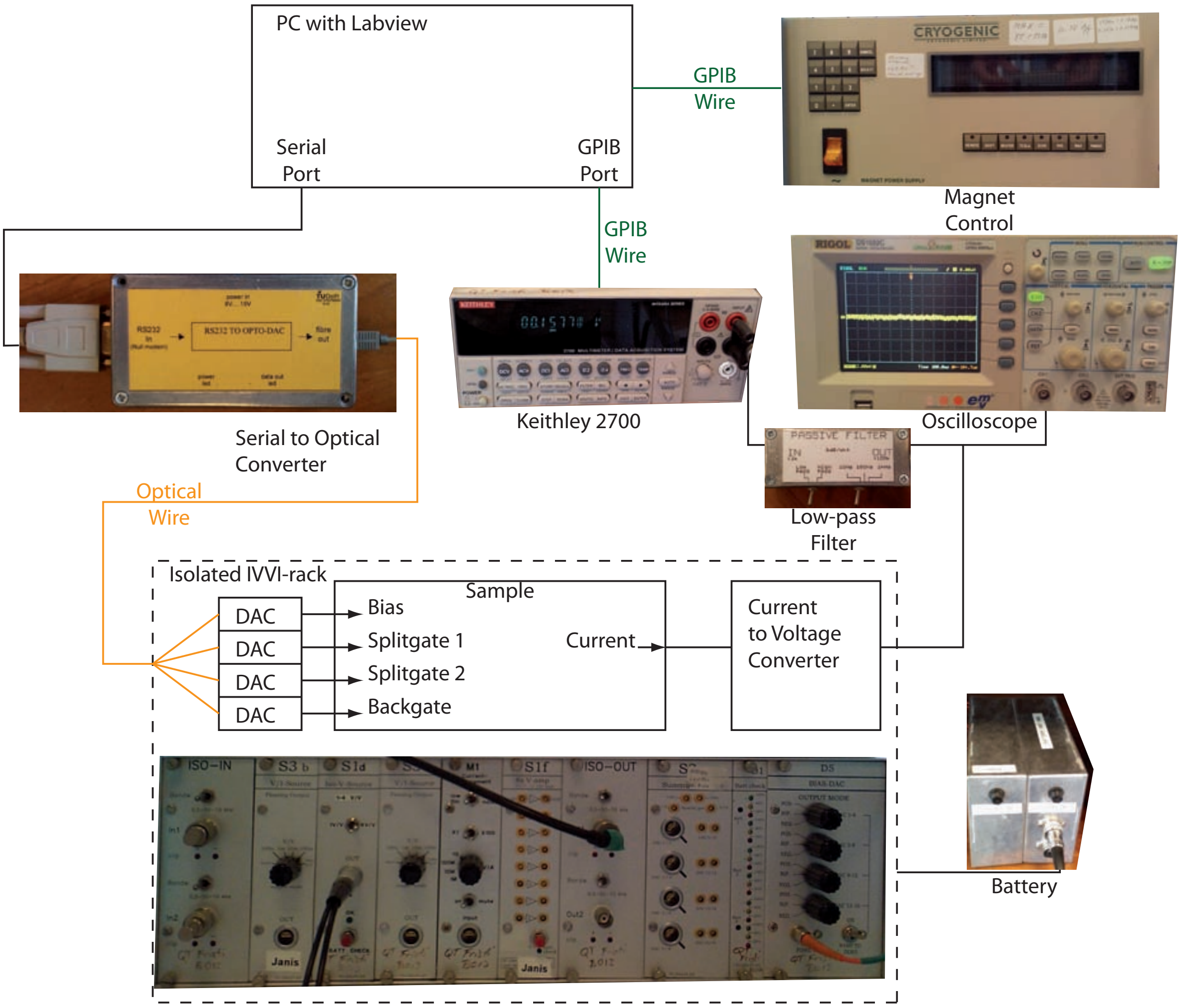

Figure 3.4: *Electronic Setup overview.*

Chapter 4

Results

During the experimental work of this thesis several devices were measured, and this chapter aims to summarize the most important findings. We set out to confirm the recent discovery of spin-orbit coupling in CNTs and look at this dependence for higher electron numbers than done before. It turned out that our devices not only have spin-orbit coupling, but also show some other unexpected behavior. These findings will be interpreted by looking again at the theory of the CNT bandstucture. Also, data is shown which we cannot explain with this theory.

4.1 Device Introduction

The devices can be best characterized by a few parameters. The first is the length of the trench of the device (see figure 3.1). Secondly, the bandgap can be determined from taking Coulomb diamonds of the device (see Appendix D). Third and last, a measurement of current as a function of the two splitgates shows the structure of the device. The splitgates are important because all devices used here have a small trench, and mainly the splitgates determine the shape of the potential in the tube. If both these splitgates have the same voltage, the QD sits in the middle and has a symmetric potential, but if one splitgate has a different voltage than the other, the electrons are attracted to the gate with the more positive voltage. The QD defined by the potential will move towards this gate, and will depend mostly on this gate (see figure 4.1). From the splitgate against splitgate plot (SGSG-plot) at low bias, places in 'gatespace' can be found where the dot has nice Coulomb peaks. This means that for that particular combination of gate voltages, a state is in the bias window and current can flow. The top left of a SGSG-plot usually shows a region with significant current occurring when the QD is hole doped (see appendix D.3).

Figure 4.1: The dot moves as a function of the splitgates (SGs)

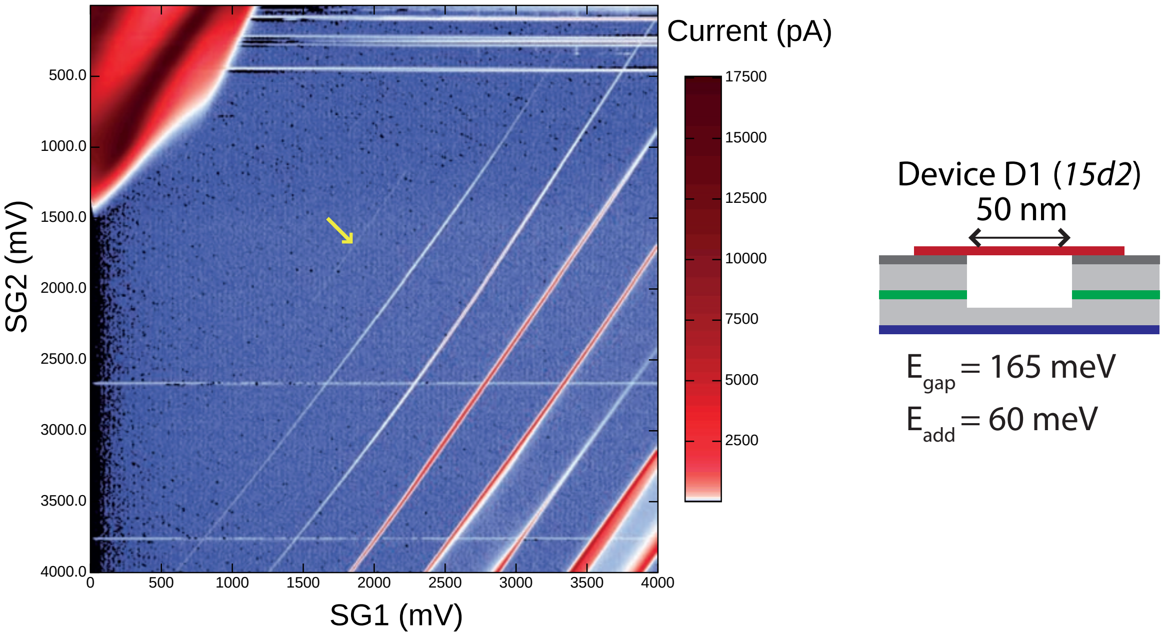

Figure 4.2: Device D1 Characteristics. *To the left a SGSG-plot of D1 at 1 mV bias is shown. The arrow indicates the very faint Coulomb peak of the first electron. To the right a schematic of device D1 (fabrication name 15d2) is drawn.*

If moving towards the center, a region without any current is visible, because the QD is tuned to be in the bandgap. Continuing towards the bottom right, lines become visible where the first line is the first electron entering the dot and the second line indicates the second electron, and so on. The direction of these lines gives information about the influence on the potential coming from each gate. For the extreme case that only one gate influences the potential, the lines would become either horizontal or vertical.

The first device D1 is shown in figure 4.2, and has a very small trench of 50 nm and a gap of 165 meV. The SGSG-plot shows that the dot does not move significantly towards one gate (straight lines) and some unidentified horizontal lines are visible for some values of SG2. A very faint line around (2000 mV, 2000 mV) shows the Coulomb peak of the first electron.

The second device D2 is shown in figure 4.3. It is has a trench of 100 nm and a gap of 80 meV (appendix D). The SGSG-plot shows a very clean and regular pattern of Coulomb peaks and nice single dot behavior, that can be tuned to the first electron.

The third device D3 is shown in figure 4.4, has a trench of 300 nm and a bandgap of 57 meV. The first two electrons are narrow Coulomb peaks, but higher electron numbers show broader lines and features in Coulomb blockade.

Note that for all devices the holes in the top left have a much higher current than the electrons in the bottom right, because the barriers for the holes are much lower than those for the electrons. This change in barrier has to do with the Schottky barrier (2.3.2) and is explained in appendix D.3.

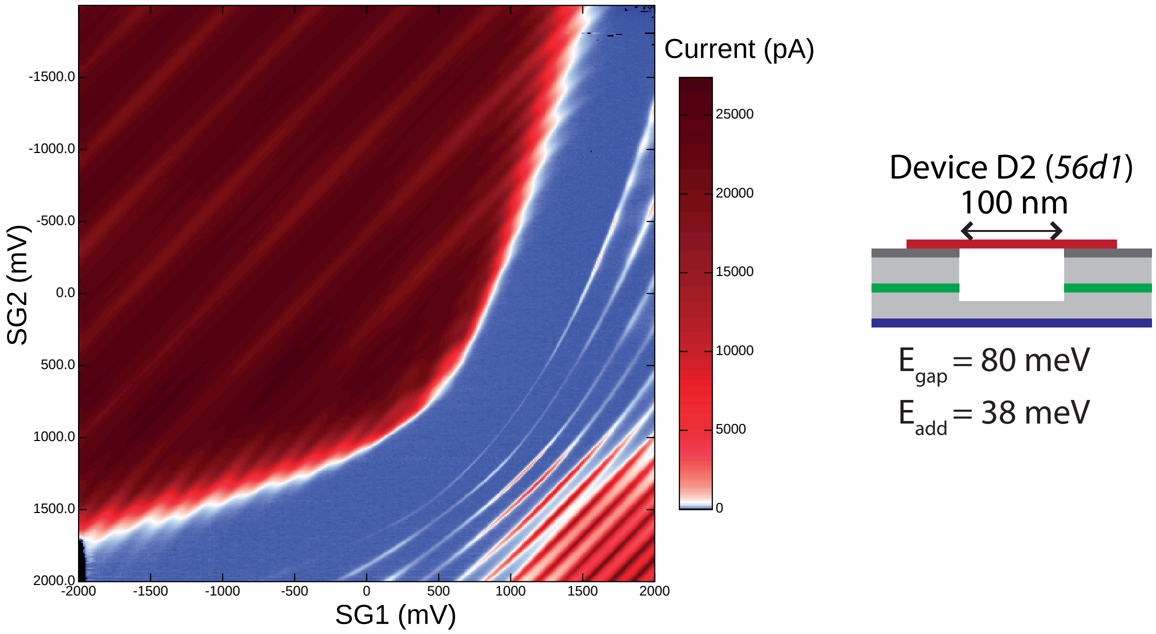

Figure 4.3: Device D2 Characteristics. *To the left a SGSG-plot of D2 at 1 mV bias is shown. To the right a schematic of device D2 (fabrication name 56d1) is drawn.*

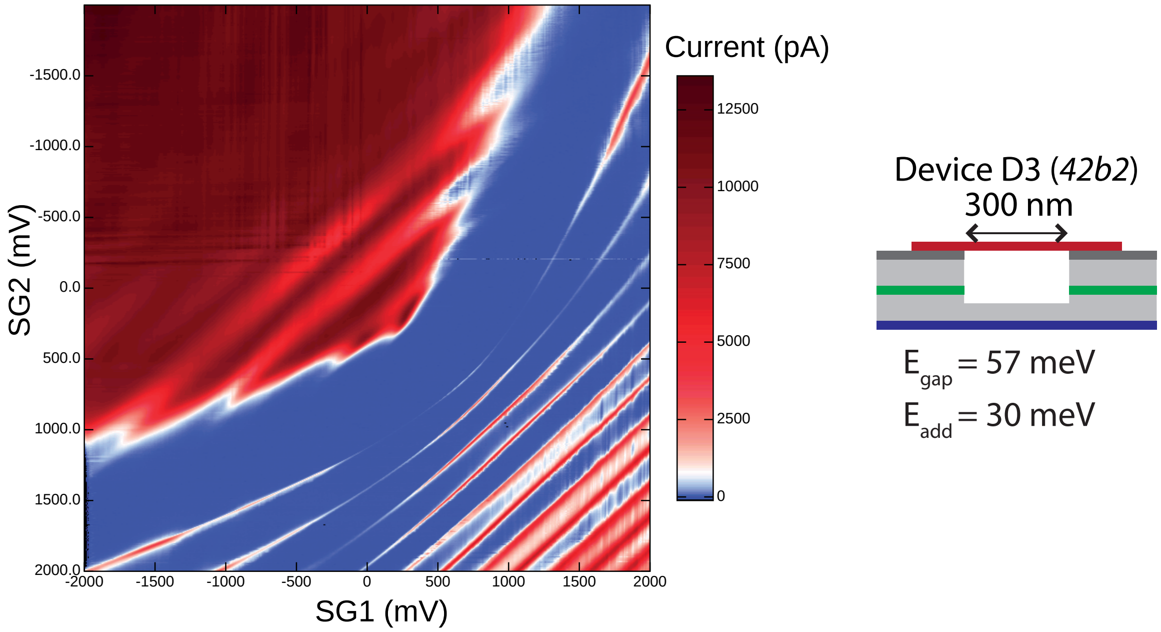

Figure 4.4: Device D3 Characteristics. *To the left a SGSG-plot of D3 at 1 mV bias is shown. To the right a schematic of device D3 (fabrication name 42b2) is drawn.*

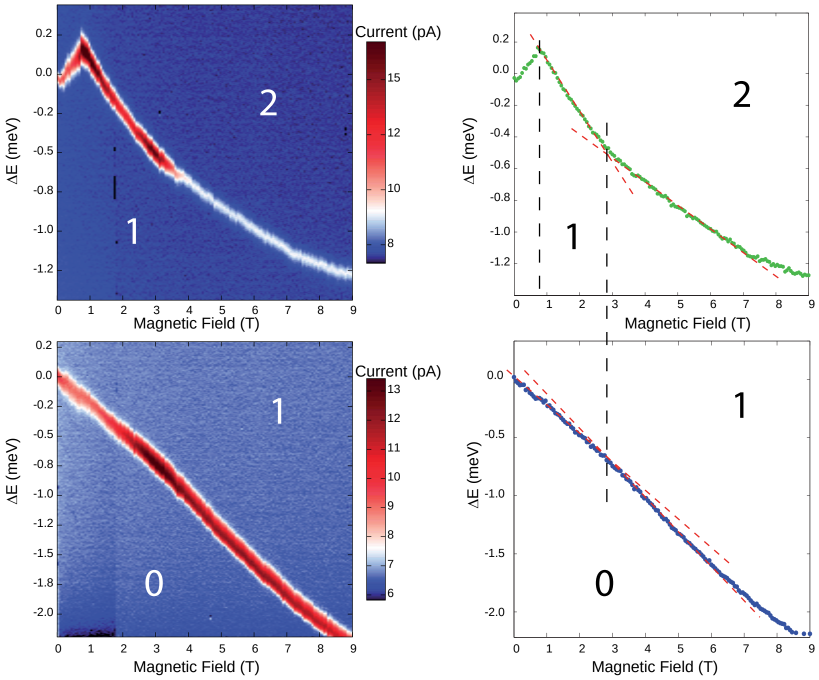

Figure 4.5: Spin-orbit effect in D1. *(Left) Groundstate energy difference as a function of magnetic field. At a fixed V_{SG1} voltage, V_{SG2} is swept in small steps across the Coulomb peaks of the first and second electron at 0.2 mV bias. Between each sweep the magnetic field was increased. The gate voltages were translated to energy using the α-factor, obtained from appendix D and corrected for sweeping only one gate. (Right) Extracted peak positions from the data, with the dashed lines indicating B_1 and B_2.*

The devices are identified by their trench as it was designed during fabrication, but from experience with previous samples it is suspected that the trench has become around 50 *nm* larger during the fabrication process.

4.2 Sign of the spin-orbit effect

The spin-orbit effect in CNT has only recently been discovered experimentally by Kuemmeth *et al.* (2008). This spin-orbit effect induced by the CNT curvature (see chapter 2.3.4) is usually so small that the effect can only be observed in very clean nanotubes devices. The crucial signature of the spin-orbit effect is that at low fields the second electron occupies the valley opposite to that of the first. This becomes apparent experimentally if the second electron state increases in energy with magnetic field, whereas it would move down in energy without the spin orbit coupling, as explained in the theory chapter (2.3.4). Here, we report measurements that demonstrate spin-orbit coupling in our devices. Furthermore, we find evidence that the sign of the spin orbit coupling can differ for different nanotubes and the amplitude can vary over an order of magnitude.

Device D1 exhibits the characteristic features of spin-orbit effect, seen in the groundstate magnetic field dependence of the first and second electron (figure 4.5). The first

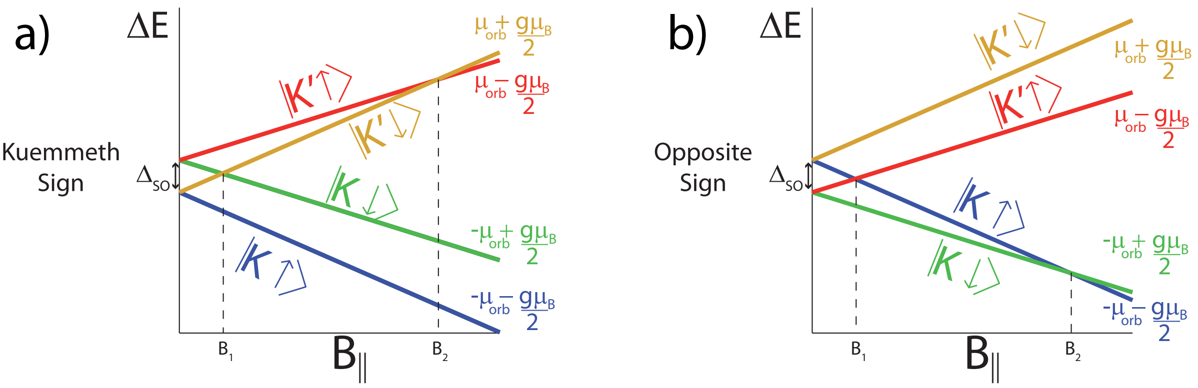

Figure 4.6: Spin-orbit effect with different sign. *(a,b) Schematic plot of the magnetic field dependence of one shell. (a) Initially* $|K'\downarrow\rangle$ *and* $|K\uparrow\rangle$ *have the lowest energy and a Zeeman-crossing is observed for electron three and four, as was originally observed by Kuemmeth* et al. *(2008). (b) The spin-orbit effect has an opposite sign, which means that* $|K'\uparrow\rangle$ *and* $|K\downarrow\rangle$ *have the lowest energy and the Zeeman crossing occurs for electron one and two.*

electron state moves down in energy with increasing field, but the second electron enters the other valley and moves up in energy with increasing field. At the field $B_1 = 0.8\ T$ the energy has increased half the associated spin-orbit energy, and the second electron changes valleys, thereby moving downward in energy. This directly gives a spin-orbit energy of Δ_{SO} of about $0.4\ meV$. A careful look at the first electron state reveals another crossing, indicated in the bottom right of figure 4.5. At the field $B_2 = 2.8\ T$, this second crossing occurs when the Zeeman energy becomes bigger than half the spin-orbit energy and the spin flips from down to up (see theory chapter (2.3.4) and figure 4.6). Note that to the first electron in the experiment always follows the lowest energy state. In this case the first electron follows the green line in figure 4.6(b) but switches to the blue line after the field B_2. The second electron follows the red line until a field of B_2 where it continues on the blue line and switches to the green line at B_2. From this spin-crossing, the spin-orbit energy can be determined and lies within the measurement error of the value obtained from the valley-crossing.

In contrast to the Zeeman-crossing B_2 observed here at the first and second electron, the first observations of the spin orbit effect by Kuemmeth *et al.* (2008) showed a Zeeman-crossing at the third and fourth electron (figure 4.6(a)). This can be interpreted as the spin-orbit coupling having the opposite sign compared to the work of Kuemmeth *et al.* (2008). The spin-orbit phase changes the $k_\perp$ interference condition, shifting the quantization lines in figure 2.14. The size and direction of this shift depend on the details of the circumference around the nanotube, which differs from nanotube to nanotube with its chirality. The resulting spin-orbit phase change could be either an addition or a subtraction to the phase acquired when the electron moves around the tube. If the resulting spin-orbit effective magnetic field points in the opposite direction for a device in comparison to Kuemmeths device, the opposite spins will be aligned with a given valley. This change in sign results in a Zeeman-crossing a the lowest two electrons instead of the highest two in the shell as is illustrated in figure 4.6(b).

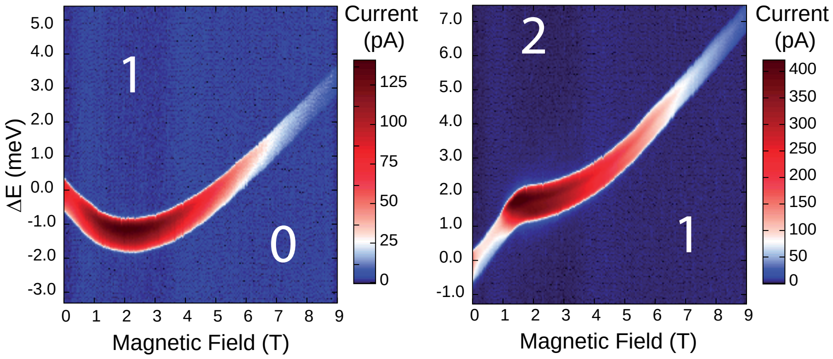

Figure 4.7: Spin-orbit effect in D2. *Groundstate energy difference as a function of magnetic field. Both split gates where swept symmetrically across the first and second Coulomb peak at a bias of 1 mV, increasing the magnetic field with each sweep.*

Device D2 also demonstrates clear spin-orbit behavior, as shown in figure 4.7. Again, spin-orbit effect is evident by the alternating slopes of the first and second electron groundstate at low fields. At a field $B_1 \sim 1.4\ T$, the second electron changes valleys, making the spin-orbit energy $\Delta_{SO} \sim 3.4\ meV$, which is an order of magnitude higher than measured before in D1 and by Kuemmeth *et al.* (2008). Unexpectedly, the first two electrons show a bending of the curves in figure 4.7. This indicates a crossing of the Dirac point, as will be discussed in the next section. For this device, we do not expect to see a Zeeman-crossing because it should be at very high fields for such a large spin-orbit energy. The slopes of the first two electrons, however, diverge with an energy in the order of the Zeeman energy. This divergence would be expected of a device with a spin-orbit effect with the same sign as in Kuemmeth's observations.

From these two devices and those measured by Kuemmeth *et al.* (2008), it can be concluded that the sign of the spin-orbit effect is device dependent. The sign and the amplitude of the spin-orbit effect depend on the details of the nanotube circumference. This can either results in an addition to the phase or a subtraction of the phase around the tube. Ultimately, the details of the nanotube circumference depend on the chirality of the CNT. In other words, the sign and amplitude of the spin-orbit effect are likely chirality dependent.

4.3 Turning Field: crossing the Dirac point

For our experiments, a magnetic field is applied along the axis of a CNT. As explained in the theory chapter, this will move one valley (K) down in energy and one valley up in energy (K'). For the valley going down (K) there is a minimum, however, because if it moves $E_{gap}/2$ down in energy, it will reach the bottom of the graphene cone, called the Dirac point (see figure 4.8). On reaching this point, the quantization line will continue moving in the same direction, meaning it will move up the cone at the other side, increasing its energy. Now the K valley will follow the same direction as the other valley K', which moved away from the Dirac point from the start. The magnetic field at which the Dirac point is reached depends on the speed of which the valley moves in energy with field μ_{orb},

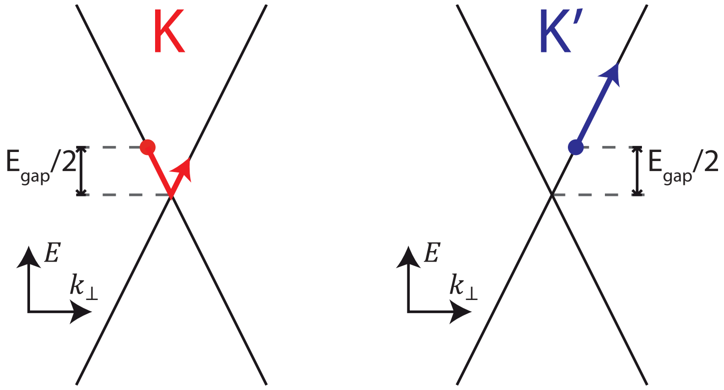

Figure 4.8: Crossing the Dirac point. *The two valleys K and K' move with field. If the K valley moves for $E_{gap}/2$ it will reach the bottom of the cone (Dirac point) and reverse its direction.*

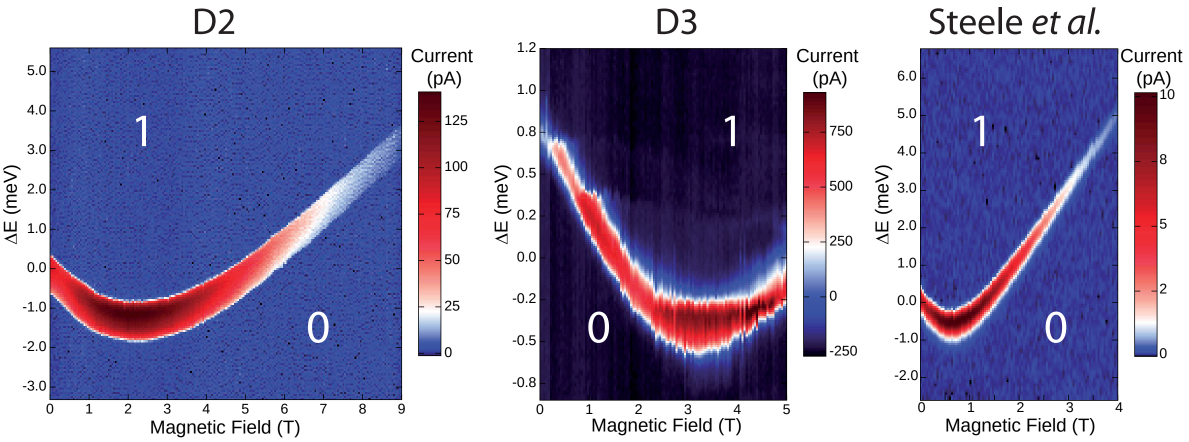

Figure 4.9: Crossing of the Dirac point for three different devices. *Gate traces at different magnetic fields. D2 has a 1 mV bias, D3 a 0.5 mV bias and for unpublished data of the device of Steele* et al. *(2009a) a bias of 0.4 mV was used. For all these devices a turning field is present at measurable fields.*

and the bandgap E_{gap} at zero magnetic field:

$$B_{dirac} = \frac{E_{gap}}{2\mu_{orb}} \tag{4.1}$$

In this experimental work, several devices are presented where a Dirac turning is present for observable fields. These fields are significantly less than expected from the bandgap obtained from the Coulomb diamonds, described in appendix D.

It was already seen in figure 4.7 of the previous section that device D2 shows a Dirac crossing at a measurable field. Such a turning field is observed in several devices, as is shown in figure 4.9. For D2 the valley reverses directions at a field of about $B_{turn} = 2.2\ T$ and for D3 this field is $B_{turn} = 3.2\ T$. Figure 4.9 also shows unpublished data from the device reported in Steele *et al.* (2009a), which has a turning field around $B_{turn} = 0.8\ T$. Such a turning field could also be caused by other effects that somehow reduce

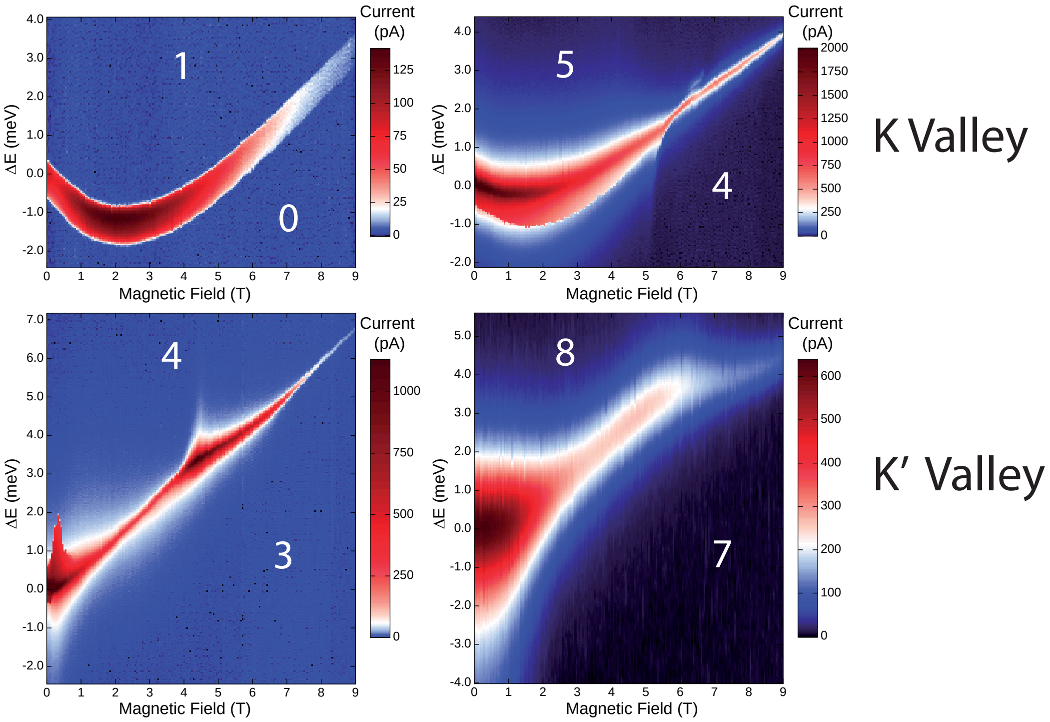

Figure 4.10: Observation of a turning field in higher shells. *First, fourth and fifth electron magnetic-field dependence at 1 mV bias, and eighth electron magnetic-field dependence at 0.07 mV. For the eighth electron, the Coulomb peak is very broad due to more open barriers. Electron 1 and 5 exhibit a turning field and electron 4 and 8 have a constant slope. The observation of such a turning field for higher shells demonstrates that this is indeed a crossing of the Dirac point of the graphene bandstructure.*

and increase the bandgap, so for this turning to be a Dirac turning, it is vital that *every electron in the K valley turns and every electron in the K’ valley does not.* For D2, it was possible to measure higher electron numbers, as shown in figure 4.10. Note that one shell consists of four electrons, so higher electrons are added to the next shell (see section 2.3.1). The fifth electron is equivalent to the first electron and the eight electron to the fourth, in the sense that they have the same valley and spin, but differ in $k_{\|}$. This plot shows data for the first and fifth electron, which are in the K valley and turn. Furthermore, it shows the fourth and eight electron, which do not turn but move straight up. This demonstrates that the turning field is an effect that indeed depends on the valley of the electron, confirming the interpretation of this crossing as a passing of the Dirac point of the graphene bandstructure.

The next issue that needs to be tackled is the very low value of the turning field compared to the expected value from the bandgap and orbital magnetic moment. For D2, the (maximum) slope of the first electron is $\mu_{orb} = 0.8\ meV/T$, which would imply a bandgap of $E_{gap}^{int} = 2\mu_{orb} \cdot B_{turn} \sim 4\ meV$, which is in stark contrast with the measured gap of $E_{gap}^{meas} = 80\ meV$. This is interpreted as a result of an ‘extrinsic’ bandgap that is added to the ‘intrinsic’ bandgap:

$$E_{gap}^{meas} = E_{gap}^{ext} + E_{gap}^{int}. \tag{4.2}$$

The intrinsic bandgap is the bandgap as derived in the theory chapter. The 'extrinsic' contribution to the gap E_{gap}^{ext} adds 76 meV to the total bandgap for this device, but does not otherwise seem to influence the bandstructure of the CNTs. An extrinsic contribution like this has been seen before by Deshpande *et al.* (2009), where they suggest this to be an effect of a Mott insulator . What this extrinsic contribution is and if it is really consistent with a Mott gap, is something that must be investigated further.

Such a large extrinsic bandgap is also seen in several other devices. For D3 in figure 4.9 the (maximum) slope is $\mu_{orb} = 0.6\ meV/T$ and the turning field is found at 3.2 T. This makes the intrinsic gap $E_{gap}^{int} \sim 4\ meV$, also significantly smaller than the measured gap of $E_{gap}^{meas} = 57\ meV$. For unpublished data of the device of Steele *et al.* (2009a), also shown in figure 4.9, a $\mu_{orb} = 1.8\ meV/T$ is found, together with $B_{turn} = 0.6\ T$. This makes the intrinsic bandgap $E_{gap}^{int} \sim 2\ meV$, for a measured gap of $E_{gap}^{meas} = 25\ meV$.

Now that it is established that one valley crosses the Dirac point, an important question arises, which has to do with the details of the movement through the Dirac-point. If one valley approaches the Dirac-point, its μ_{orb} will be constant, because the linearity of the Dirac-cone. If the valley crosses the Dirac point, the sign of μ_{orb} should be reversed in a sharp transition (figure 4.8). Why, then, do the measurements show a smooth transition, rather than a kink? This question will be answered in the next sections, when the influence of $k_{||}$ will be discussed.

Summarizing, this section showed devices for which the K valley turns at measurable fields. These turning fields are something happening only to the K valley and therefore can be interpreted in terms of the bandstructure of the CNT. The turning field is explained as a Dirac-crossing which occurs at low fields because the CNTs have a very small intrinsic bandgap with an unrelated extrinsic gap of unknown origin.

4.4 Magnetic field dependence of higher shells

Experimental research on the spin-orbit effect has been focusing mostly on the behavior of the first electron and its shell, because this is the easiest to understand. Here, the research is extended to include higher shells, with the initial goal of investigating the spin-orbit effect at these shells. What we find is that the measured shells show a magnetic field dependence that is significantly different from the first shell in the same device.

Figure 4.11 shows the gate traces of the first three shells and the eighth shell of device D2 as a function of magnetic field. For the first electrons of the first three shells, a turning field is visible. The second electron starts off in the K' valley and the third in the K valley, due to the spin-orbit effect, as discussed in the previous section. The peaks become broader for higher electron numbers because the barriers of the QD become more transparent. This is due to the change in dot size as discussed in appendix D.3. Also, a Kondo current becomes visible in the Coulomb blockade region at low field between the peaks around the gate voltages of 1900, 3300, and 3400 mV. Note that this Kondo current is visible because the bias voltage is close to zero but is lifted when a magnetic field is applied (which lifts the degeneracy of these states). For the eighth shell, a different pattern is visible where the turning field is absent. The behavior of the electron states for the subsequent higher shells is very similar to that of the eighth shell.

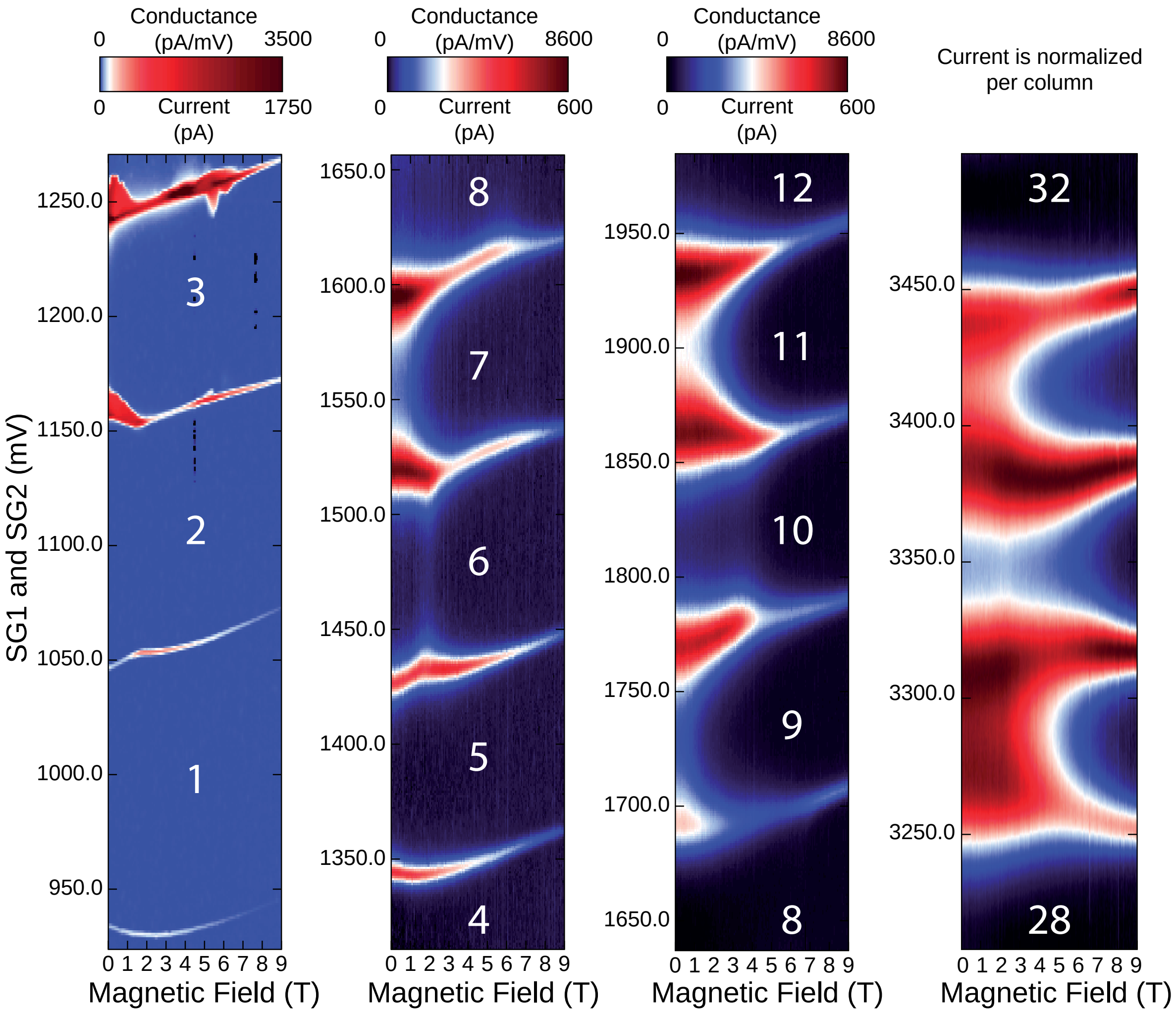

Figure 4.11: Magnetic field dependence of the first three shells for device D2. *Gate trace as a function of magnetic field for the first 12 electrons, together with electrons 29 to 32. Electrons 1 to 4 are taken with a 0.5 mV bias and 5 to 12, and 29 to 32, are taken with a bias of 0.07 mV. For electrons 28 to 32 the color scale is adjusted for better visibility per column.*

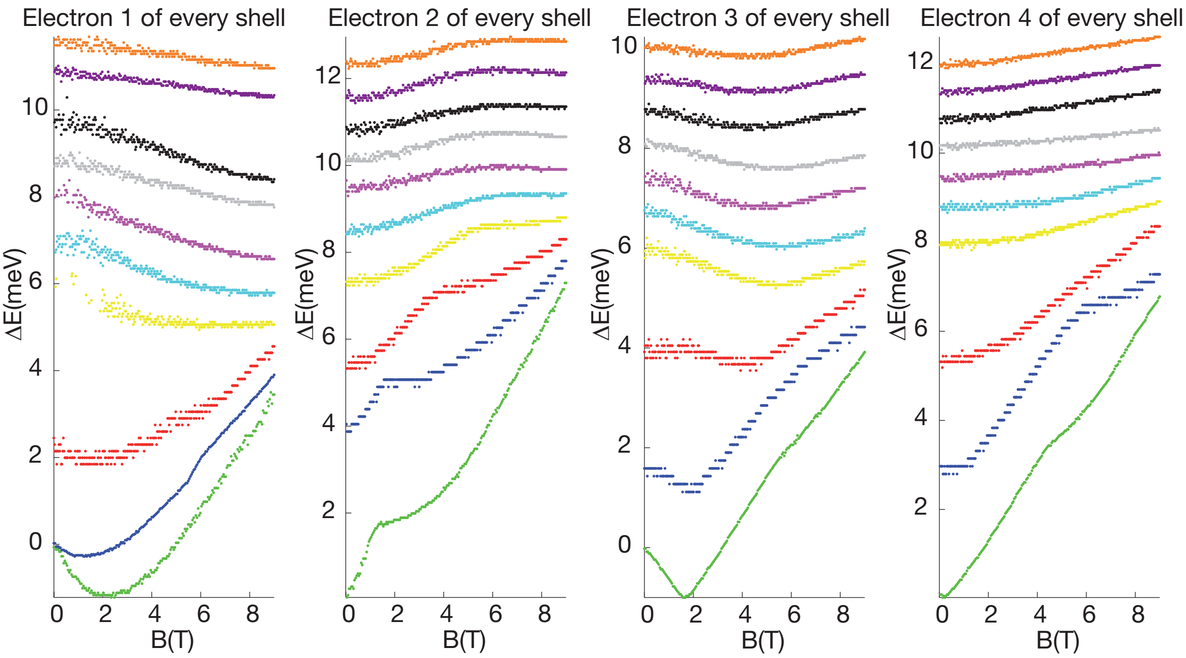

Figure 4.12: The shape of the magnetic curves change drastically for higher shells. *Extracted peaks for different electron number for the first 10 shells of device D2. Green is the first shell, blue the second, etcetera. The peaks are corrected for α-factor to be in the correct energy scale and the distance between the peaks is chosen for reasons of visualization.*

The magnetic field dependence of the peaks in figure 4.11 already shows a difference in shape from one shell to another, but if the peaks are corrected for the α-factor found from the Coulomb diamonds (see appendix D), this difference becomes much more dramatic (figure 4.12). The slopes of the peaks are reduced and after a few shells the turning field starts to disappear altogether. Due to the difficulty of extracting an accurate peak position for very broad peaks, the peaks data shown in figure 4.12 are not suited to do numerical fits, as explained in appendix D.5, but they do convincingly show that the slopes involved decrease significantly and the turning field disappears.

In order to demonstrate this more quantitatively, numbers for the slopes are extracted from the fourth electron of every shell, see figure 4.13. Only the fourth electron is used because these showed the clearest magnetic field curves and are unaffected by a turning field. From the data it looks like the μ_{orb}-slope is indeed disappearing, leaving only a slope of $0.08-0.09\ meV/T$, slightly higher than the slope resulting from Zeeman splitting ($g\mu_B/2 = 0.057\ meV/T$). This dramatic change in slope and shape of the magnetic field curves is unexpected, using the conventional model of the orbital magnetic moment in CNTs.

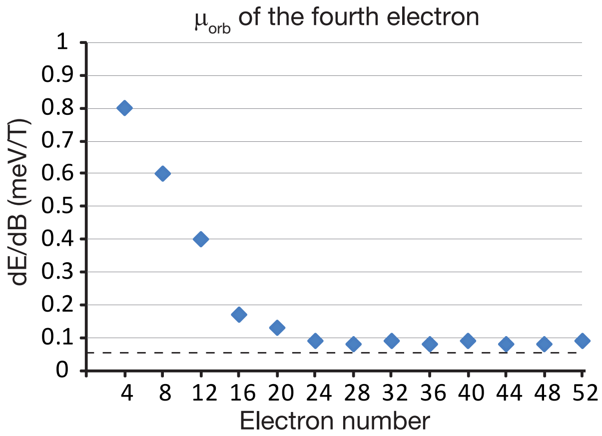

Figure 4.13: Magnetic-field slope goes down with electron number. *Magnetic field dependence as a function of electron number, obtained from the fourth electron of each shell. The dotted black line indicates the Zeeman-slope.*

4.5 Orbital magnetic moments in CNTs at very small intrinsic bandgap

Until now, two observations remained unexplained. First, a smooth Dirac-crossing was measured where a kink would be expected. Second, μ_{orb} was strongly suppressed for higher electron numbers. In this section these two observation will be explained by looking at both small $k_{\|}$ and $k_{\perp}$. All data published previously is in the limit of $k_{\perp}^{0} >> k_{\|}^{0}$ while the devices presented here have $k_{\perp}^{0} \sim k_{\|}^{0}$, due to the small intrinsic bandgap implied by the low field for which the Dirac point is crossed. This much smaller $k_{\perp}^{0}$ drastically changes the orbital magnetic field effects in CNTs. To understand the effects of a parallel magnetic field on a device with both small $k_{\perp}$ and $k_{\|}$, the electronic levels need to be rederived from the CNT bandstructure with this in mind. From this derivation and the data it will become apparent that the simple expression for the magnetic moment $\mu = Dev_f/d$ (equation 2.19), used extensively in the literature, see for instance Minot *et al.* (2004), Jarillo-Herrero *et al.* (2005b), Jarillo-Herrero *et al.* (2005a), Kuemmeth *et al.* (2008) and Hüttel *et al.* (2009), is no longer valid for the $k_{\perp} \sim k_{\|}$ limit.

Again, the starting point of the derivation is the Dirac cone

$$E(k_{\perp}, k_{\|}) = \hbar\, v_f \sqrt{k_{\perp}^2 + k_{\|}^2} \tag{4.3}$$

A $k_{\perp}$ quantization is introduced by rolling up a graphene sheet and forming a carbon nanotube. The distance between the first quantization line and the Dirac point in the cone is $k_{\perp}^{0}$, which depends on the wrapping vector. The point on this line where a certain electron level is placed is determined by $k_{\|}$, whose value depends on the number of electrons in the dot and longitodunal level spacing. The resulting bandstructure is shown in figure 4.14.

There are two mechanism that shift the quantization line by changing $k_{\perp}$, see figure 4.15. The first is magnetic field which shifts $k_{\perp}$ with $s_v \frac{\delta k_{\perp}}{\delta B} \cdot B$, where s_v is the valley K or

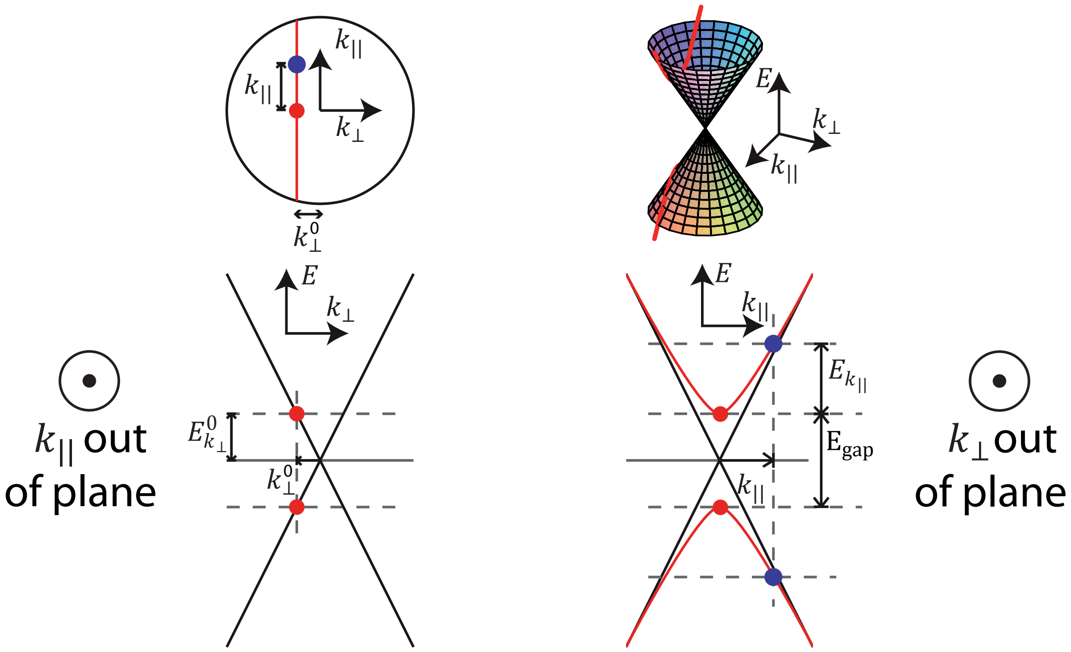

Figure 4.14: Bandstructure of a carbon nanotube in the graphene bandstructure. *The top right shows a 3-D visualization of the bandstructure around the Dirac point of graphene. In red the (1-D) bandstructure of a CNT is given. At the top left a top view of the graphene-cone is shown with a red dot at the bottom of the CNT bandstructure and blue dots at the position of an electron-level. The bottom left picture is a cut of the cone along the* $k_{\perp}$ *axis and the bottom right is a cut along the* $k_{||}$ *axis.*

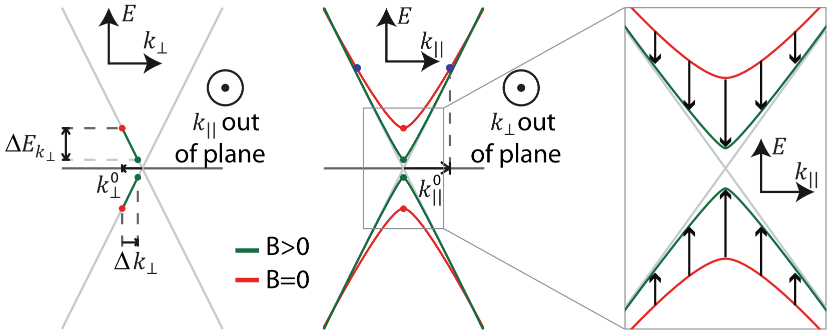

Figure 4.15: Movement of the CNT bandstructure trough the Dirac cone. *The left figure is a cut of the cone along the* $k_{\perp}$ *axis and the middle figure is a cut along the* $k_{||}$ *axis. When* $k_{\perp}$ *changes, the bandgap shifts in the cone, drawn here as a shift from the red curve to the green curve, see figure 4.14. The right figures gives a zoom for the cut along the* $k_{||}$*. The value of* $k_{||}$ *determines the size of the change in energy with field, indicated by the arrows.*

K' and can take the values 1 or -1, and B is the magnetic field. The second mechanism is the spin-orbit coupling. This coupling generates an effective magnetic field, which again results in an additional shift depending on the interaction between valley and spin. This is modeled in the term $-s_v * s_s \cdot k_{SO}$, where s_s gives the spin of the electron and is either 1 or -1, and k_{SO} is the quantization-line displacement due to the spin-orbit coupling, see figure 2.17(a). Substituting these terms for $k_\perp$ into the graphene bandstructure from equation 4.3 gives

$$E(k_{||},B) = \hbar\, v_f \sqrt{(k_\perp^0 + s_v \frac{\delta k_\perp}{\delta B} \cdot B - s_v s_s \cdot k_{SO})^2 + k_{||}^2}, \tag{4.4}$$

and the states of one shell are denoted as

Label	(s_v,s_s)
$\vert K\uparrow\rangle$	(-1,-1)
$\vert K\downarrow\rangle$	(-1,1)
$\vert K'\uparrow\rangle$	(1,-1)
$\vert K'\downarrow\rangle$	(1,1)

.

Now the above equation can be expressed in measurable quantities by taking $\mu' = \hbar\, v_f\, \frac{\delta k_\perp}{\delta B}$ as the change in energy with magnetic field *if* $k_{||}$ *and* Δ_{SO} *are both zero*. Furthermore, $E_{k\perp}^0 = \hbar\, v_f \cdot k_\perp^0$ is the energy difference between the bottom of the graphene cone and the bottom of the CNT line, see figure 4.14. The spin-orbit contribution $\frac{1}{2}\Delta_{SO} = \hbar\, v_f \cdot k_{SO}$ is the effective spin-orbit displacement in k-space translated in energy for $k_{||} = 0$. Note that the factor of 1/2 is put here to stick to the definition of Kuemmeth. To express $k_{||}$ as an energy, equation 4.3 can be used to get:

$$(\hbar\, v_f k_{||})^2 = (E_{k\perp}^0 + E_{k||})^2 - (E_{k\perp}^0)^2 = (E_{k||})^2 + 2E_{k\perp}^0 E_{k||} \tag{4.5}$$

where $E_{k||}$ is the energy from the bottom of the CNT band at zero magnetic field. All this is summarized in figure 4.14 and changes equation 4.4 into

$$\begin{aligned} E(E_{k||},B) \;&=\; \sqrt{(E_{k\perp}^0 + s_v \mu' B - s_v s_s \cdot \frac{1}{2}\Delta_{SO})^2 + (E_{k||})^2 + 2E_{k\perp}^0 E_{k||}} \\ &\quad + s_s \frac{g\mu_B}{2} \cdot B, \end{aligned} \tag{4.6}$$

where the last term is the Zeeman contribution.

From equation 4.4 it becomes clear that the ratio between $k_\perp^0$ and $k_{||}$ is important for the shape of the magnetic field curve (as in figure 4.12). Figure 4.15 shows that a higher $k_{||}$ moves the energy state higher in the bandstructure. If a magnetic field is applied, $k_\perp$ changes and the lowest parts of the bandstructure have a significantly bigger change in energy than points higher up in the curve (arrows in figure 4.15). Higher shells have higher values for $k_{||}$ so these also have a smaller change in energy with magnetic field.

This $k_{||}$-dependence also applies to the shape of the kink. Basically, the state traces a curve through a cone and $k_{||}$ determines where this cut is taken, whereas $k_\perp$ determines where the curve starts. A smooth Dirac-crossing therefore occurs because $k_{||}$ has a finite

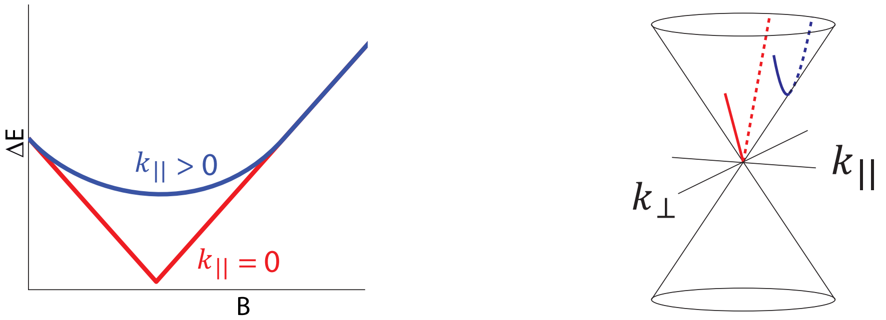

Figure 4.16: Crossing of the Dirac cone at different values of $k_{||}$. *Magnetic-field curves of energy states in CNTs. The Dirac crossing can be either a kink if $k_{||} = 0$ or a smooth transition for $k_{||} > 0$, shown left. This can be visualized in the Dirac-cone on the right, where $k_{||}$ determines where the cone is cut.*

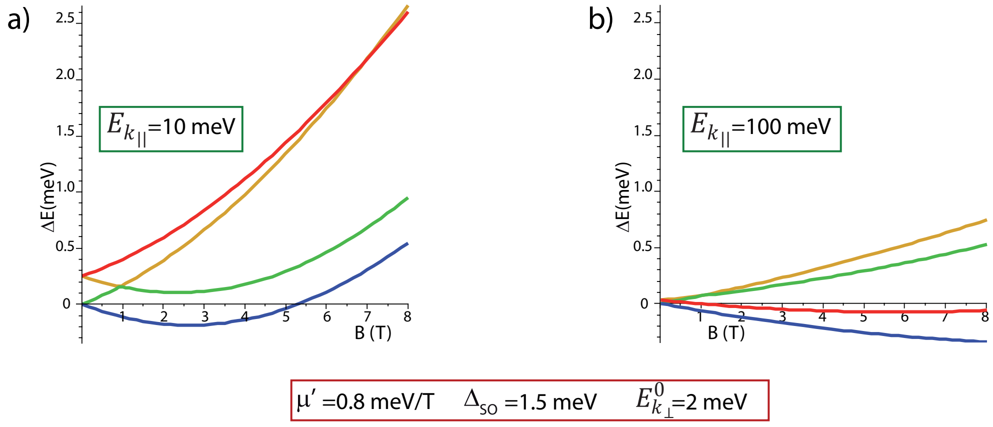

Figure 4.17: Shells with higher $k_{||}$ have lower μ_{orb}. *Plots of equation 4.6 for a shell with values chosen to fit the data of device D2, as indicated in the red box. (a) Magnetic field dependence for a low $k_{||}$ corresponding to a low electron number. (b) Magnetic field depedence for a big $k_{||}$ which is equivalent with a large electron number.*

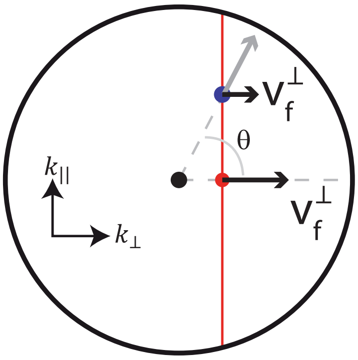

Figure 4.18: Higher $k_{\|}$ results in lower $v_{f\perp}$. *A topview of the Dirac cone with the CNT quantization shown in red. For $k_{\|} = 0$ (red dot), where $v_{f\perp}$ equals the slope of the Dirac cone v_f. For $k_{\|} > 0$ (blue dot), $v_{f\perp}$ is only a component of v_f, determined by the angle θ.*

value and the state does not cut the Dirac cone exactly in the middle. For $k_{\|}$ approaching zero, the transition will start to resemble a kink. This is visualized in figure 4.16.

Figure 4.17(a) shows a plot obtained from equation 4.6, for a shell with values chosen to fit the first shell data of D2. This plot is very similar to the measured data. If the value for $E_{k_{\|}}$ is increased, plot 4.17(b) is obtained. Here, the turning field disappears and the slopes become significantly smaller, similar to what was observed for the higher shells of D2. A numerical fit of the data failed because with the addition of an electron the dot size changes (appendix D), also influencing $k_{\|}$ in an unknown amount.

From these plots we can conclude that equation 4.4 and 4.6 describe the measured data, in particular the turning field and the change in slope. Both $k_{\perp}^{0}$ and $k_{\|}$ are important in the description of the magnetic field dependence. $k_{\perp}^{0}$ determines whether a turning field can be reached, and $k_{\|}$ determines the size of the slopes. In the limit of $k_{\|} >> k_{\perp}^{0}$ the orbital contribution to the slopes disappears altogether. $\mu_{orb} = Dev_f/d$ (equation 2.19) is only valid for $k_{\|} = 0$ (or in the limit if $k_{\|} << k_{\perp}^{0}$) and is equal to μ' in equation 4.6.

The reduced orbital moment can also be explained in a semi-classical way. In the semi-classical picture of section 2.3.3, an electron in a valley circles the nanotube and the field couples to this motion, via the formula $\mu_{orb} = Dev_f/d$. We have already established that this formula is only valid for $k_{\|} << k_{\perp}^{0}$. It is important to note that the field only couples to motion along the circumference of the nanotube and therefore the Fermi-velocity meant there is actually the component of this Fermi-velocity around the tube $v_f^{\perp} = \hbar^{-1}\delta E/\delta k_{\perp}$. Figure 4.18 shows a top view of the Dirac cone, where $v_f^{\perp}$ is shown as the component of the graphene Fermi velocity which is constant in the radial direction, and can be calculated as

$$\begin{aligned} v_f^{\perp} &= v_f cos(\theta) \\ \mu_{orb} &= \frac{Dev_f}{4} \cdot \sqrt{\frac{1}{1+(k_{\|}/k_{\perp})^2}}. \end{aligned} \tag{4.7}$$

With this modification, the orbital magnetic moment becomes dependent on the ratio between $k_{\|}$ and $k_{\perp}$ as it should be. Furthermore, if the Dirac point is crossed, this expression shows the observed smooth crossing instead of a sharp kink.

4.6 Unexplained effects at large electron and hole numbers

In the last section it was explained why a turning field was visible and why it would disappear. Furthermore, it was established that the orbital magnetic moment should decrease for higher electron numbers. The higher shells, however, show behavior that can not be fully explained. Here, we discuss measurements for many electrons (60), and also for a large (but undetermined) number of holes. (See appendix D.3 for a discussion of doping device D2 with holes.)

Unexpectedly strong suppression of μ_{orb}

Figure 4.19(a) shows three of the higher electron shells. Very similar figures can be obtained from all shells of more than 24 electrons. The difference in slopes (energy splitting) between the 61st peak and 62nd peaks is about $210\mu eV/T$. Similar values are obtained by subtracting the 63rd and 64th peak, etcetera. Subtracting this value by the Zeeman splitting of $116\mu eV/T$, leaves a orbital splitting of $2\mu_{orb} = 100\mu eV/T$. In the previous section, it was shown that μ_{orb} could be suppressed by a large $k_{\|}$. From the level spacing of $\Delta \sim 3.2\ meV$, we obtain $E_{k_{\|}} \sim 20\ meV$ at a filling of 24 electrons (six shells times the level spacing). However, from the theory of the previous section, we would require an $E_{k_{\|}}$ of around 100 meV to achieve the observed suppression of μ_{orb}, as is shown in 4.17(b). (For this estimate, we used an $E_{k_{\perp}^0}$ of a few meV, obtained from the turning field, as shown in figure 4.17(a)). Thus, the magnitude of the suppression of μ_{orb} in higher shells cannot be understood in our current model.

Big value, constant magnetic-field slope for higher shells

Apart from the suppression of μ_{orb} at unexpectedly low $k_{\|}$, both the high electron number and high hole number shells (figure 4.19) have a magnetic-field slope that does not change from shell to shell. If this slope still has a significant μ_{orb} contribution, it should decrease further for higher shells, which it does not. One possible explanation is that the orbital magnetic moment has actually completely vanished, and these slopes contain only a Zeeman splitting of $\sim 210\mu eV/T$ corresponding to an anomalously large electron g-factor of 4 (instead of 2). However, there is no clear reason why we would expect g=4, since it has never been observed before in CNTs (Charlier *et al.* (2007)), so it is likely that the splitting between the peaks also includes a contribution from μ_{orb} which has not only been more strongly suppressed than expected, but has also become independent of $k_{\|}$. Such effects cannot be understood in the theory of section 4.5.

To experimentally rule out the possibility that what we observe is a Zeeman splitting with an anomalously large g-factor, the direction of the magnetic field needs to be changed, which was not possible for the experimental setup used in this thesis. The parallel magnetic field used to obtain figure 4.19, for example, should be turned towards a field that points perpendicular to the nanotube axis. For this perpendicular field, the μ_{orb} contribution is gone, leaving only the Zeeman contribution.

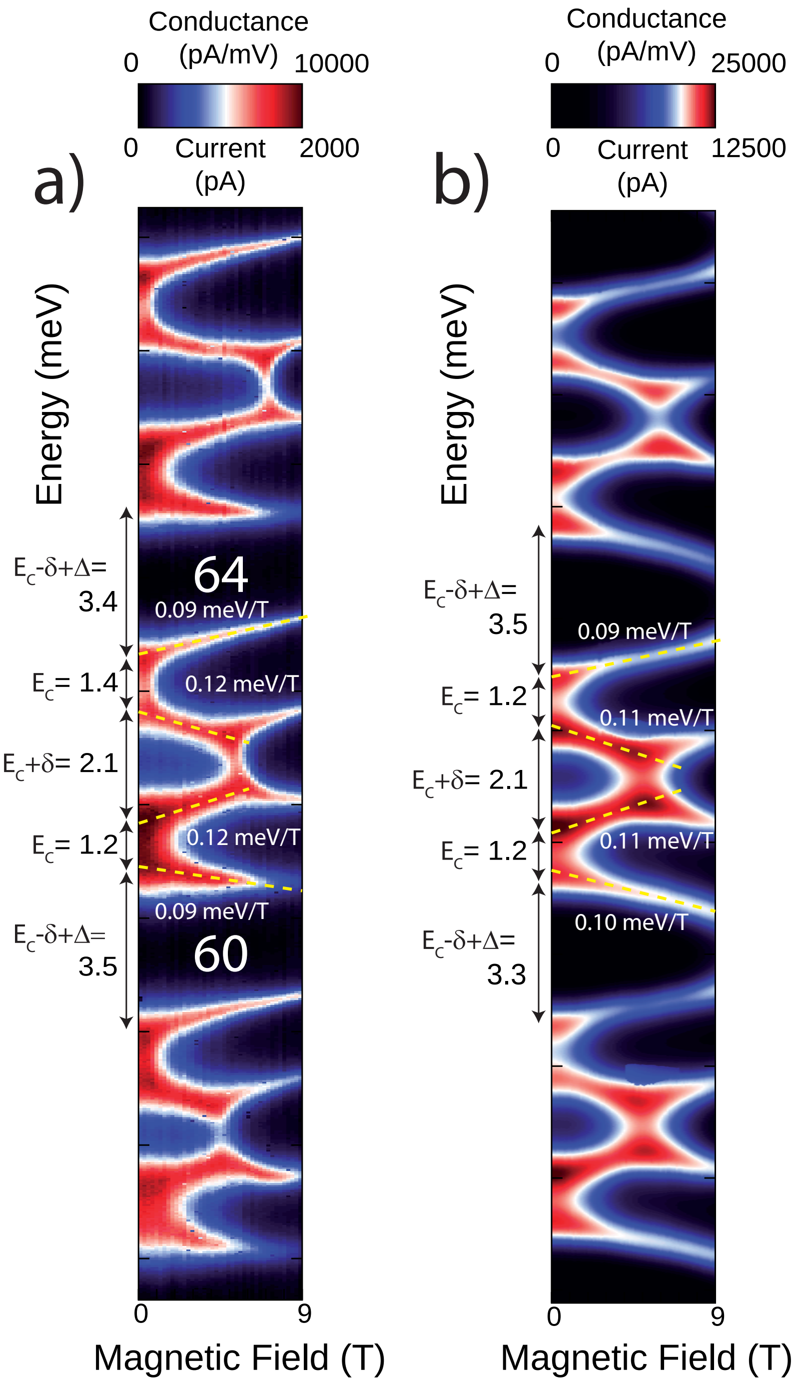

Figure 4.19: Magnetic field dependence for many electrons and many holes. *(a) Magnetic field dependence for the three highest shells measured for D2 at a bias of 0.2 mV. In white a few electron numbers are indicated. The α-factor is approximately constant for these electrons and is used to get an approximate energy scale. (b) Magnetic field dependence for three shells when the quantum dot is filled with holes, for a bias of 0.5 mV. The exact number of holes is unknown. Again the α-factor is constant over this range and is used to obtain the energy scale.*

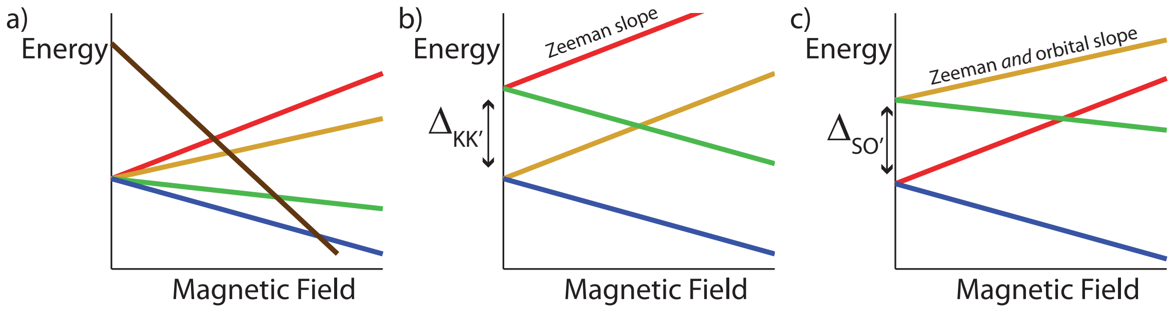

Figure 4.20: Three possible explanations for the high field crossing. *(a) A higher quantum level crosses with the states. This would result in a visible crossing for the fourth electron of the shell. (b) The orbital magnetic moment has vanished and the crossing is caused by KK' splitting. The slopes contain only a Zeeman contribution and are mixed K and K' valley states. (c) The crossing is caused by spin-orbit splitting and the slopes have both a Zeeman and an orbital contribution.*

High field crossing

Another feature in the shells of figure 4.19 is the crossing at high fields for the middle two peaks in each shell.

A first possible cause of this crossing could be a 'level' crossing. This would mean that a state of a higher shell crosses with these states, see 4.20(a). If this would be the case, this crossing should also be visible in the fourth electron of the shell, since this state should be crossed first. We can therefore discount a level crossing.

A second possible case would be that KK'-mixing causes the crossing. This implies that no orbital magnetic moment is present and the slope only has a Zeeman contribution with a g of 4 due to something we do not understand. In that case a splitting of $\delta = \Delta_{KK'} = 0.8 - 0.9\ meV$ is caused by valley-mixing and the high field crossing occurs when the Zeeman-splitting overcomes the KK'-mixing energy $\Delta_{KK'}$, see 4.20(b). However, this increased g-factor is unlikely as explained above, thus ruling out KK'-mixing.

The third option would be that the crossing is caused by the spin-orbit effect, just like it did for the low field crossing at the few electron regime 2.17. This would mean that $\delta = \Delta_{SO} = 0.8 - 0.9\ meV$, see figure 4.20(c). But, because $\mu_{orb} \sim 0.05\ meV/T$, the corresponding k_{SO} must be about ten times as big as it was for the few electron regime, to result in the same energy splitting. In other words, the spin-orbit coupling has to increase for higher $k_{||}$ values to result in the same splitting Δ_{SO} for peaks with a suppressed μ_{orb}. In the picture presented above (based on Ando (2000) and Kuemmeth *et al.* (2008)), k_{SO} is a constant phase change due to the movement of the electron through the p_z orbitals, and should not change with electron number. This means that the resulting spin-orbit energy Δ_{SO} should be reduced together with the orbital magnetic moment. One possible explanation is given by Izumida *et al.* (2009), where they report an additional term outside of the square root of equation 4.6, which would not depend on $k_{||}$ or $k_{\perp}$. Our observation of a spin-orbit splitting that is not suppressed along with the orbital magnetic moment suggests the presence of such an Izumida-style spin-orbit term in this device, with a magnitude of $\sim 0.8 meV$. Further evidence of such a spin-orbit term comes from the turning fields of the second electron in the first shell. As can be seen in figure 4.17, the inclusion of an Ando/Kuemmeth term gives a different turning field for the first and second electron. However, in our data shown in figure 4.11 and 4.12, it can be seen that the first and second electron have very similar turning fields, which points to a large Izumida-type spin orbit coupling.

To summarize, a crossing at high magnetic field and high electron number could be an indication of an Izumida-style spin-orbit coupling. The anomalously strong suppression of μ_{orb} and the unexpected high constant value of the remaining magnetic-field slope, however, remain a mystery and cannot be explained by the model described here.

Chapter 5

Conclusions and recommendations

5.1 Conclusions

The physics of carbon nanotube quantum dots (CNT-QDs) were experimentally investigated by performing current measurements as a function of both gates and magnetic field.

Spin-orbit effect

The first conclusion can be drawn about the spin-orbit effect. This coupling is caused by the spin-dependent phase accumulated when an electron moves around the circumference of the nanotube in a valley-dependent direction. Spin-orbit energies of 0.4 meV and 3.4 meV were measured, confirming that this spin-orbit coupling exists in carbon nanotubes and can be very strong. Secondly, both the magnitude and sign of the spin-orbit coupling varies from device to device. The most likely explanation is that it is related to the chiral vector of the nanotube.

Dirac-crossing

For one valley, the Dirac-point can be crossed at fields significantly lower than expected from the bandgap obtained from Coulomb diamond measurements. This implies the presence of an extrinsic contribution to the bandgap that does not depend on the graphene-derived bandstructure.

Suppressed orbital magnetic moment

The orbital magnetic moment μ_{orb} depends on the ratio between the wavevector parallel to the tube, $k_{||}$, and the wavevector pointing around the tube, $k_{\perp}$. The orbital magnetic moment is suppressed if $k_{||}$ increases from $k_{||} << k_{\perp}$ to $k_{||} \sim k_{\perp}$ and vanishes in the limit of $k_{||} >> k_{\perp}$.

Limit of large $k_{||}$

High shells (large $k_{||}$) show behavior which is not completely understood. Indications have been found that an Izumida *et al.* (2009) style spin-orbit interaction needs to be taken into account. Furthermore it remains unclear how big the separate contributions of spin and valley splitting are to the magnetic-field dependence of the electron states. Why the orbital magnetic moment is suppressed so strongly, and why this suppression becomes independent of $k_{||}$, is also not understood.

5.2 Recommendations

A few recommendations can be made for further research.

Vector magnet

To investigate the separate spin and valley contributions to the magnetic field dependence of the electron states, a vector magnet can be used. As explained in section 4.6, tuning the magnetic field from parallel to the tube axis to perpendicular would reveal the different contributions.

Interacting electrons

In order to get a better understanding of the many electron regime, it might be a good idea to look to theories about (strongly) interacting systems, such as Luttinger liquid. In Luttinger liquids, individual quantum states of spin, valley, and orbital excitations become mixed, and the elementary excitations no longer look simply like electrons with a given charge, spin, and valley quantum number (Auslaender *et al.* (2005)). The failure of our model based on shell filling of single particle states could indicate that Luttinger liquid theory may be necessary to describe the many electron regime.

Tunable barriers and mechanics

A new device should be designed that can tune the barriers separately. In that case, the barriers can be tuned to a regime where Kondo and mechanics are suppressed. To suppress the mechanics it might also be better to have non-suspended devices.

Spin-qubits

In spite of the things that are not understood, this thesis gives a intuitive picture of the spin-physics of CNT-QDs. This picture provides a basis for understanding the spin physics of carbon nanotube devices experimentally, and it should now be possible to work towards developing spin-qubits. Some unclear details that remain in the interpretation presented here will probably become clear when studying the future spin qubit devices.

Appendix A

Bandstructure of graphene

This appendix gives a detailed derivation of the bandstructure of graphene. This derivation uses the tight-binding method or Linear Combination of Atomic Orbitals (LCAO) and is based on an exercise by Schönenberger (2000).

A.1 Atomic structure of graphene

Figure A.1 shows a picture of the atomic structure of graphene in its honeycomb lattice. The carbon atoms of graphene have four valence electrons but only three are used to form sp^2 bonds with their neighbors in the x-y plane, meaning that each atom has one free electron left for electronic transport. This last electron is used for the p_z orbital (where z is the dimension perpendicular to the graphene plane).

A lattice is by definition a regular rectangular roster of repeated patterns. The regular rectangular roster is called a Bravais-lattice in solid state physics, and the repeated pattern is called a unit-cell. The unit-cell can be of any size, as long as the pattern is repeated.

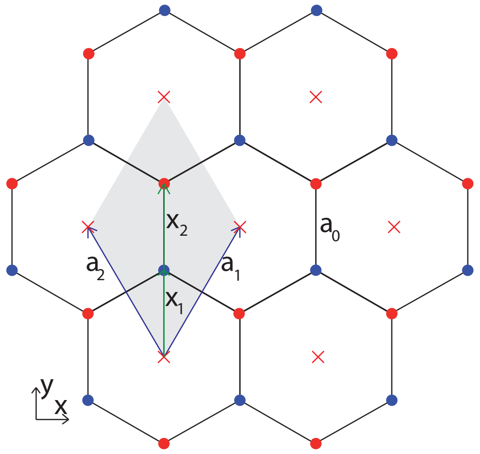

Figure A.1: *Atomic structure of graphene, with the unit-cell and corresponding lattice vectors. The nearest neighbor distance is* $a_0 = 1.42 \cdot 10^{-10} m$.

A choice for a unit-cell in graphene could be a few honeycombs (in such a way that the neighboring cell do not overlap), but this unit-cell would contain some repeated patterns itself. The smallest possible unit-cell is called the primitive unit-cell, and is the one that cannot be reduced to smaller cells. In the graphene case the primitive unit-cell contains two atoms. (Another way to look at this is that there are two Bravais lattices interposed.) The origins of each unit-cell form a Bravais lattice and are called lattice points. The position of the atoms in the unit-cell in relation to the origin of the unit-cell (or lattice point) are called base vectors. The vectors along which the origin of the unit-cell is moved to another origin are called the lattice vectors and these define the lattice.

The lattice vector for graphene, with $a = \sqrt{3}a_0$, are

$$\vec{a_1} = a \begin{bmatrix} 1/2 \\ \sqrt{3}/2 \end{bmatrix}, \quad \vec{a_2} = a \begin{bmatrix} -1/2 \\ \sqrt{3}/2 \end{bmatrix} \tag{A.1}$$

with the base vectors

$$\vec{x_1} = \begin{bmatrix} 0 \\ a_0 \end{bmatrix}, \quad \vec{x_2} = \begin{bmatrix} 0 \\ 2a_0 \end{bmatrix} \tag{A.2}$$

There is another lattice geometry that is of particular interest: the Wigner-Seitz (WS) cell. The WS-cell is created by connecting all the lines going perpendicular through the midpoint of the lines connecting the lattice points, as is done in figure A.2. The WS-cell contains all the symmetries the lattice itself has. Furthermore, it contains all the points closest to the lattice point. From the figure we see that the lattice is rotational symmetric over 60°. The concept of the WS-cell will be used again later on to determine the Brillouin zone.

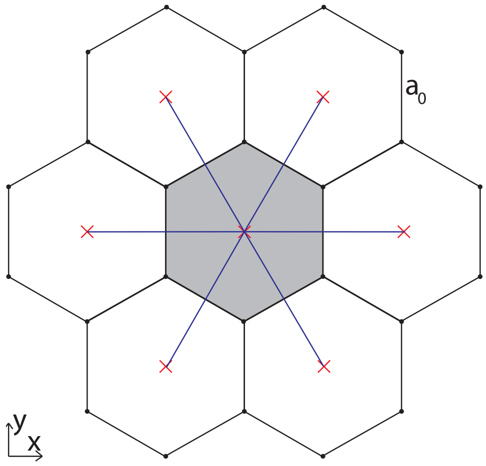

Figure A.2: *Wigner-Seitz cell for the graphene lattice. It turns out that trough the choice of the origin of the unit-cell, the Wigner-Seitz cell is exactly one honeycomb.*

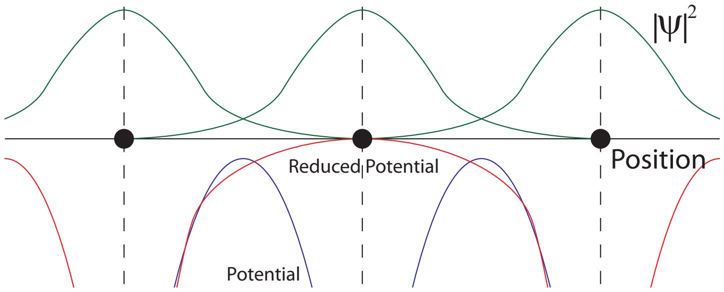

Figure A.3: *The tight binding view of a solid in a 1-d lattice. Below the axis the potential is visualized and above the axis the atomic orbitals are showed. In red the potential is showed, corrected to exclude the contribution of one atom.*

A.2 The tight-binding approach

Because of the symmetry of the lattice a symmetry of the physics is inevitable. If one moves from one lattice point to the next and assumes that the boundaries of the lattice are very far away (e.g. infinit lattice), the physical environment is exactly the same. A translation operator for a state is given by $Tr = e^{-\frac{i}{\hbar}\hat{p}\cdot\vec{R}}$, where $\vec{R}$ is the distance translated. When $\vec{R}$ equals one of the lattice vectors, the physics should not change and therefore the translation operator should commute with the Hamiltonian of the system, and consequently have the same eigenstates.

To get the eigenstates of the system the tight-binding method is used. If a valence electron is (loosely) bound to a carbon atom in free space it has an orbital wavefunction ϕ_{atom}. The tight-binding approach assumes these orbitals don not change much when the carbon atom is placed in a lattice. A valence electron in the lattice will therefore move to an atom, circle a few orbitals for that atom and move on to the next. An electron will effectively only see the potential of the atom closest to it and the orbitals will only overlap slightly. This is visualized in figure A.3.

The total wavefunction will be a linear combination of all the atomic orbitals, where in the weights of this linear combination the overlap between the orbitals will be taken into account. The atomic orbitals at the different lattice sites are given by $\phi(\vec{x}-\vec{R})$, where $\vec{R} \in G$ and G is the collection of all latticepoints. Note that the atomic orbitals are already solutions of the Hamiltonian of an atom in free space (with the corresponding potential). The total correction to the atomic-wavefunctions must therefore be calculated for a potential that is the lattice potential without the potential belonging to the atom where the electron is located. This is also visualized in A.3. The goal of the tight binding is to calculate the perturbation that arise by the small overlap between the different orbitals.

Unfortunately, when the tight-binding approach is applied to graphene, each unit-cell contains two atoms and therefore two atomic orbitals, so this makes the problem more complicated. The unit-cell equivalent atomic orbital ϕ of the lattice point is again a linear combination of the two real atomic orbitals of the two atoms:

$$\boxed{\phi(\vec{x}) = c_1\phi_1(\vec{x}) + c_2\phi_2(\vec{x})} \tag{A.3}$$

A.3 The tight-binding Hamiltonian of graphene

To obtain the wavefunction for graphene, the corresponding Hamiltonian should be considered first. A general Hamiltonian for an electron is given by

$$H = \frac{\hat{p}^2}{2m} + V_{lattice}(\vec{x}) + V_{electrons}(\text{locations of all other electrons}). \tag{A.4}$$

The $V_{electrons}$ is the electron-electron interaction and $V_{lattice}$ is the potential the electrons feel from the lattice. For the tight binding approach only the kinetic energy term and the lattice potential are considered. The lattice potential can be divided into contributions of every unit-cell and this is split again into a contribution from both (identical) atoms in this cell:

$$\begin{aligned} V_{lattice}(\vec{x}) &= \sum_{\vec{R}\in G} \left[V_{atom}(\vec{x}-\vec{x}_1-\vec{R}) + V_{atom}(\vec{x}-\vec{x}_2-\vec{R}) \right] && \text{(A.5)} \\ & && \text{(A.6)} \end{aligned}$$

Now this is solved for $\vec{R} = \vec{0}$ and atom 1 in the unit-cell. The Hamiltonian can be written as

$$\begin{aligned} H &= H_0 + H_1 \\ H_0 &= \frac{\hat{p}^2}{2m} + V_{atom}(\vec{x}-\vec{x}_1) && \text{(A.7)} \\ H_1 &= V_{atom}(\vec{x}-\vec{x}_2) + \sum_{\vec{R}\in G\backslash\{\vec{0}\}} \left[V_{atom}(\vec{x}-\vec{x}_1-\vec{R}) + V_{atom}(\vec{x}-\vec{x}_2-\vec{R}) \right] \end{aligned}$$

The real atomic orbitals ϕ_1 and ϕ_2 are eigenstates of the Hamiltonian H_0 with energies ϵ_1 and ϵ_2. The unit-cell equivalent atomic orbital (equation A.3) is therefore also an eigenstate of H_0. For the whole lattice the solution is a linear combination, since the atomic orbitals are defined to be decoupled for H_0, so

$$\boxed{\Psi_{\vec{k}} = \sum_{\vec{R}\in G} e^{i\vec{k}\cdot\vec{R}} \phi(\vec{x}-\vec{R})} \tag{A.8}$$

where the weights are chosen in such a way that the wavefunction is also an eigenstate of the translation operator for a specific $\vec{k}$, where $\vec{k} = \hat{p}/\hbar$. This wavefunction is called the Wannier function.

The unperturbed energy is identical for each atom and it is convenient to set this energy to zero for this problem: $\epsilon_1 = \epsilon_2 = \epsilon = 0$. Returning to the case of $\vec{R} = \vec{0}$ and the first atom, the Schröddinger equation becomes

$$\begin{aligned} H\left|\phi_1\right\rangle &= \epsilon\left|\phi_1\right\rangle + H_1\left|\phi_1\right\rangle = 0 + \Delta U_1 \phi_1 && \text{(A.9)} \\ \Delta U_1 &= V_{atom}(\vec{x}-\vec{x}_2) + \sum_{\vec{R}\in G\backslash\{\vec{0}\}} \left[V_{atom}(\vec{x}-\vec{x}_1-\vec{R}) + V_{atom}(\vec{x}-\vec{x}_2-\vec{R}) \right] \end{aligned}$$

and the same can be done for the second atom.

$$\begin{aligned} H\left|\phi_2\right\rangle &= \epsilon\left|\phi_2\right\rangle + H_1\left|\phi_2\right\rangle = 0 + \Delta U_2\phi_2 \\ \Delta U_2 &= V_{atom}(\vec{x}-\vec{x}_1) + \sum_{\vec{R}\in G\setminus\{\vec{0}\}}\left[V_{atom}(\vec{x}-\vec{x}_1-\vec{R}) + V_{atom}(\vec{x}-\vec{x}_2-\vec{R})\right] \end{aligned} \tag{A.10}$$

For these equation only the potential is considered for which the Hamiltonian has not yet been solved, as explained above and visualized in figure A.3.

From the Schrödinger equation, it can be derived that

$$\begin{aligned} H\Psi_{\vec{k}} &= E(\vec{k})\Psi_{\vec{k}} \\ \langle\phi_j|H\left|\Psi_{\vec{k}}\right\rangle &= \langle\phi_j|E(\vec{k})\left|\Psi_{\vec{k}}\right\rangle \\ \langle\phi_j|\Delta U_j\left|\Psi_{\vec{k}}\right\rangle &= E\left\langle\phi_j|\left|\Psi_{\vec{k}}\right\rangle\right. \end{aligned} \tag{A.11}$$

were j can take the value 1 or 2. For both atoms, there is a contribution due to the orbital overlap. In principle there is an overlap for every orbital with every other orbital in the crystal. Because of tight-binding, only the overlap for nearest neighbors will be taken into account, reducing the collection G to the nearest neigbors G_{nn} (figure A.4).To get higher order solutions, more neighbours can be taken into account without changing the general method. For the first atom, the overlap matrix (sometimes called transition matrix) becomes

$$\begin{aligned} \langle\phi_1|\Psi_{\vec{k}}\rangle &= \langle\phi_1|\left[\sum_{\vec{R}\in G_{nn}} e^{i\vec{k}\cdot\vec{R}}\left(c_1\left|\phi_1\right\rangle + c_2\left|\phi_2\right\rangle\right)\right] \\ &= c_1\langle\phi_1|\phi_1\rangle + c_2\langle\phi_1|\phi_2\rangle + e^{-i\vec{k}\cdot\vec{a}_1}c_2\langle\phi_1|\phi_2\rangle + e^{-i\vec{k}\cdot\vec{a}_2}c_2\langle\phi_1|\phi_2\rangle \\ \langle\phi_1|\Psi_{\vec{k}}\rangle &= c_1 + c_2\langle\phi_1|\phi_2\rangle\left(1 + e^{-i\vec{k}\cdot\vec{a}_1} + e^{-i\vec{k}\cdot\vec{a}_2}\right) \\ \langle\phi_2|\Psi_{\vec{k}}\rangle &= c_2 + c_1\langle\phi_2|\phi_1\rangle\left(1 + e^{i\vec{k}\cdot\vec{a}_1} + e^{i\vec{k}\cdot\vec{a}_2}\right) \end{aligned} \tag{A.12}$$

where the overlap for the second atom is calculated equivalently.

The labels of the atoms should not matter for the physics and should therefore be interchangable

$$\langle\phi_1|\phi_2\rangle = \langle\phi_2|\phi_1\rangle = \gamma_0 \in \Re. \tag{A.13}$$

The left hand side of equation A.11 gives the overlap between the orbital of one atom and the potential of the other atoms and is called energy overlap matrix.

$$\begin{aligned} \langle\phi_1|\Delta U_1\left|\Psi_{\vec{k}}\right\rangle &= \langle\phi_1|\Delta U_1\left[\sum_{\vec{R}\in G_{nn}} e^{i\vec{k}\cdot\vec{R}}\left(c_1\left|\phi_1\right\rangle + c_2\left|\phi_2\right\rangle\right)\right] \\ &= c_1\langle\phi_1|\Delta U_1\left|\phi_1\right\rangle + c_2\langle\phi_1|\Delta U_1\left|\phi_2\right\rangle \\ &\quad + e^{-i\vec{k}\cdot\vec{a}_1}c_2\langle\phi_1|\Delta U_1\left|\phi_2\right\rangle + e^{-i\vec{k}\cdot\vec{a}_2}c_2\langle\phi_1|\Delta U_1\left|\phi_2\right\rangle \end{aligned} \tag{A.14}$$

The element $\langle\phi_1|\Delta U_1|\phi_1\rangle$ is very small if close to atom 1 because the potential is very small there (remember that ΔU_1 is the potential of everything *but* the atom 1). On the

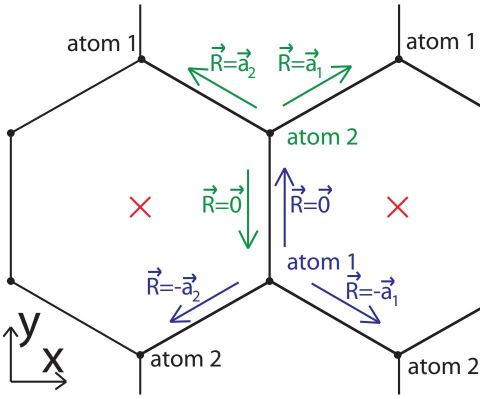

Figure A.4: *The graphene lattice with vectors to the nearest neighbors*

other hand this element is also very small when away from atom 1, since ϕ_1 is small far from the atom, see again figure A.3. With these considerations, it is assumed that $\langle\phi_1|\,\Delta U_1\,|\phi_1\rangle = 0$ and the previous equation is reduced to (the equation for $j = 2$ is found equivalently)

$$\begin{aligned}\langle\phi_1|\,\Delta U_1\,|\Psi_{\vec{k}}\rangle &= c_2\,\langle\phi_1|\,\Delta U_1\,|\phi_2\rangle\left[1 + e^{-i\vec{k}\cdot\vec{a_1}} + e^{-i\vec{k}\cdot\vec{a_2}}\right] \\ \langle\phi_2|\,\Delta U_2\,|\Psi_{\vec{k}}\rangle &= c_1\,\langle\phi_2|\,\Delta U_2\,|\phi_1\rangle\left[1 + e^{i\vec{k}\cdot\vec{a_1}} + e^{i\vec{k}\cdot\vec{a_2}}\right]\end{aligned} \tag{A.15}$$

The labels of the atoms should not matter for the physics

$$\langle\phi_1|\,\Delta U_1\,|\phi_2\rangle = \langle\phi_2|\,\Delta U_2\,|\phi_1\rangle = \gamma_1 \in \Re \tag{A.16}$$

Returning to the original Schröddinger equation A.11 where $\alpha(\vec{k}) = 1 + e^{-i\vec{k}\cdot\vec{a_1}} + e^{-i\vec{k}\cdot\vec{a_2}}$, the equation becomes:

$$\begin{aligned}E(\vec{k})\left[c_1 + c_2\gamma_0\alpha(\vec{k})\right] &= c_2\gamma_1\alpha(\vec{k}) \\ E(\vec{k})\left[c_2 + c_1\gamma_0\alpha^\dagger(\vec{k})\right] &= c_1\gamma_1\alpha^\dagger(\vec{k})\end{aligned} \tag{A.17}$$

or written as a matrix equation

$$\begin{bmatrix} E(\vec{k}) & \gamma_0\alpha(\vec{k})E(\vec{k}) - \gamma_1\alpha(\vec{k}) \\ \gamma_0\alpha^\dagger(\vec{k})E(\vec{k}) - \gamma_1\alpha^\dagger(\vec{k}) & E(\vec{k}) \end{bmatrix}\begin{bmatrix} c_1 \\ c_2 \end{bmatrix} = \begin{bmatrix} 0 \\ 0 \end{bmatrix} \tag{A.18}$$

This equation has a non-trivial solution when the determinant is zero:

$$\begin{aligned}E^2(\vec{k}) - \alpha(\vec{k})\alpha^\dagger(\vec{k})\left[(\gamma_0 E(\vec{k} - \gamma_1)(\gamma_0 E(\vec{k}) - \gamma_1\right] &= 0 \\ E^2(\vec{k}) = |\alpha(\vec{k})|^2\left[\gamma_0 E(\vec{k}) - \gamma_1\right]^2& \\ E(\vec{k}) = \pm|\alpha(\vec{k})|(\gamma_0 E(\vec{k}) - \gamma_1)&\end{aligned} \tag{A.19}$$

If there is no overlap between the orbitals of different atoms ($\gamma_0 = 0$) and no overlap between orbitals and neighboring potentials ($\gamma_1 = 0$), then the energy correction term $E(\vec{k})$ is zero, as expected.

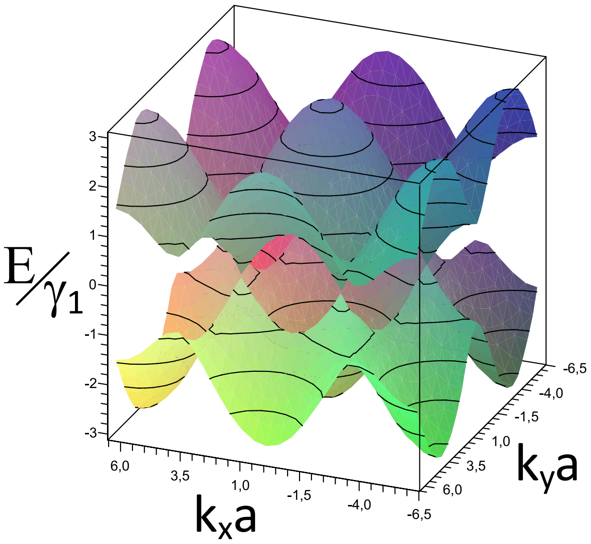

Figure A.5: *Energy as a function of momentum. The sign of equation A.22 determines the band to which the state belongs. The bottom band is called valance band or π-band and the top band is called the conduction-band or the π^*-band.* Note that for this plot a and γ_1 are set to 1.

Experimentally, it turns out that $\gamma_0 << \gamma_1$ and $\gamma_1 \sim 2.9eV$ (Charlier *et al.* (2007)) so the dispersion relation can be simplified even further to

$$\begin{aligned} E(\vec{k}) &= \pm\gamma_1|\alpha(\vec{k})| = \pm\gamma_1\sqrt{\alpha(\vec{k})\alpha^\dagger(\vec{k})} \\ &= \pm\gamma_1\left[3 + 2\cos(\vec{k}\cdot\vec{a_1}) + 2\cos(\vec{k}\cdot\vec{a_2})\right]^{\frac{1}{2}} \end{aligned} \tag{A.20}$$

and when using the values of the lattice vectors

$$\vec{k} = \begin{bmatrix} k_x \\ k_y \end{bmatrix}, \quad \vec{a_1} = a\begin{bmatrix} 1/2 \\ \sqrt{3}/2 \end{bmatrix}, \quad \vec{a_2} = a\begin{bmatrix} -1/2 \\ \sqrt{3}/2 \end{bmatrix}, \tag{A.21}$$

and rewriting some cosines, equation A.20 becomes

$$E(\vec{k}) = \pm\gamma_1\left[1 + 4\cos(\frac{a\ k_x}{2})\cos(\frac{\sqrt{3}a\ k_y}{2}) + 4\cos^2(\frac{a\ k_x}{2})\right]^{\frac{1}{2}} \tag{A.22}$$

Plotting above equation for both the positive and the negative sign results in figure A.5. For each value of $\vec{k}$ there are two states available due to spin. The unit-cell has two valence electrons and those will occupy the states with the lowest energy, which are the spin up and spin down position of the lowest energy band and this is the ground state. At zero temperature every electron occupies its ground state and since there are as many k points as atoms in the solid, the valence-band will be completely filled and the conduction-band will be completely empty. This means that the Fermi-energy of graphene is $E_f = 0$

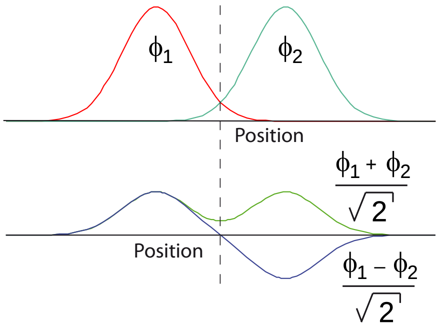

Figure A.6: *The symmetric and anti-symmetric states of the total lattice point equivalent atomic orbital. Because of its lower energy, the anti-symmetric is the bonding state where there is no electron in between the atoms.*

and since the bands touch at the Fermi level, no additional energy is needed to excite a electron from the top of the valence-band to the bottom of the conduction-band and this means that graphene behaves like a metal. The points where the bands touch are called the Dirac points.

A special k-point is $\vec{k} = \vec{0}$, where the energy is $E(\vec{0}) = \pm 3\gamma_1$. The matrix notation then simplifies to

$$3\gamma_1 \begin{bmatrix} \pm 1 & -1 \\ -1 & \pm 1 \end{bmatrix} \begin{bmatrix} c_1 \\ c_2 \end{bmatrix} = \begin{bmatrix} 0 \\ 0 \end{bmatrix} \sim 3\gamma_1 \begin{bmatrix} \pm 1 & -1 \\ 0 & 0 \end{bmatrix} \begin{bmatrix} c_1 \\ c_2 \end{bmatrix} = \begin{bmatrix} 0 \\ 0 \end{bmatrix} \tag{A.23}$$

and this means that $c_1 = c_2$ for a positive energy and $c_1 = -c_2$ for a negative energy, or using equation A.3 and normalize to get

$$\phi = \frac{\phi_1 \pm \phi_2}{\sqrt{2}} \tag{A.24}$$

The state with the plus sign is symmetric and has the highest energy and is the anti-bonding state. The minus sign indicates the anti-symmetric state which has the lowest energy and is the bonding state, see figure A.6.

A.4 Brillouin zone of graphene

The factor $e^{i\vec{k}\cdot\vec{R}}$ in equation A.8 is periodic, because for $\vec{k} = \vec{k}' + \vec{b}_i$ and $\vec{b}_i \cdot \vec{R} = 2\pi$ the points $\vec{k}$ and $\vec{k}'$ are equivalent since $e^{i\vec{k}\cdot\vec{R}} = e^{i\vec{k}'\cdot\vec{R}}e^{i2\pi} = e^{i\vec{k}'\cdot\vec{R}}$, with R still chosen from G. The vectors $\vec{b}_i$ are called the reciprocal lattice vectors, since they themselves form a lattice in k-space and have a reciprocal relationship with the conventional lattice vectors. The points where $e^{i\vec{k}\cdot\vec{R}} = 1$ are called the reciprocal lattice points. The vectors obey the following relation

$$\vec{b}_i \cdot \vec{a}_j = 2\pi\delta_{ij}, \tag{A.25}$$

since this is the required periodicity and the usual convention is used for the cross relations between lattice vectors and reciprocal lattice vectors (Ashcroft & Mermin (1976)). The

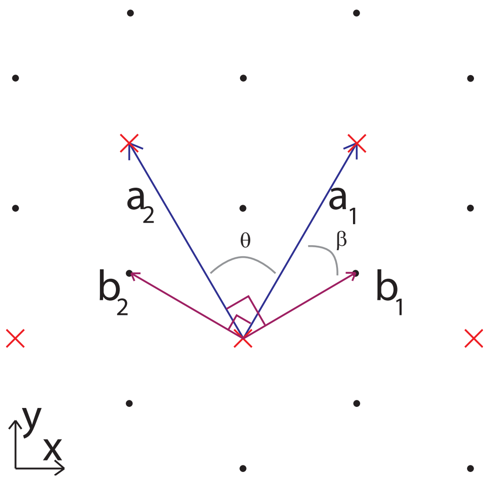

Figure A.7: *The lattice vectors for graphene ($\vec{a}_1$ and $\vec{a}_2$) and their reciprocal counterparts ($\vec{b}_1$ and $\vec{b}_2$).*

angle between the two lattice vectors θ is 60°, implying the angle between the lattice vectors and their reciprocal counterparts is $\beta = 30°$, see figure A.7. From these relations the size of the reciprocal lattice vector can be calculated as

$$\begin{aligned} \vec{a}_1 \cdot \vec{b}_1 &= |\vec{a}_1||\vec{b}_1|\cos\beta = \frac{\sqrt{3}a}{2}|\vec{b}_1| = 2\pi \\ |\vec{b}_1| &= |\vec{b}_2| = \frac{4\pi}{\sqrt{3}a}. \end{aligned} \tag{A.26}$$

With these reciprocal vectors the reciprocal lattice can be constructed (see figure A.8):

$$\vec{b}_1 = \frac{2\pi}{a}\begin{bmatrix} 1 \\ \frac{1}{3}\sqrt{3} \end{bmatrix}, \quad \vec{b}_2 = \frac{2\pi}{a}\begin{bmatrix} -1 \\ \frac{1}{3}\sqrt{3} \end{bmatrix}. \tag{A.27}$$

Note that this is a fundamentally different lattice from the real space lattice and its base is $\vec{k}$. All points on this lattice which are separated by an integer amount of lattice vectors are equivalent, as described above. To reduce the reciprocal lattice to points that are not equivalent to each other, the Brillouin zone is constructed. The Brillouin zone (BZ) is the Wigner-Seitz cell of the reciprocal lattice and is also shown in figure A.8. All the physics of the solid can be represented within this BZ, because each point outside the BZ is equivalent to one in the BZ.

The corners of the Brillouin zone are special. All corner points are equivalent to other corner points, since they are on the border of the BZ, but there are two inequivalent sets of corner points and these are called K and K'. The position of these points can be calculated from the lattice vectors (see figure A.9) and this is done for the first quadrant to get

$$\vec{K} = \begin{bmatrix} \frac{2\pi}{3a} \\ 0 \end{bmatrix}, \quad \vec{K'} = \begin{bmatrix} \frac{2\pi}{3a} \\ \frac{2\pi}{\sqrt{3}a} \end{bmatrix} \tag{A.28}$$

Note that both the K and K' points are the Dirac points for graphene, because equation A.20 gives zero for the corresponding energies.

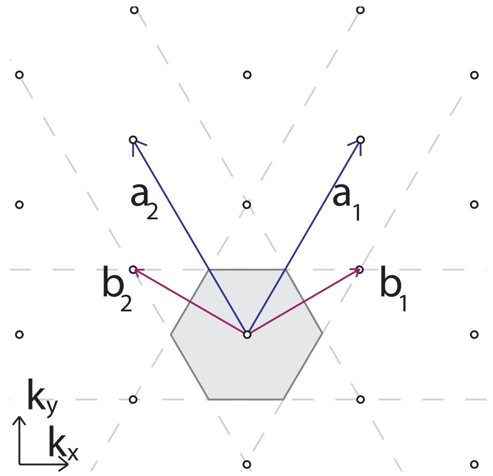

Figure A.8: *The reciprocal lattice for graphene, the hollow circles are the reciprocal lattice points. Note that although this looks similar to the real space lattice it is fundamentally different. The Brillouin zone is constructed as the area in gray by use of the half way lines of the neighboring lattice points.*

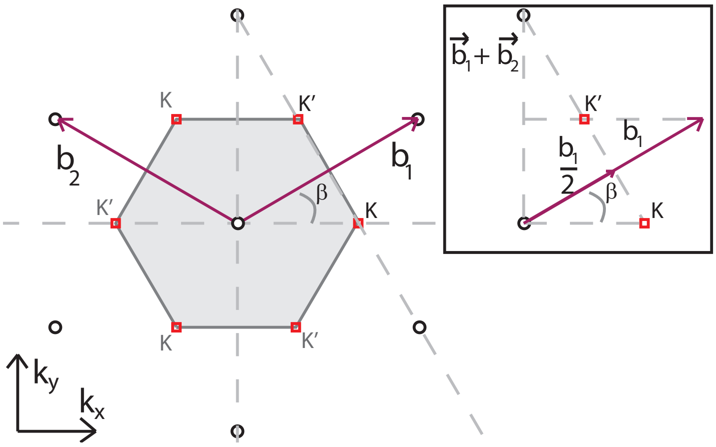

Figure A.9: *The K and K' points of the Brillouin zone, the inlet shows the relevant geometry to calculate the position of the K-points.*

A.5 Expansion around the K-points

At low energies, only the valence electrons close to the Fermi-level (the K-points) determine the electron-behavior of graphene. Therefore, it is more convenient to expand $E(\vec{k})$ around the $\vec{K}$ point. With $\vec{k} = \vec{K} + \vec{\kappa}$ expand

$$\begin{aligned} E(\vec{k}) &= E(\vec{K}+\vec{\kappa}) \\ &\approx E(\vec{K}) + \vec{\nabla}_{\vec{k}} E|_{\vec{K}} \cdot \vec{\kappa} + ... \\ & \quad 0 + \epsilon(\vec{\kappa}). \end{aligned} \tag{A.29}$$

This can be inserted in the matrix-equation A.18, where $\alpha(\vec{\kappa})$ is also expanded:

$$\begin{aligned} \alpha(\vec{k}) &= 1 + e^{-i\vec{k}\cdot\vec{a_1}} + e^{-i\vec{k}\cdot\vec{a_2}} \\ \alpha(\vec{K}+\vec{\kappa}) &= 1 + e^{-i\vec{K}\cdot\vec{a_1}} e^{-i\vec{\kappa}\cdot\vec{a_1}} + e^{-i\vec{K}\cdot\vec{a_2}} e^{-i\vec{\kappa}\cdot\vec{a_2}} \\ &= 1 + e^{-i\frac{2\pi}{3}} e^{-i\vec{\kappa}\cdot\vec{a_1}} + e^{i\frac{2\pi}{3}} e^{-i\vec{\kappa}\cdot\vec{a_2}}, \end{aligned} \tag{A.30}$$

and note that $\alpha(\vec{K}) = 0$. Continuing,

$$\begin{aligned} \alpha(\vec{K}+\vec{\kappa}) &= \alpha(\vec{K}) + \vec{\nabla}_{\vec{k}} \alpha|_{\vec{K}} \cdot \vec{\kappa} + ... \\ \frac{\delta\alpha}{\delta k_x}|_{\vec{K}} &= -\frac{\sqrt{3}a}{2} \\ \frac{\delta\alpha}{\delta k_y}|_{\vec{K}} &= -i\frac{\sqrt{3}a}{2} \\ \alpha(\vec{K}+\vec{\kappa}) &\approx -\frac{\sqrt{3}a}{2}(\kappa_x + i\kappa_y) \end{aligned} \tag{A.31}$$

Transforming matrix equation A.18

$$\begin{bmatrix} \epsilon(\vec{\kappa}) & \frac{\sqrt{3}}{2}\gamma_1 a(\kappa_x + i\kappa_y) \\ \frac{\sqrt{3}}{2}\gamma_1 a(\kappa_x - i\kappa_y) & \epsilon(\vec{\kappa}) \end{bmatrix} \begin{bmatrix} c_1 \\ c_2 \end{bmatrix} = \begin{bmatrix} 0 \\ 0 \end{bmatrix} \tag{A.32}$$

and one obtains the solution in the same way:

$$\epsilon(\vec{k}) = \pm(\frac{\sqrt{3}}{2}\gamma_1 a)|\vec{\kappa}|. \tag{A.33}$$

The speed of a wavepacket is given by

$$\begin{aligned} v_f &= |\vec{v}| = \hbar^{-1}|\frac{d\epsilon}{d\vec{k}}| = \frac{\sqrt{3}\gamma_1 a}{2\hbar} \\ &= 10^6 m/s \end{aligned} \tag{A.34}$$

and this can be used to rewrite

$$\boxed{\epsilon(\vec{k}) = \pm\hbar v_f |\vec{\kappa}|} \tag{A.35}$$

and solve the matrix equation for c_1 and c_2

$$\begin{aligned} & \frac{\sqrt{3}a\gamma_1}{2}\begin{bmatrix} \pm|\vec{\kappa}| & (\kappa_x+i\kappa_y) \\ (\kappa_x-i\kappa_y) & \pm|\vec{\kappa}| \end{bmatrix}\begin{bmatrix} c_1 \\ c_2 \end{bmatrix}=\begin{bmatrix} 0 \\ 0 \end{bmatrix} \\ \sim\; & \frac{\sqrt{3}a\gamma_1}{2}\begin{bmatrix} \pm|\vec{\kappa}| & (\kappa_x+i\kappa_y) \\ 0 & 0 \end{bmatrix}\begin{bmatrix} c_1 \\ c_2 \end{bmatrix}=\begin{bmatrix} 0 \\ 0 \end{bmatrix} \end{aligned} \tag{A.36}$$

and this means $c_1 = \pm\frac{(\kappa_x+i\kappa_y)}{|\vec{\kappa}|}c_2$. In general, a complex number z can be represented as $|z|e^{i\arg z}$, so $c_1 = \pm e^{i\arg(\kappa_x+i\kappa_y)}c_2 = \pm e^{i\beta}c_2$, if $\beta = \arg(\kappa_x+i\kappa_y)$. Choosing $c_2 = e^{i\beta/2}$ and normalizing to obtain

$$\vec{b} = \frac{1}{\sqrt{2}}\begin{bmatrix} \pm e^{i\beta/2} \\ e^{-i\beta/2} \end{bmatrix}, \tag{A.37}$$

or applied to equation A.3 (with β depending on $\vec{k}$)

$$\phi_{\vec{k}}^{\pm} = \frac{1}{\sqrt{2}}\left[\pm e^{i\beta/2}\phi_1 + e^{-i\beta/2}\phi_2.\right] \tag{A.38}$$

To calculate the probability to go from one state to another, the overlap is calculated between different $\phi_k^{\pm}$, where the plus sign is for the positive energy and the minus sign for the states with a negative energy, using $p,q=\pm$,

$$\begin{aligned} \langle\phi_{k1}^{p}|\phi_{k2}^{q}\rangle &= pq\frac{1}{2}e^{-i\beta_1/2}e^{i\beta_2/2}\langle\phi_1|\phi_1\rangle + \frac{1}{2}e^{i\beta_2/2}e^{-i\beta_1/2}\langle\phi_2|\phi_2\rangle \\ &\quad + p\frac{1}{2}e^{-i\beta_1/2}e^{-i\beta_2/2}\langle\phi_{k1}|\phi_{k2}\rangle + q\frac{1}{2}e^{i\beta_1/2}e^{i\beta_2/2}\langle\phi_{k2}|\phi_{k1}\rangle \\ &= \frac{1}{2}e^{i\beta_1/2}e^{-i\beta_2/2} + pq\frac{1}{2}e^{-i\beta_2/2}e^{i\beta_1/2} \\ &\quad + \gamma_0\left[p\frac{1}{2}e^{-i\beta_1/2}e^{-i\beta_2/2} + q\frac{1}{2}e^{i\beta_1/2}e^{i\beta_2/2}\right] \end{aligned} \tag{A.39}$$

with this equation and $\gamma_0 << 1$, selection rules for graphene are obtained

$$\begin{aligned} |\langle\phi_k^+|\phi_k^+\rangle|^2 &= 1, \\ |\langle\phi_k^-|\phi_k^-\rangle|^2 &= 1, \\ |\langle\phi_k^+|\phi_k^-\rangle|^2 &= 0, \\ |\langle\phi_k^+|\phi_{-k}^+\rangle|^2 &= 1, \\ |\langle\phi_k^+|\phi_{-k}^+\rangle|^2 &= 0, \\ |\langle\phi_k^-|\phi_{-k}^-\rangle|^2 &= 0. \end{aligned} \tag{A.40}$$

This concludes the appendix about graphene.

Appendix B

Bandstructure of carbon nanotubes

This appendix will derive the bandstructure for both armchair and zigzag CNTs from the full graphene bandstructure. This section is meant to give a somewhat quantitative understanding of the mechanisms involved in the formation of the bandstructure. As a starting point, a wrapping vector of (N,N) is used for armchair CNTs and (N,0) for zigzag tubes (see 2.1.2 of main text and figure B.1).

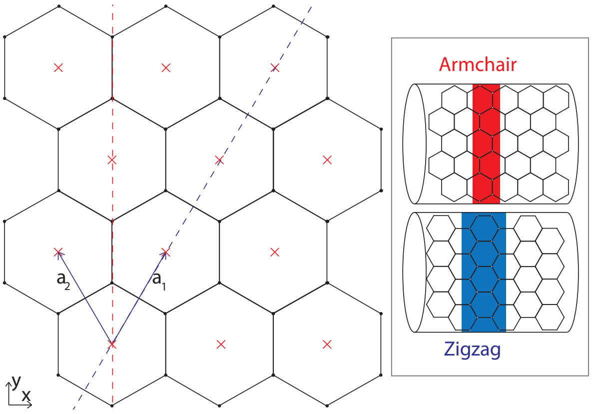

Figure B.1: *The graphene lattice with the wrapping directions indicated. If the sheet is rolled over the blue line, an armchair-CNT is created, and the red line corresponds to a zigzag-CNT, see the inset. Everything rolled over a line in between these lines is called a chiral-CNT. The inset shows the orientations on the carbon nanotubes. The colored bands denote the 1-D unit-cell.*

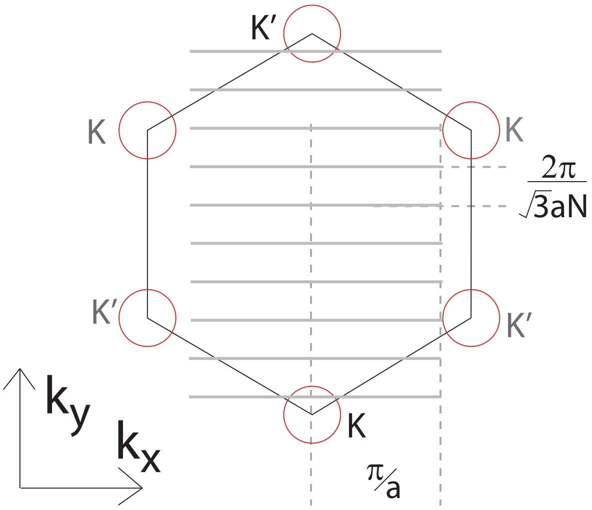

Figure B.2: *The Brillouin zone of graphene with the possible modes indicated as horizontal lines. The size of the horizontal lines indicate the size of the 1-D Brillouin Zone.*

B.1 Armchair-CNT

The CNT is periodic over the wrapping vector. This means that $e^{i\vec{k}\cdot(\vec{R}+\vec{w})} = e^{i\vec{k}\cdot\vec{R}}$ and $\vec{k}\cdot\vec{w_a} = 2\pi m$ where m has an integer value. This can be expressed in the $k_x k_y$-basis:

$$\begin{aligned}
\vec{w_a} &= N(\vec{a_1}+\vec{a_2}) = N\left(a\begin{bmatrix}1/2\\ \sqrt{3}/2\end{bmatrix} + a\begin{bmatrix}-1/2\\ \sqrt{3}/2\end{bmatrix}\right) = Na\begin{bmatrix}0\\ \sqrt{3}\end{bmatrix}\\
\vec{k}\cdot\vec{w_a} &= k_y N a\sqrt{3} = 2\pi m\\
k_y &= \frac{2\pi}{N\sqrt{3}a}m \qquad \text{(B.1)}
\end{aligned}$$

The maximum $|k_y|$ in the Brillouin Zone of graphene is $\frac{2\pi}{\sqrt{3}a}$, so for the value of k_y to be in the BZ, it must hold that $|\frac{m}{N}|$ or $-N \leq m \leq N$. For each value of k_x there are $2N$ different k_y values possible. The CNT can thus be viewed as a 1-D structure where different modes can exist. Below, it will be shown that the difference in energy between the modes is so big that under normal conditions (e.g. thermal energies) the electrons stay in the same mode. This is why a CNT is called a pseudo one dimensional structure.

Looking along the direction of the tube a repeating pattern emerges: the 1-D unit-cell. The atoms in the colored region of the inset of figure B.1 is repeated every $c_a = |\vec{a_1} - \vec{a_2}| = a$, where c_a is the 1-D lattice constant. The number of atoms in the 1-D unit-cell is 4N, because it contains 2 graphene unit-cells for each of the N honeycombs. The 1-D reciprocal lattice constant is given by $d_a = \frac{2\pi}{a}$, so the 1-D Brillouin Zone has size $\pm\frac{\pi}{a}$. These results can be summarized in the Brillouin zone of graphene, as is done in figure B.2.

Using the values for k_y in equation A.22 to get

$$E_m(\vec{k}) = \pm\gamma_1\left[1 + 4\cos\left(\frac{a\,k_x}{2}\right)\cos\left(\frac{\pi}{N}m\right) + 4\cos^2\left(\frac{a\,k_x}{2}\right)\right]^{\frac{1}{2}} \qquad \text{(B.2)}$$

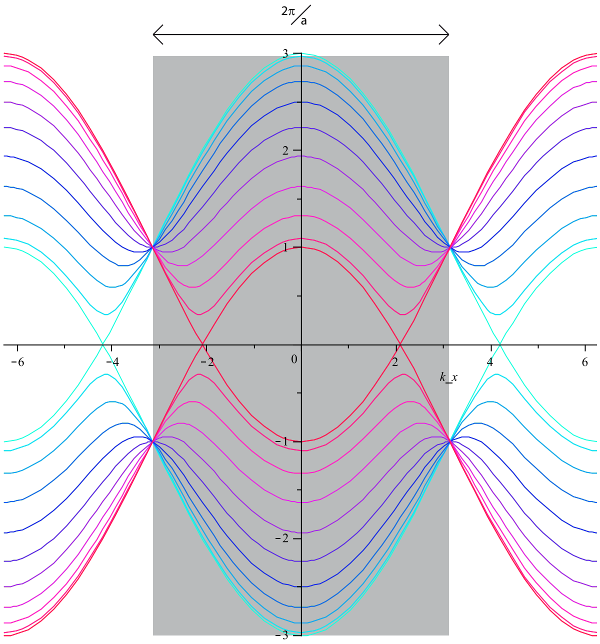

Figure B.3: *The armchair dispersion relation from equation B.2 plotted for* $N = 10$*,* $a = 1$*,* $\gamma_1 = 1$ *and* $-10 \leq m \leq 10$*. The different lines have a different* m*. Red denotes* $m = \pm 10$ *and the light-blue* $m = 0$*, the rest of the lines have values in between. The grey area is the 1-D Brillouin Zone*

and in figure B.3 this is plotted for N=10 and $-10 \leq m \leq 10$. From this figure and the equation above it can be seen that the states are degenerate, because the sign of m does not matter for the energy. The states $m = \pm 0$ are not separate states, and the state $m = -N$ is mapped on $m = N$ (see figure B.2) so these are also the same. The total states available for the energy are therefore 2N for each band and this is multiplied by two for spin to get the total available electron states. The 1-D unit-cell has 4N valence electrons and those fit exactly in the valence-band. The CNT has a Fermi energy $E_f = 0$ too. For this armchair configuration, the bands touch and a metallic behavior emerges.

B.2 Zigzag-CNT

For the zigzag-CNT the situation is rotated 30°. In figure B.1 the blue area in the inset indicates the 1-D unit-cell. The lattice constant is $c_z = |\vec{a_1} + \vec{a_2}| = \sqrt{3}a$ and this means the 1-D reciprocal lattice constant is given by $d_z = \frac{2\pi}{\sqrt{3}a}$, and the 1-D Brillouin Zone has size $\pm\frac{\pi}{\sqrt{3}a}$. Again, the periodicity across the cylinder is applied to get

$$\begin{aligned} \vec{k} \cdot \vec{w_z} &= 2\pi m \\ &= k_x N a/2 + k_y N a\sqrt{3}/2 = 2\pi m \qquad \text{(B.3)} \\ \frac{k_x}{\sqrt{3}} + k_y &= \frac{4\pi m}{\sqrt{3}aN} \end{aligned}$$

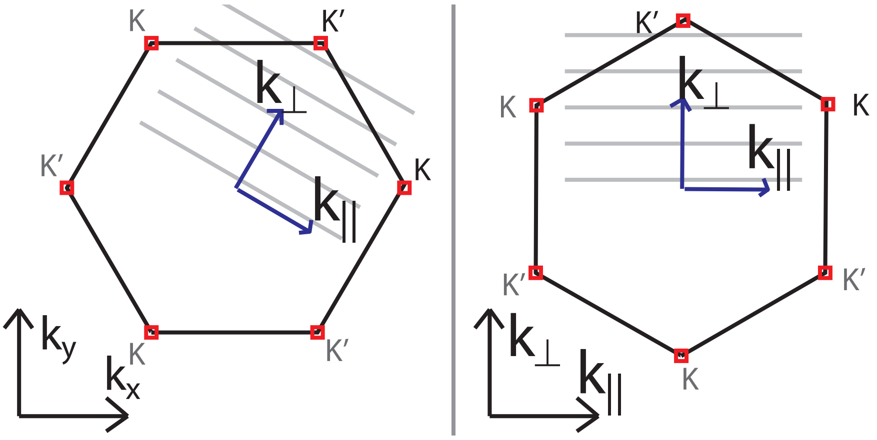

Figure B.4: *The Brillouin Zone of graphene with to the left the modes of a zigzag CNT with the vector which is quantized and its perpendicular counterpart. To the right the basis is rotated over* 30°.

and this means that the modes are not horizontal in the graphene Brillouin Zone anymore. For a general approach, the Brillouin Zone will be rotated to show the relevant modes more clearly. The (normalized) vector that is quantized is given from the above equation

$$\vec{k_\perp} = \begin{bmatrix} 1/2 \\ \sqrt{3}/2 \end{bmatrix}, \quad \vec{k_\parallel} = \begin{bmatrix} \sqrt{3}/2 \\ -1/2 \end{bmatrix}, \tag{B.4}$$

where $\vec{k_\parallel}$ is taken to be the vector perpendicular to $\vec{k_\perp}$, see also figure B.4. These vectors where already introduced in figure 2.3(b).

A basis rotation is executed to go from the $\vec{k_x}$, $\vec{k_y}$ to the $\vec{k_\parallel}$, $\vec{k_\perp}$ basis (the z-basis). For this the unit vectors are rotated:

$$\begin{aligned} \vec{k_x^z} &= (\vec{k_x} \cdot \vec{k_\parallel})\vec{k_\parallel} + (\vec{k_x} \cdot \vec{k_\perp})\vec{k_\perp} = \begin{bmatrix} \sqrt{3}/2 \\ 1/2 \end{bmatrix}_z, \\ \vec{k_y^z} &= (\vec{k_y} \cdot \vec{k_\parallel})\vec{k_\parallel} + (\vec{k_y} \cdot \vec{k_\perp})\vec{k_\perp} = \begin{bmatrix} -1/2 \\ \sqrt{3}/2 \end{bmatrix}_z \\ \mathbf{M_z} &= \begin{bmatrix} \vec{k_x^z} & \vec{k_y^z} \end{bmatrix} = \begin{bmatrix} \sqrt{3}/2 & -1/2 \\ 1/2 & \sqrt{3}/2 \end{bmatrix} \end{aligned} \tag{B.5}$$

where $\mathbf{M_z}$ is the transformation matrix. Using this transformation matrix to transform the wrapping vector, the lattice-vectors and K' to

$$\begin{aligned}
\vec{w}_z^{z} &= \mathbf{M_z}\vec{w}_z = \begin{bmatrix} 0 \\ Na \end{bmatrix}_z \\
\vec{a}_1^{z} &= \mathbf{M_z}\vec{a}_1 = \begin{bmatrix} 0 \\ 1 \end{bmatrix}_z \\
\vec{a}_2^{z} &= \mathbf{M_z}\vec{a}_2 = \begin{bmatrix} -\sqrt{3} \\ -1/2 \end{bmatrix}_z \\
\vec{K}'^{z} &= \mathbf{M_z}\vec{K}' = \begin{bmatrix} 4\pi/3 \\ 0 \end{bmatrix}_z .
\end{aligned} \tag{B.6}$$

The $\vec{K}'^{z}$ shows that the K point is on the $k_\perp$-axis, as it should be. From the rotated wrapping vector we get the quantization from $\vec{w}_z^{z} \cdot \vec{k}^{z} = 2\pi m$ which gives $k_\perp = \frac{2\pi}{a}\frac{m}{N}$. One of the modes crosses the K point if $k_\perp = \frac{4\pi}{3a}$ or $\frac{m}{N} = \frac{2}{3}$. Only if a mode crosses the K point, the bands touch. The rotated lattice-vectors can be used in equation A.20 to get a new dispersion relation, which is plotted in figure B.5. This figure nicely shows the N-dependence

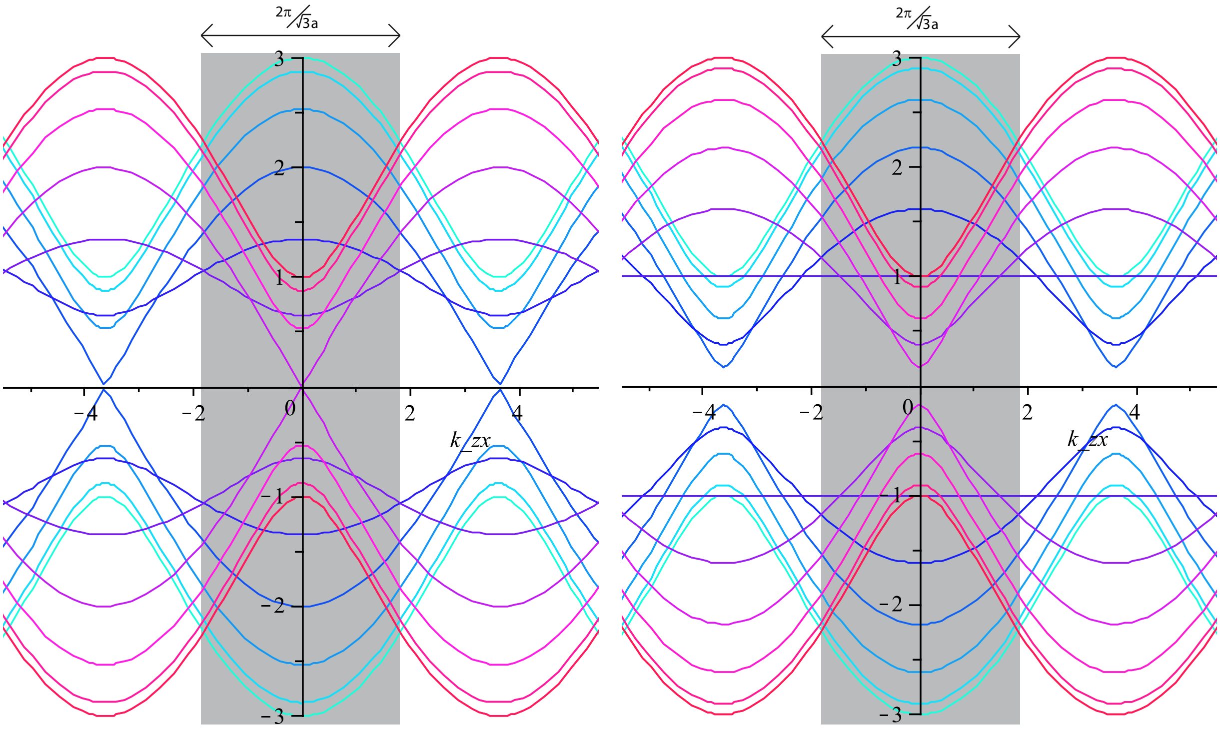

Figure B.5: *Energy-dispersion for the different modes and N=9 (left) and N=10 (right). Red denotes $m = \pm 10$ and light-blue $m = 0$. The grey area indicates the 1-D Brillouin Zone.*

of the electronic behavior of the zigzag-CNT. For N=9, the relation between m and N (as explained above) is such that a mode crosses the K' point and the bands touch. For N=10 this is not the case and all the modes 'miss' the K'-point and a gap emerges between the valence and conduction-band: the band-gap, resulting in semi-conductor behavior. The maximum bandgap scales with the distance between the modes (since that is the maximum distance a mode can be away from the K' point). This distance is $\frac{2\pi}{aN}$ and scales with $1/N$. N scales with circumference of the tube and therefore with the diameter, concluding that the maximum bandgap is inversely proportional to the diameter.

This discussion can easily be expanded to include a chiral-CNT. The transformation matrix should be determined and the rest of the calculation will be analogous. This will not be done here, because no new physics will appear. Note that the rotated basis always has a base vector perpendicular to the modes and one that runs parallel to the modes. This is why usually the modes are denoted as $k_\perp$ in the base of the zig-zag CNT) and $k_\parallel$.

Appendix C

Timing in DC measurements

Timing is an important factor when doing sequential DC measurements. Errors in the timing will create noise in the measurements. Two mechanisms that cause this noise will be discussed in this appendix.

The first mechanism is capacitative coupling. All wires going to the device have a capacitance between them as shown in figure C.1(a). In the setup used for this experimental work, the wires are going to the sample in a bundle, so a relatively large capacitance is present. When the voltage on the gate is changed, this will cause a change in current in a nearby measurement wire by

$$\Delta I_{meas} = \frac{dQ}{dt} = C\frac{dV_{gate}}{dt}. \tag{C.1}$$

In other words, the measured current is offset by an amount that depends on the speed of the change in gate voltage (sweep rate). This change in voltage is dependent on the step in voltage in the gate and the time Δt it takes to do this step. As long as the total rate dV_{gate}/dt is constant, this offset is constant and can be corrected for. If this Δt changes, the offset in the measurement also changes, coupling noise in timing to noise in current.

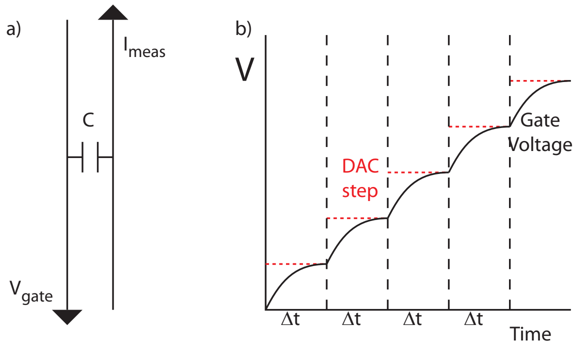

Figure C.1: *Mechanisms that introduce noise when timing errors occur. (a) Capacitative coupling. (b) Offset in measurement average. The red line is the digital step the DAC takes, the black line is the actual voltage the DAC puts on the gate.*

The second mechanism has to do with the finite rise time of the Digital-to-Analog converters (DACs), as shown in figure C.1(b). If a signal is given that the DAC should be swept to a certain voltage V, the output rises in a certain time. The measurement takes an average over a time Δt, and if consecutive measurements are taken, the timing has to be the same for the average step to be the same. If not, then the measurement is taken at a different stage during the rise time and the gate voltage is offset an unknown amount. This gate voltage offset translates in a change in measurement current, again coupling the noise in timing with noise in the measurement.

Figure C.2 shows that the effects of timing can be very significant in the type of measurements done in this thesis. It is therefore very important to pay attention to a stable constant timing.

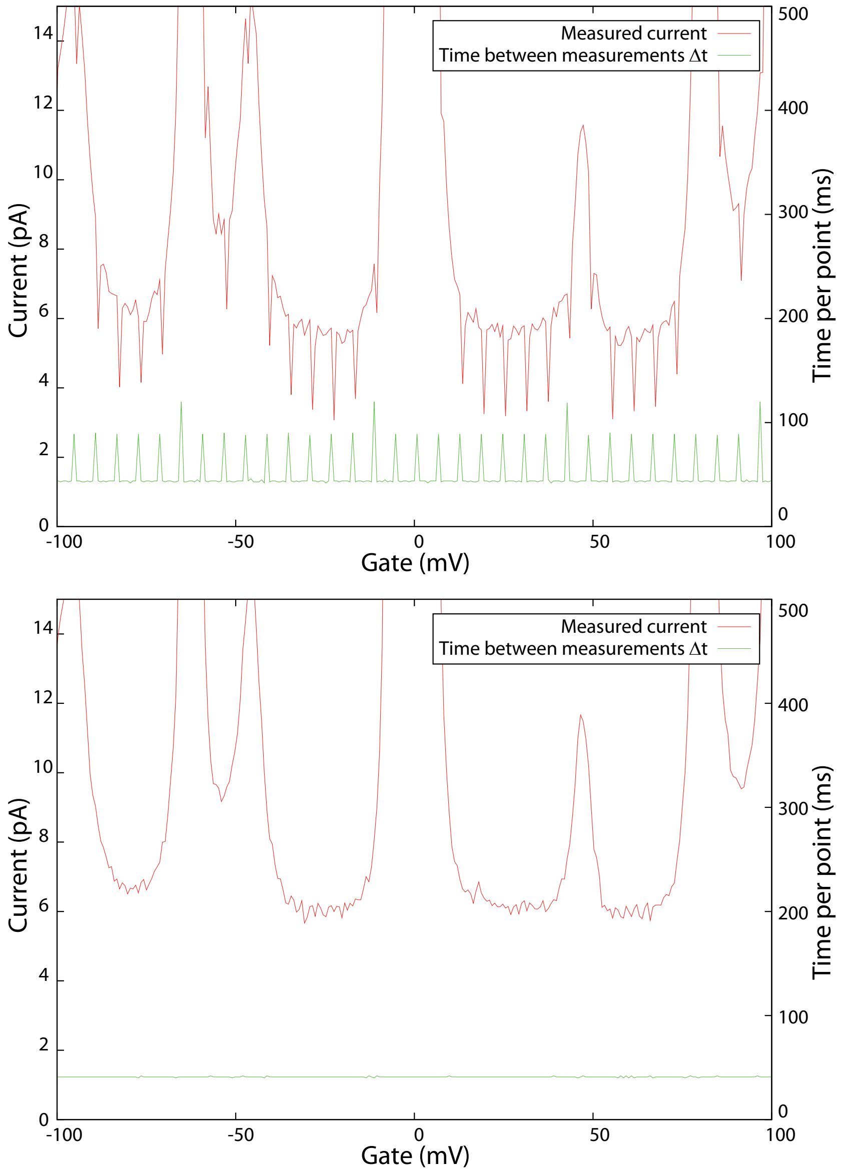

Figure C.2: *Two measurements that show the influence of timing. The gate is swept and the resulting current is measured (red). In green, the time between the steps during the sweep is shown. In the top plot, the timing is not constant due to a setting in the voltage meter. This causes peaks in the current measurement that disappear when the problem with the timing is solved in the bottom plot.*

Appendix D

Additional measurement data

In this appendix additional measurement data will be shown that supports the data in the main text.

For the three devices of the main text, a bandgap is obtained.In order to determine this bandgap, the distance in gate-space between the holes and electrons is corrected with the α-factor to get the addition energy between the electrons and holes E^0_{add}. This number is subtracted with the charging energy for this transition to get the bandgap of the device. The addition energy of the first electron E^e_{add} equals the charging energy for a spin degenerate system, just like the addition energy for the first hole E^h_{add}, making the bandgap $E_{gap} = E^0_{add} - (E^e_{add} + E^e_{add})/2$, see figure D.1.

D.1 Device D1

Coulomb diamonds for device D1 are shown in figure D.2. Many excited state lines are visible in the first few diamonds, but these are not excited states of the dot. Changing the gate voltages moves the lines with respect to the sides of the Coulomb diamond, indicating that these are not electronic states of the QD itself. These states can be states in the leads or vibrational excited states, for example.

The first four electrons transitions have clear diamond edges which can be extracted.

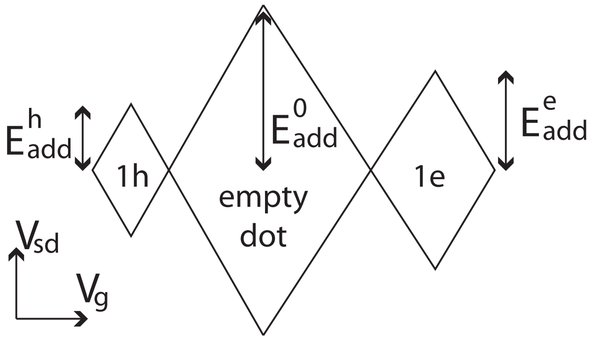

Figure D.1: *Schematic Coulomb diamond with the addition energies.*

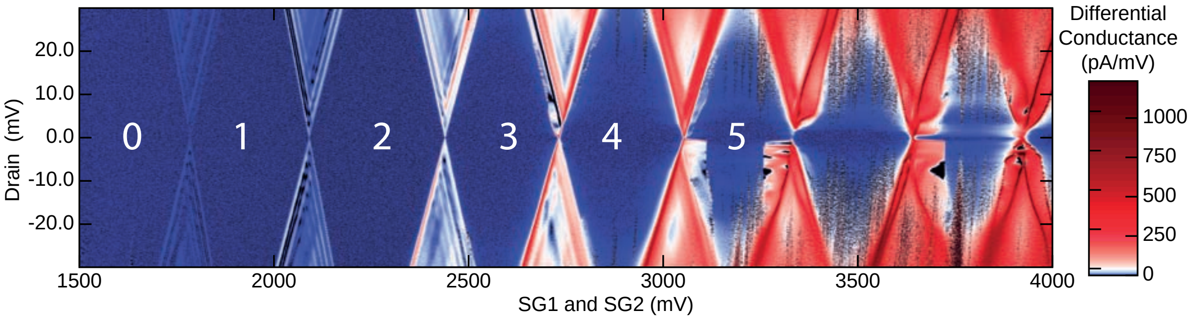

Figure D.2: *Coulomb diamonds for D1 with electron numbers indicated in white.*

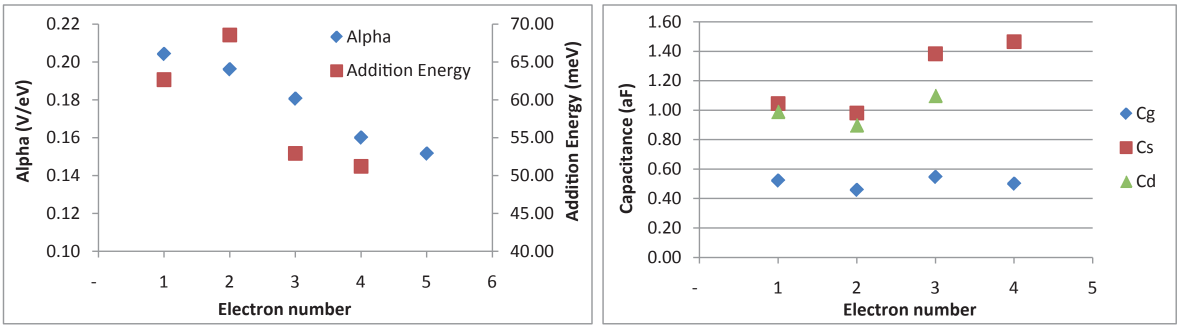

Figure D.3: *Values for alpha and addition energy of D1 for the first electrons (left), and capacitance to the gate (Cg), source (Cs) and drain (Cd) for the same electrons (right).*

This gives the slopes γ and β and are used to calculate the α-factor. From these factors the capacitance to the gates are calculated and together with the distance between the transition at zero bias the addition energy is calculated, see figure D.3. In this case, both the splitgates are swept together and can be seen as one gate.

For more than four electrons, non-linear mechanics starts to destroy the Coulomb diamond. The almost vertical features in the Coulomb-blockade for more than four electrons remain unidentified, but are speculated to come from a second tube. Note that for these electrons, co-tunneling lines become visible.

D.2 Device D2

Figure D.4 gives the temperature dependence during the cooldown (left) and at low temperatures (right) for device D2. The left of figure D.4 shows that the device goes from a smeared out transistor curve to Coulomb peaks. To the right, the temperature is decreased further and resonant tunneling causes higher and more narrow peaks.

Figure D.5 shows a Coulomb diamond measurement for device D2. The ideal behavior at low bias disappears at higher bias. This device has very small barriers so for more than three electrons, mechanical vibrations destroys the Coulomb diamonds. Also, some cotunneling is visible in the gaps. All measurements presented in this thesis were done at the lowest possible bias to avoid the mechanics, but the α-factor has to be determined

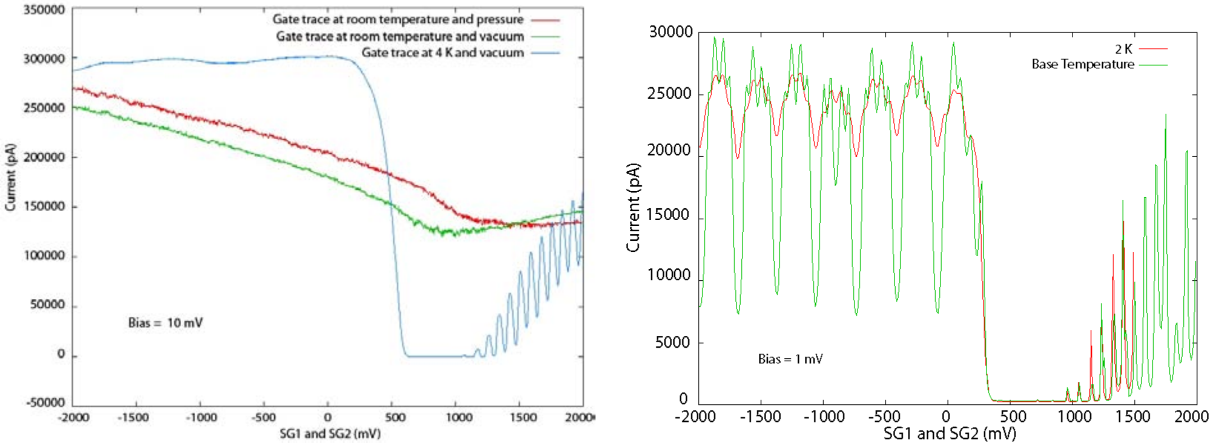

Figure D.4: *(left) Gate traces of device D2 at different stages of the cool down process. (right) Gate traces of device D2 showing the temperature dependence expected from a quantum dot.*

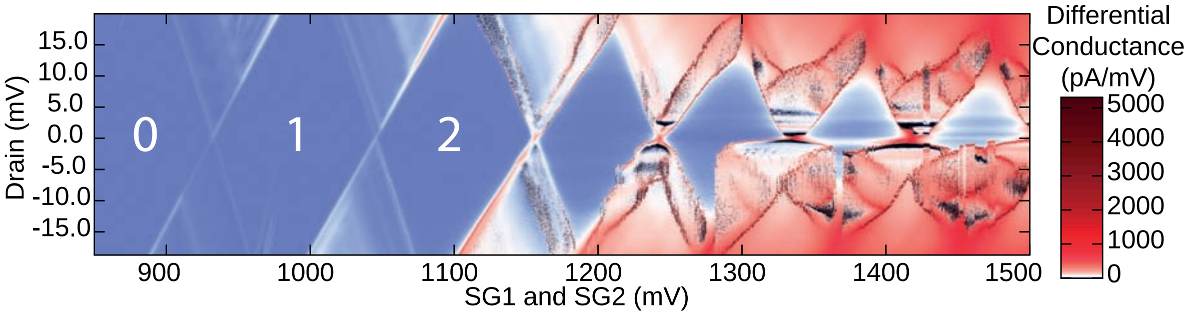

Figure D.5: *Coulomb diamonds for D2 with electron numbers indicated in white.*

from the Coulomb diamonds edges. Fortunately, the edges of the diamonds can still be estimated, in spite of the mechanics.

Note that in figure D.5, the addition energy already decreases by a factor of 2 between the first and 6th electron, as does the α-factor (the diamond edges are less steep). Figure D.6 gives the α-factor, addition energy, and capacitances as a function of electron number, as obtained from Coulomb diamonds like figure D.5. For the first 12 electrons a drastic decrease in α-factor is observed. From the values of the capacitance, it can be concluded that the dot becomes much broader with electron number since the capacitance to the source and drain becomes higher (see figure 3.2(b)).

D.3 Holes in device D2

Device D2 can also be tuned to the hole regime. Figure D.7 shows a very regular Coulomb peak pattern where the conductance is much higher than for the electrons. The workfunction difference between tube and contact metal creates a barrier between the p-doped leads and the nanotube if the quantum dot is n-doped (has electrons). Now, the tube is

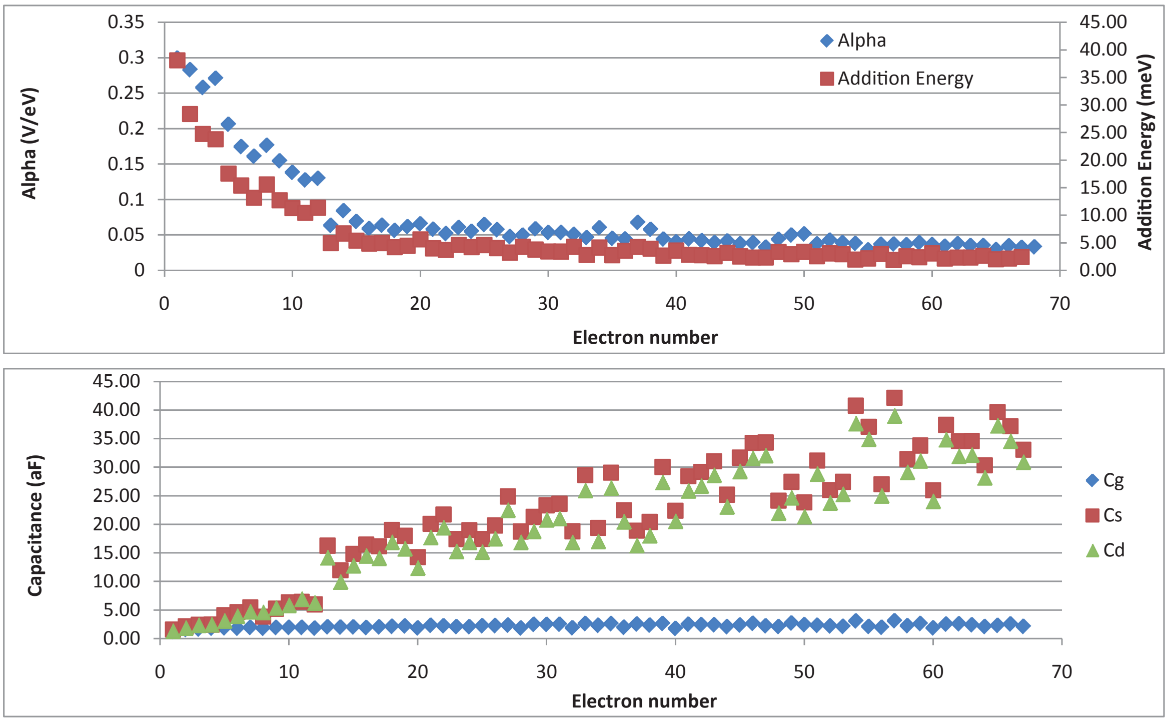

Figure D.6: *Values for alpha and addition energy of D2 (top), and capacitance to the gate (Cg), source (Cs) and drain (Cd) (bottom). The values for Cs and Cd from the 12th electron on are with a big error due to the mechanics breaking the Coulomb diamonds. The error is estimated to be in the order of the spread which is about 30%.*

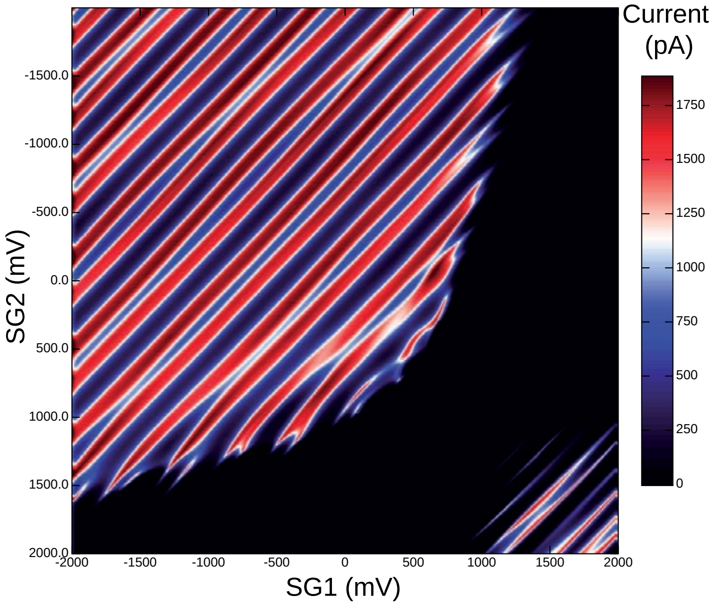

Figure D.7: *SGSG-plot of device D2 for the hole-regime.*

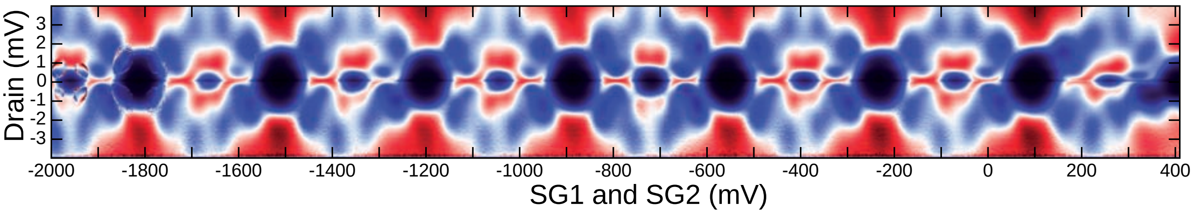

Figure D.8: *Coulomb diamonds for a the hole regime of device D2.*

also p-doped so the Schottky barrier is gone. For these type of devices, something else causes the barriers to be still closed enough to distinguish between the different Coulomb peaks. Figure D.8 shows the Coulomb diamonds of these holes. From shell to shell the diamonds do not change significantly. This means that the α-factor and the capacitances can be assumed constant for this regime:

	value
α-factor	0.025
C_g	2 aF
C_s	40 aF
C_d	36 aF

Note that these values of the highest electron numbers in D.6 are close to those of the holes. This must mean that the QD for holes is of the same size as that for the many electrons regime.

To explain this, the potential in the tube has to be discussed. The holes do not have a Schottky barrier, but still a barrier exists to the metals, as is shown in figure D.9(a). The green barrier is a some barrier to the metal. Its exact position is not know and could also be more above the metal. The level spacing is small because the QD size is defined by the metal-CNT barriers and the QD has at least the length of the CNT. If the gate voltage is increased, this p-type QD empties slowly, but before the single hole regime is reached, the bandgap crosses the Fermi-level. If the voltage is increased further, the potential will allow a small n-type QD (figure D.9(b)). Now the QD size can be very small, making the level spacing big and the n-type QD is in the single electron regime. Note that the electron have to tunnel trough a large barrier (the bandgap) when going trough the dot. Increasing the voltage even more will tune the n-type dot to the many electron regime (figure D.9(c)). Here, the size of the QD is again much bigger and similar to the holes. The barrier is much smaller because the bandgap gets ‘squeezed’ against the metal.

D.4 Device D3

Figure D.10 shows a Coulomb diamond measurement for device D3. No clear excited states are visible in the Coulomb diamonds and mechanics breaks down the diamond structure for more than 2 electrons. Figure D.11 gives another measurement of the same device for larger bias but with a smaller gate voltage range. Only the first two electrons are used in the thesis and the α-factor is estimated from the slope of the zoomed diamonds to be $\sim 0.25\ meV/mV$, see figure D.12.

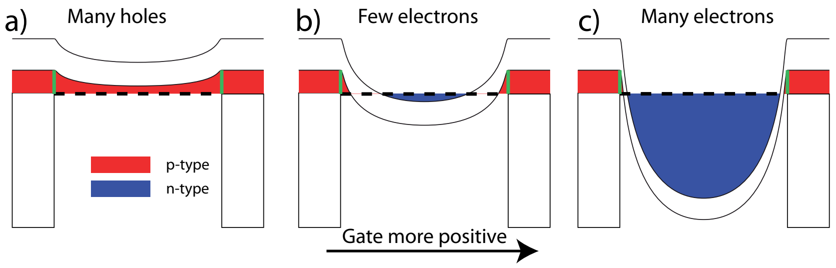

Figure D.9: *The CNT potential for different gate voltages. In green a barrier is shown from the CNT to the metal. The dotted line is the Fermi-level.*

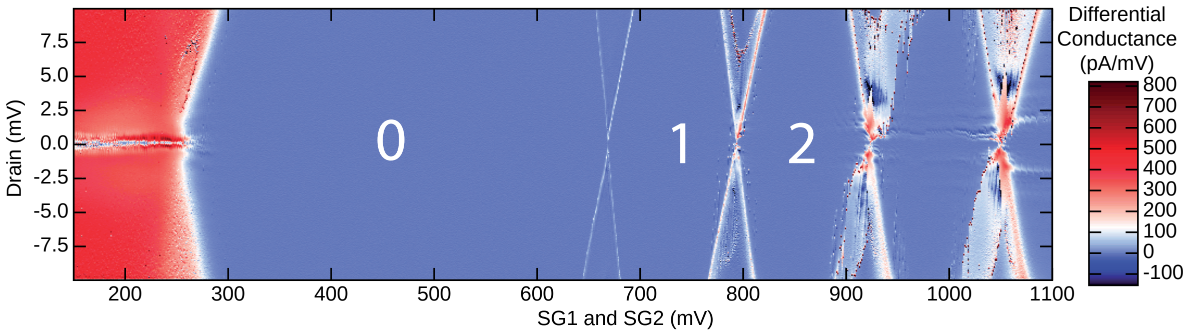

Figure D.10: *Coulomb diamonds for D3 with electron numbers indicated in white.*

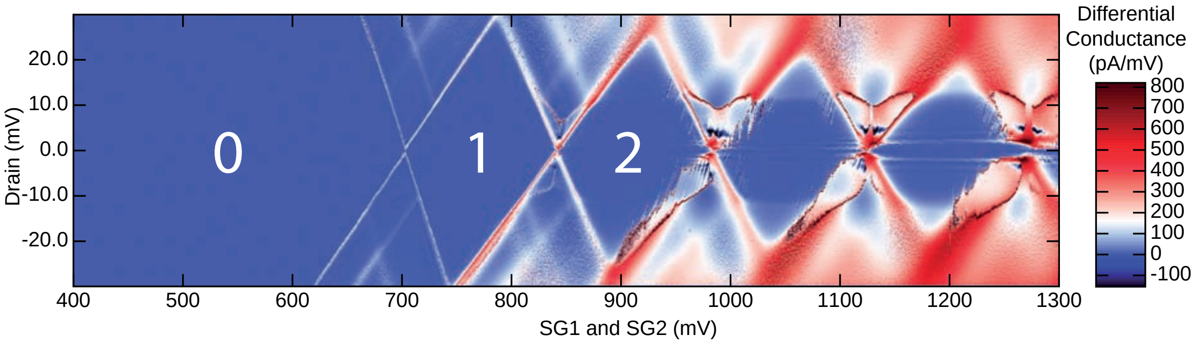

Figure D.11: *Coulomb diamonds over bigger bias range for D3 with the electron numbers indicated in white.*

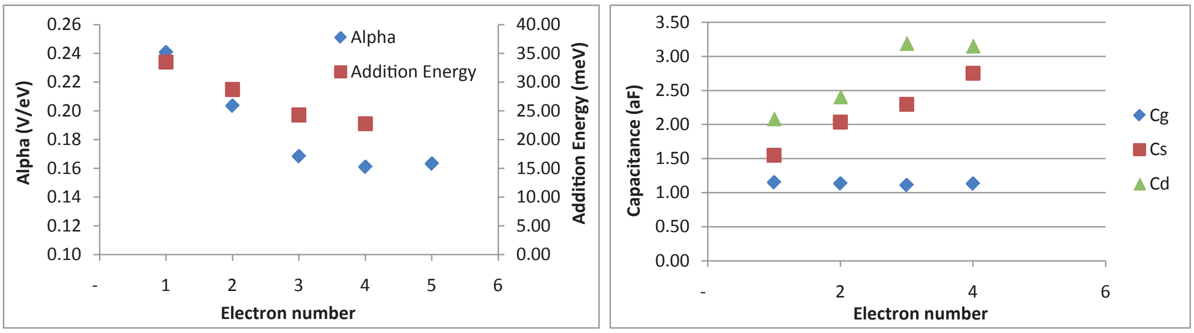

Figure D.12: *Values for alpha and addition energy of D3 for the first electrons (left), and capacitance to the gate (Cg), source (Cs) and drain (Cd) for the same electrons (right).*

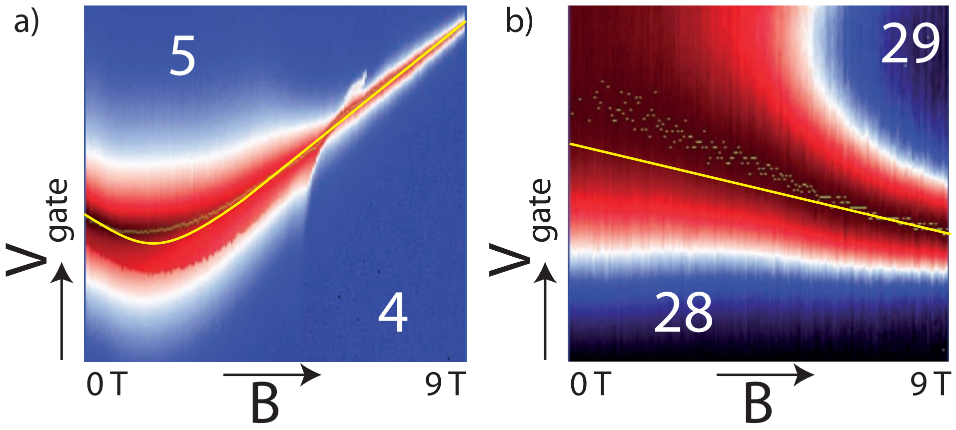

Figure D.13: *Current measurement as a function of gate and magnetic field with extracted peak positions (green) and estimate of the underlying state position (yellow).*

D.5 Extracting magnetic field curves

The magnetic field dependence of different states needs to be extracted from the gate against field curves. To accomplish this, the α-factor is used to convert gate voltage to energy. Now a systematic measure needs to be found to determine 'the' energy of the state, so without contribution from Kondo or mechanical vibrations. At a low bias, a reasonable and systematic measure of the position of the state in energy space is given by the maximum of the Coulomb peak. Unfortunately, two effects are moving this peak away from the actual position of the state in energy space.

The first is mechanical vibration and is shown for the fifth electron in figure D.13(a), which makes the peak broader than it actually is. That this broadening is due to mechanics can be seen in the Coulomb diamonds of figure D.5. As a result, the maximum of the Coulomb peak (green) is not necessarily equal to the position of the state. From a heuristic view on the curve of figure D.13(a), the yellow line would *likely* be more accurate for the actual position of the state. Thus, the extracted (green) peak position has a deviation from the 'true' peak position.

The mechanics is suppressed if the bias is lowered even further, but here a second effect obscures the level-position. Figure D.13(b) is taken at the lowest bias where clear Coulomb peaks were still visible and the Coulomb diamonds show no mechanical feedback. The peaks are still broadened, however, by the Kondo effect as discussed briefly in the theory section 2.2.3. This creates current in the Coulomb blockade region, probably moving the maximum of the original Coulomb peak somewhat towards the side. The peak in figure D.13(b) shows the extracted peaks in green, and, again, in yellow a heuristic slope is drawn which could be the actual energy position of the state.

So on the one hand, low bias is needed to avoid mechanics, but on the other hand high bias is needed to suppress the Kondo effect. This catch-22 cannot be avoided except if a high field is applied or if the barriers are high enough. For higher field Coulomb diamonds show that both mechanics and Kondo effect are suppressed (see figure D.5), and for the first few electron numbers both are also suppressed because the barriers are higher. Because of this catch-22, it would make sense to look for another way to measure the position of the states and a technique called Inelastic Co-tunneling Spectroscopy was tried. For this technique, inelastic co-tunneling lines in the Coulomb diamond are followed as a function of the field (see theory chapter 2.2.3 and De Franceschi *et al.* (2001)). Because this is at higher bias, Kondo is avoided, and usually the current is low enough to avoid starting any vibrations. In spite of this lower current, the mechanical vibrations were visible here and this technique did not result in useful measurements for this device. For higher electrons, the mechanics destroyed any visibility of the states, so the lowest bias was used in spite of the Kondo present there.

We can conclude that using the peak positions for the position of the state in energy space is not accurate especially at low fields. The slopes as discussed in the main text are therefore extracted from the high field data, but the positions cannot be used on their own to draw quantitative conclusions.

This can be applied to the curves in figure 4.12. Especially at low fields for higher electron numbers, the Coulomb peaks are broadened by the Kondo effect. For the third electron of every shell, the spin-orbit valley crossing (B_1) seems to move suddenly up for the third and fourth shell and move there. It is likely that this movement is an artefact of the extracting of the state position. Another example of these artefacts is probably the slight movement of the turning field between the first electrons of the first three shells. Also the first electron of the fourth shell has a particular peculiar shape at low fields which could be explained as artefacts. Therefore, no direct fits with any theory can be made concerning the energy positions of the state. There is, however, still a firm conclusion that can be drawn from these curves: the slopes involved decrease significantly, and the turning field disappears.

Bibliography

Ando, Tsuneya. 2000. Spin-orbit interaction in carbon nanotubes. *Journal of the physical society of japan*, **69**(6), 1757–1763.

Ashcroft, Neil W., & Mermin, David N. 1976. *Solid state physics*. 1 edn. Toronto: Thomson Learning.

Auslaender, O. M., Steinberg, H., Yacoby, A., Tserkovnyak, Y., Halperin, B. I., Baldwin, K. W., Pfeiffer, L. N., & West, K. W. 2005. Spin-Charge Separation and Localization in One Dimension. *Science*, **308**(5718), 88–92.

Berry, M. V. 1984. Quantal Phase Factors Accompanying Adiabatic Changes. *Proceedings of the royal society of london. a. mathematical and physical sciences*, **392**(1802), 45–57.

Cao, Jien, Wang, Qian, & Dai, Hongjie. 2005. Electron transport in very clean, as-grown suspended carbon nanotubes. *Nat mater*, **4**(10), 745–749.

Castro Neto, A. H., Guinea, F., Peres, N. M. R., Novoselov, K. S., & Geim, A. K. 2009. The electronic properties of graphene. *Rev. mod. phys.*, **81**(1), 109–162.

Chang, A M, & Chen, J C. 2009. The kondo effect in coupled-quantum dots. *Reports on progress in physics*, **72**(9), 096501.

Charlier, Jean-Christophe, Blase, Xavier, & Roche, Stephan. 2007. Electronic and transport properties of nanotubes. *Rev. mod. phys.*, **79**(2), 677–732.

Cronenwett, Sara M., Oosterkamp, Tjerk H., & Kouwenhoven, Leo P. 1998. A Tunable Kondo Effect in Quantum Dots. *Science*, **281**(5376), 540–544.

Datta, Supriyo. 1997. *Electronic transport in mesoscopic systems*. Cambridge University Press.

De Franceschi, S., Sasaki, S., Elzerman, J. M., van der Wiel, W. G., Tarucha, S., & Kouwenhoven, L. P. 2001. Electron cotunneling in a semiconductor quantum dot. *Phys. rev. lett.*, **86**(5), 878–881.

Deshpande, Vikram V., Chandra, Bhupesh, Caldwell, Robert, Novikov, Dmitry S., Hone, James, & Bockrath, Marc. 2009. Mott Insulating State in Ultraclean Carbon Nanotubes. *Science*, **323**(5910), 106–110.

Einstein, Albert. 1916. Zur quantentheorie der strahlung. *Physikalische gesellschaft mitteilungen*, **16**, 47–62.

Feynman, Richard. 1982. Simulating physics with computers. *International journal of theoretical physics*, **21**(6), 467–488.

Feynman, R.P. 2008. *The Pleasure of Finding Things Out: The best short works of Richard P. Feynman*. 1 edn. Basic Books.

Gammon, Daniel. 2000. Semiconductor physics: Electrons in artificial atoms. *Nature*, **405**(6789), 899–900.

Griffiths, David. 2005. *Introduction to quantum mechanics*. 2nd edn. Prentice Hall.

Hanson, R., Kouwenhoven, L. P., Petta, J. R., Tarucha, S., & Vandersypen, L. M. K. 2007. Spins in few-electron quantum dots. *Rev. mod. phys.*, **79**(4), 1217–1265.

Huertas-Hernando, Daniel, Guinea, F., & Brataas, Arne. 2006. Spin-orbit coupling in curved graphene, fullerenes, nanotubes, and nanotube caps. *Phys. rev. b*, **74**(15), 155426.

Hüttel, Andreas K., Steele, Gary A., Witkamp, Benoit, Poot, Menno, Kouwenhoven, Leo P., & van der Zant, Herre S. J. 2009. Carbon nanotubes as ultrahigh quality factor mechanical resonators. *Nano letters*, **9**(7), 2547–2552. doi: 10.1021/nl900612h.

Iijima, Sumio. 1991. Helical microtubules of graphitic carbon. *Nature*, **354**(6348), 56–58.

Iijima, Sumio, & Ichihashi, Toshinari. 1993. Single-shell carbon nanotubes of 1-nm diameter. *Nature*, **363**(6430), 603–605.

Izumida, Wataru, Sato, Kentaro, & Saito, Riichiro. 2009. Spin–orbit interaction in single wall carbon nanotubes: Symmetry adapted tight-binding calculation and effective model analysis. *Journal of the physical society of japan*, **78**(7), 074707.

Jarillo-Herrero, P., Kong, J., van der Zant, H. S. J., Dekker, C., Kouwenhoven, L. P., & De Franceschi, S. 2005a. Electronic transport spectroscopy of carbon nanotubes in a magnetic field. *Phys. rev. lett.*, **94**(15), 156802.

Jarillo-Herrero, Pablo, Kong, Jing, van der Zant, Herre S. J., Dekker, Cees, Kouwenhoven, Leo P., & De Franceschi, Silvano. 2005b. Orbital kondo effect in carbon nanotubes. *Nature*, **434**(7032), 484–488.

Javey, Ali, & Kong, Jing (eds). 2009. *Carbon nanotube electronics*. Springer.

Kane, C. L., & Mele, E. J. 1997. Size, shape, and low energy electronic structure of carbon nanotubes. *Phys. rev. lett.*, **78**(10), 1932–1935.

Kouwenhoven, L P, Austing, D G, & Tarucha, S. 2001. Few-electron quantum dots. *Reports on progress in physics*, **64**(6), 701.

Kuemmeth, F., Ilani, S., Ralph, D. C., & McEuen, P. L. 2008. Coupling of spin and orbital motion of electrons in carbon nanotubes. *Nature*, **452**(7186), 448–452.

Ladd, T. D., Jelezko, F., Laflamme, R., Nakamura, Y., Monroe, C., & O'Brien, J. L. 2010. Quantum computers. *Nature*, **464**(7285), 45–53.

Leturcq, Renaud, Stampfer, Christoph, Inderbitzin, Kevin, Durrer, Lukas, Hierold, Christofer, Mariani, Eros, Schultz, Maximilian G., von Oppen, Felix, & Ensslin, Klaus. 2009. Franck-condon blockade in suspended carbon nanotube quantum dots. *Nat phys*, **5**(5), 327–331.

Lide, D. R. (ed). 2008. *Crc handbook of chemistry and physics*. 89 edn. CRC Press.

Liu, Peng, Sun, Qin, Zhu, Feng, Liu, Kai, Jiang, Kaili, Liu, Liang, Li, Qunqing, & Fan, Shoushan. 2008. Measuring the work function of carbon nanotubes with thermionic method. *Nano letters*, **8**(2), 647–651. doi: 10.1021/nl0730817.

Minot, E. D., Yaish, Yuval, Sazonova, Vera, & McEuen, Paul L. 2004. Determination of electron orbital magnetic moments in carbon nanotubes. *Nature*, **428**(6982), 536–539.

Minot, E.D. 2004 (August). *Tuning the band structure of carbon nanotubes*. Ph.D. thesis, Cornell University.

Novoselov, K. S., Geim, A. K., Morozov, S. V., Jiang, D., Zhang, Y., Dubonos, S. V., Grigorieva, I. V., & Firsov, A. A. 2004. Electric Field Effect in Atomically Thin Carbon Films. *Science*, **306**(5696), 666–669.

Pustilnik, Michael, & Glazman, Leonid. 2004. Kondo effect in quantum dots. *Journal of physics: Condensed matter*, **16**(16), R513.

Reimann, Stephanie M., & Manninen, Matti. 2002. Electronic structure of quantum dots. *Rev. mod. phys.*, **74**(4), 1283–1342.

Sapmaz, S., Blanter, Ya. M., Gurevich, L., & van der Zant, H. S. J. 2003. Carbon nanotubes as nanoelectromechanical systems. *Phys. rev. b*, **67**(23), 235414.

Sapmaz, S., Jarillo-Herrero, P., Blanter, Ya. M., Dekker, C., & van der Zant, H. S. J. 2006. Tunneling in suspended carbon nanotubes assisted by longitudinal phonons. *Phys. rev. lett.*, **96**(2), 026801.

Schönenberger, Christian. 2000 (April). *Bandstructure of graphene and carbon nanotubes: An exercise in condensed matter physics*.

Steele, A.G., Gotz, G., & Kouwenhoven, L.P. 2009a. Tunable few-electron double quantum dots and klein tunnelling in ultraclean carbon nanotubes. *Nat nano*, **4**(6), 363–367.

Steele, G. A., Huttel, A. K., Witkamp, B., Poot, M., Meerwaldt, H. B., Kouwenhoven, L. P., & van der Zant, H. S. J. 2009b. Strong Coupling Between Single-Electron Tunneling and Nanomechanical Motion. *Science*, **325**(5944), 1103–1107.

Sze, S.M. 1981. *Physics of semiconductor devices*. 2nd edn. Wiley.

Thijssen, J.M., & Van der Zant, H.S.J. 2008. Charge transport and single-electron effects in nanoscale systems. *physica status solidi (b)*, **245**(8), 1455–1470.

Wallace, P. R. 1947. The band theory of graphite. *Phys. rev.*, **71**(9), 622–634.

Wikipedia. July 3rd, 2010. *History of the internet*. `http://en.wikipedia.org/w/index.php?title=History_of_the_Internet&oldid=368745844`.